

UC Berkeley

UC Berkeley Electronic Theses and Dissertations

Title

Multidimensional Spectroscopy of Photosynthetic Complexes

Permalink

<https://escholarship.org/uc/item/5j97q5cw>

Author

Schlau-Cohen, Gabriela Sadira

Publication Date

2011

Peer reviewed|Thesis/dissertation

Multidimensional Spectroscopy of Photosynthetic Complexes

by

Gabriela Sadira Schlau-Cohen

A dissertation submitted in partial satisfaction
of the requirements for the degree of

Doctor of Philosophy

in

Chemistry

in the

Graduate Division

of the

University of California, Berkeley

Committee in charge:

Professor Graham R. Fleming, chair

Professor Richard A. Mathies

Professor Krishna K. Niyogi

Fall 2011

Multidimensional Spectroscopy of Photosynthetic Complexes

©2011

by

Gabriela Sadira Schlau-Cohen

Abstract

Multidimensional Spectroscopy of Photosynthetic Complexes

by

Gabriela Sadira Schlau-Cohen

Doctor of Philosophy in Chemistry

University of California, Berkeley

Professor Graham R. Fleming, Chair

Experiments using two-dimensional (2D) electronic spectroscopy to investigate the structure-function relationships that give rise to photosynthetic energy transfer within pigment protein complexes are presented and discussed in this dissertation. 2D electronic spectroscopy using ultrafast laser pulses throughout the visible regime was applied to study excitation energy transfer in the major light harvesting complex of photosystem II (LHCII) and the reaction center from purple bacteria. These experiments elucidated information about the excited state structure and the energy transfer timescales within these complexes. All-parallel 2D spectroscopy was used to monitor the energy transfer dynamics in LHCII and reveals previously unobserved sub-100 fs energy transfer between the chlorophyll-*b* (Chl-*b*) and chlorophyll-*a* (Chl-*a*) bands and within the Chl-*a* band. Reproducing these results with simulations led to improvements in the values of the uncoupled transition energies of the chlorophyll in the working Hamiltonian of LHCII. The delocalized excited states observed in the experimental and theoretical results were found to increase the range of optimal angles for energy transfer from LHCII to neighboring pigment-protein complexes, as opposed to the case of a single, isolated donor excited state. Polarized 2D spectroscopy experiments reported here identified previously unresolved excitation energy transfer steps in LHCII. These results were used to determine the angle between transition dipole moments of the donor and acceptor. A new method was developed to use the angle between transition dipole moments to find the uncoupled transition energies of the chlorophyll, previously the major unknown for an accurate electronic Hamiltonian. This method was applied to LHCII. Quantum coherence, or a long-lived superposition of excited states, was observed in LHCII using a second polarization sequence. The observable timescales of coherence was determined to be 700-900 fs, which illustrates that quantum coherence lasts longer than many energy transfer steps. The potential contribution of coherence to the robustness of photosynthetic energy transfer to the rugged energy landscape and to temperature variations is discussed. Experiments on the B band of the bacterial reaction center were able to isolate the previously inseparable two peaks and observe energy transfer between these two excited states. A new extension of 2D spectroscopy, two-color 2D spectroscopy, was demonstrated for examining the interactions between two spectrally separate chromophores. Using this approach, energy was found to transfer from the carotenoid to the bacteriochlorophyll both via S_1 and via Q_x in the bacterial reaction center in an approximately 2:1 ratio, and within about 750 fs.

This work is dedicated to my parents.

Table of Contents

Abstract	1
Dedication	i
Table of Contents	ii
Acknowledgements	iv
Chapter 1: Introduction	1
1.1 Photosynthesis	
1.1.1. Background	
1.1.2. Photosynthetic Complexes	
1.2 Two-Dimensional Electronic Spectroscopy	
1.2.1 Overview of 2D spectroscopic measurement	
1.2.2 Phase stability	
1.2.2.1 Phase in 2D Spectroscopy	
1.2.2.2 Detection of Complex Signals	
1.2.2.3 Retrieval of Excitation Energies	
1.2.2.4 Methods to Generate Correctly Phased Spectra	
1.2.3 Beam Geometry	
1.2.4 Artifacts and Spectral Phase	
1.2.5 Polarization-Dependent 2D Spectroscopy	
1.3 References	
Chapter 2: Pathways of energy flow in LHCII from two-dimensional electronic spectroscopy	20
2.1 Abstract	
2.2 Introduction	
2.3 Methods	
2.3.1 Experimental Methods	
2.3.2 Theoretical Methods	
2.4 Experimental Results	
2.5 Discussion	
2.5.1 Chl-a -> Chl-a Energy Transfer	
2.5.2 Chl-b -> Chl-b Energy Transfer	
2.5.3 Chl-b -> Chl-a Energy Transfer	
2.5.4 Theoretical Discussion	
2.5.5 Intercomplex Transfer	
2.6 Conclusions	
2.7 References	

Chapter 3: Spectroscopic Elucidation of Uncoupled Transition Energies in the Major Photosynthetic Light-Harvesting Complex, LHCII.....	47
3.1 Abstract	
3.2 Introduction	
3.3 Results	
3.4 Discussion	
3.5 Conclusions	
3.6 Experimental Methods	
3.7 References	
Chapter 4: Direct Imaging of Quantum Coherence in LHCII.....	63
4.1 Abstract	
4.2 Introduction	
4.3 Experimental Methods	
4.4 Results & Discussion	
4.5 Conclusions	
4.6 References	
Chapter 5: Investigating Energy Transfer in the Bacterial Reaction Center with 2D Spectroscopy.....	77
5.1 Introduction	
5.2 Experimental Methods	
5.3 Results & Discussion	
5.3.1 Relaxation within the B band	
5.3.2 Energy transfer from neurosporene to the B band	
5.4 Conclusions	
5.5 References	
Chapter 6: Conclusion.....	90
6.1 Afterword	
6.2 References	
Appendix A: Theoretical methods for Simulation of 2D Spectra of LHCII.....	92
Appendix B: Additional Figures and Calculating the Angle between Excited State Transition Dipole Moments.....	93
B.1 Angle between etdms for model dimer system	
B.2 Additional Figures	

Acknowledgements

Many people have contributed both science and support to aid this project through my years of graduate school. I am grateful for the mentorship and physical insight provided by my advisor, Prof. Graham Fleming. Thank you for fostering an open research environment that provided the space for me to learn how to become a scientist. Your ability to view and articulate fundamental questions has provided an inspiring framework for me as a researcher. I am also grateful to Prof. Ron Cohen, for always having an open door.

All the members of the Fleming group have been supportive colleagues and friends, offering suggestions, helpful ideas, and comments. I owe thanks to Dr. Elizabeth Read for her mentorship and training and to Prof. Naomi Ginsberg and Dr. Tessa Calhoun for their scientific collaboration. Thanks, also, to Eleonora De Re, who has been an incredibly reliable labmate, and I am lucky that she has also become a friend. I am grateful that Dr. Akihito Ishizaki has always been willing to answer my questions with his consistently brilliant insight. Thanks to Dr. Arijit Kumar De for sharing his expertise. Thank you to Jacquelyn Burchfield for being alternately a shoulder to lean on and a patient tutor. I thank Julia Zaks for always being a constructive critic while being a good friend. Thanks, as well, to the following for, among enumerable other contributions, Dr. Jahan Dawlaty for calm, wisdom, and lessons on the details of optics, Kapil Amarnath for re-teaching me biology, Doran Bennett for discussions, Dr. Vanessa Huxter for insight about lab problems, and Emily Jane Glassman for consultations in etiquette. To the rest of the Fleming lab, thank you for discussions, help, and camaraderie.

Prof. Roberto Bassi, Dr. Matteo Ballottari, Prof. Robert Blankenship, and Prof. Richard Cogdell generously provided samples and patiently answered questions about the function of the photosynthetic organisms. I am also extremely grateful to Nancy Turley and Tiffaney Dressen for handling a huge variety of administrative problems, and lending a supportive ear when needed.

Many thanks to my parents who have consistently encouraged me to choose my own path, and then supported me in whatever I have pursued. Finally, thanks to Christian who has often born the brunt of it all with patience and humor.

Chapter 1

Introduction

Sections of this chapter are reproduced with permission from
G. S. Schlau-Cohen, J.M. Dawlaty, G. R. Fleming
“Ultrafast Multidimensional Spectroscopy: Principles and Applications to Photosynthetic Systems”
IEEE – Journal of Selected Topics in Quantum Electronics, DOI: 10.1109/JSTQE.2011.2112640.
© 2011 Institute of Electric and Electronics Engineers

Sections of this chapter are reproduced with permission from
G. S. Schlau-Cohen, Akihito Ishizaki, G. R. Fleming
“Two-dimensional Electronic Spectroscopy and Photosynthesis: Fundamentals and Applications to Photosynthetic
Light-Harvesting”
Chemical Physics, DOI: 10.1016/j.chemphys.2011.04.025.
© 2011 Elsevier

1.1 Photosynthesis

1.1.1 Background

Biological systems consist of complex machinery of molecular components that combine to drive non-equilibrium processes through time and space¹⁻³. The precise molecular principles and detailed molecular mechanisms of most biological processes remain elusive. The complexity of molecular constituents within biological systems continues to challenge experimental and theoretical methods. Ultrafast spectroscopy has proved to be a valuable tool to examine the dynamics underlying a variety of biological processes^{3, 4}. In recent years, multidimensional spectroscopy has emerged rapidly as a particularly powerful ultrafast technique to study the ultrafast dynamics of complex systems⁵. The technique provides a unique window into ultrafast non-equilibrium behaviors of these systems.

An understanding of the photosynthetic apparatus is particularly critical in the context of a growing need for renewable energy sources. Photosynthesis powers essentially all life on earth. In light-harvesting organisms, these conditions lead to a general architecture of pigment-protein complexes where large, dense arrays of chromophores serve as antennae, or the sites of initial absorption events. The excitation then migrates quickly, without losses from relaxation to the ground state, to a location, the reaction center, where a photochemical reaction traps the excitation and initiates an electron transfer chain that converts the light energy to usable chemical energy⁶.

LHCII, the complex discussed in the first three chapters of this work, is the power source for green plants. It binds over 50% of the world’s chlorophyll and is the most abundant light-harvesting complex. As shown in Fig. 1.1a, LHCII complexes are found surrounding the reaction center, and comprise the majority of the antenna regions. In Fig. 1.1b, the structural model of LHCII is displayed. The complex has a trimeric structure, where each monomer contains fourteen chlorophyll and four carotenoids held within a protein matrix of three fully and one partially trans-membrane alpha-helices.⁷ The fourteen chlorophyll are found in two spectral and structural variants, 8 Chl-a and 6 Chl-b, which gives rise to two broad peaks for the Q_y (S_0 -

S₁ transition) region, as will be discussed in Chapters 2-4, with Chl-a centered at ~14,900 cm⁻¹ and Chl-b at ~15,400 cm⁻¹.

After absorption, the excitation migrates from the antenna complexes to the reaction center. Unlike the antenna complexes, the reaction centers show very similar structures across organisms. In the final chapter, the reaction center from purple bacteria is investigated using 2D spectroscopy. Extension of 2D spectroscopy to non-degenerate implementations are described, which allows investigation of carotenoid-chlorophyll interaction.

1.1.2 Photosynthetic Complexes

Photosynthetic light harvesting occurs within arrays of pigment-protein complexes (PPCs) which complete absorption and subsequent transport of photoenergy to a designated location (the reaction center) for a charge separation step to drive chemical reactions.¹ This contrasts with a photovoltaic light-harvesting mechanism, where the initial absorption event is a charge separation, or the creation of an electron-hole pair, throughout the material. In the case of green plants, photosynthetic light harvesting occurs in sub-cellular structures, or organelles, called chloroplasts. These are disc-like objects, about 10 μm in diameter and about 2 μm thick. Within the chloroplast, there is a membrane constructed from a lipid bilayer, called the thylakoid membrane, arranged into stacks about 500 nm in diameter.⁸ The thylakoid membrane houses dense networks of PPCs, generally grouped into photosystems of about 20 PPCs. LHCII, the PPC I will be focusing on here, is about 2 nm across and its structure as obtained from x-ray crystallography is shown in Fig. 1.1b. In photosynthesis, the absorption event generates an excited state on the chromophores within the antenna array. The excitation then migrates through the PPCs to reach the reaction center in a process that generally lasts approximately 200 ps.^{9, 10} Each energy transfer step takes between 100 femtoseconds to many picoseconds.¹¹ Because solar intensity is only (on average) 1 kW/m², in order to be able to utilize all incident photons photosynthetic organisms have a high density of pigments. Inside the chloroplast, 80% of the area of the thylakoid membrane is occupied by PPCs.⁸ Inside the protein matrix of a given PPC, there is approximately 1 molar concentration of chlorophyll, which is much more concentrated than the point at which quenching effects begin for chlorophyll in solution^{7, 12} The density of chromophores within LHCII is illustrated in the structural model in Fig. 1.1b.⁷ As seen in Fig. 1.1b, chlorophyll, the primary light-harvesting molecule, and carotenoids, a secondary light-harvester, are held in a close-packed arrangement by a protein scaffold. The density produces strong Coulombic interactions (10-500 cm⁻¹) between chromophores and between chromophores and the protein. The electrodynamic interactions are highly sensitive to position and relative orientation of the molecular components, so the nanostructure of the chromophores within the protein matrix becomes critical for effective energy transport. The dense packing and resultant strong Coulomb coupling between pigments (stronger than the coupling of the pigments to the protein environment) drive ultrafast energy transfer, produce delocalized excited states, and give rise to quantum coherence, or superpositions between the excited state wavefunctions.

The site basis Hamiltonian for the system is constructed from the uncoupled transition energies of the individual chlorophylls (site energies or diagonal elements), and the couplings between chromophores (off-diagonal elements). Diagonalization of this Hamiltonian results in delocalized excited states or excitons, which are linear combinations of the excited states of the individual chromophores.¹¹ Excitons are the eigenstates of the system, and therefore are the

spectroscopic observables. A single exciton may contain contributions from multiple chromophores. Thus, the energies and transition dipole moments of the excited states result from the interactions between multiple molecules within the structure.

This relation between the states that interact with light and the molecular site states, along with the effect of the surrounding protein matrix, obfuscates the nature of the energy landscape of a PPC within which energy transfer occurs. Pigment-pigment coupling terms, strength of the electron-phonon interaction, size of slow fluctuations of the protein structure, and broadening due to fast vibrational motion all contribute to the energy transfer dynamics and spectroscopic measurements.¹¹ This large number of structural variables together determine the excited state energies and mechanisms of energy transport, and all have similar magnitudes making it difficult to use approximate models.^{11, 13} The collective effect on the energy landscape due to these variables as measured by linear absorption is illustrated for a model dimer of chlorophyll in Fig. 1.2. In Fig. 1.2a, a single transition energy in the absence of any broadening variables (shown on the right) is shown for identical chlorophyll (shown on the left). In this case, the excitation Hamiltonian is simply,

$$H_{el} = \sum_{j=1}^N |j\rangle \varepsilon^0 \langle j| \quad (1.1)$$

where ε^0 is the transition energy of a pigment and is the same for all pigments j . In PPCs, chlorophylls are held within a protein matrix and the protein pockets surrounding each chlorophyll molecule vary (illustrated in Fig. 1.2b, left). These differences change the protein environment and therefore change the transition energies of the chlorophyll. As shown in Fig. 2b, right, the single transition has changed to two. The Hamiltonian can then be written as,

$$H_{el} = \sum_{j=1}^N |j\rangle \varepsilon_j^0 \langle j| \quad (1.2)$$

where ε_j^0 is the transition energy of the j^{th} pigment. As discussed above, the dense packing of chlorophyll in PPCs leads to strong couplings (shown in Fig. 1.2c, left), thus changing the transition energies and dipole strengths (reflected in Fig. 1.2c, right). With the addition of coupling terms, the Hamiltonian becomes,

$$H_{el} = \sum_{j=1}^N |j\rangle \varepsilon_j^0 \langle j| + \sum_{i<j}^N J_{ij} (|i\rangle \langle j| + |j\rangle \langle i|) \quad (1.3)$$

with coupling energy J_{ij} between sites i and j . Wavefunctions of the diagonal form of this Hamiltonian or excitons are linear combinations of single chromophore excitations

$$|\psi_k\rangle = \sum_{j=1}^N c_{kj} |j\rangle \quad (1.4)$$

where the coefficient c_{kj} is proportional to the contribution of chromophore j to exciton k .

Diagonalization of H_{el} also gives rise to multiply excited states, where more than one excitation resides in the complex at the same time. In this work, we will restrict most of our discussion to the one exciton states because these are the only states accessed by the low density of sunlight. The two-exciton states can, however, contribute to a 2D spectrum and can provide important insight into coupling between pigments, as has been discussed elsewhere^{14, 15}. Next, because most spectroscopic experiments are ensemble measurements, meaning the volume of the sample interrogated by the laser contains a large number of complexes, the variations between

complexes due to slow fluctuations in protein configuration lead to inhomogeneous broadening in the transition energies. Configuration changes mean differences in orientation and distances between the chromophore transition dipoles relative to the protein backbone and to the polar groups bound to the protein, changes in bowing of the aromatic ring of the chlorophyll, etc. These fluctuations change the chromophores' transition energies (and may affect the coupling). The ensemble is shown in Fig. 1.2d, left, and broadening from variations in the ensemble in Fig. 1.2d, right. Thus, to represent a given measurement taken on an ensemble of PPCs, the calculated dynamics must be averaged over a distribution of transition energies, ϵ_j^0 . Finally, vibrations of the protein environment lead to homogeneous broadening, producing the spectrum shown in Fig. 1.2e, right. In the presence of the protein environment, the Hamiltonian becomes,

$$H_{tot} = H_{el} + H_{ph} + H_{el-ph}. \quad (1.5)$$

The dynamics of the phonon modes of the protein bath are contained within H_{ph} . For the electron-phonon coupling, H_{el-ph} , a displaced harmonic oscillator model is used. These couplings produce site energy fluctuations described as,

$$H_{el-ph} = \sum_{j=1}^N \left(- \sum_{\xi} \hbar \omega_{\xi} d_{j\xi} q_{\xi} \right) |j\rangle \langle j|. \quad (1.6)$$

The electron-phonon coupling term for each pigment j is a sum over all phonon modes, or all vibrations within the protein bath, where the ξ th mode is described by the dimensionless vibrational coordinate q_{ξ} and frequency ω_{ξ} . The strength of the coupling is scaled according to a proportionality constant d_{ξ} , corresponding to the displacement of the excited state potential energy surface along the generalized coordinate q_{ξ} .^{13, 16} This large number of variables contributing to the system Hamiltonian (and consequently to measurements) makes it difficult to identify the contribution of each component to the dynamics. For example, the linear absorption shown for the model dimer looks almost indistinguishable from a single transition with a high energy tail.

The dynamics of photosynthetic light harvesting and energy transfer are difficult to study by many conventional methods due to broad overlapping transitions and a variety of timescales of energy transfer.¹⁷ Development of advanced spectroscopic methods is necessary to learn about the initial steps of photosynthesis. In the next section, we present 2D electronic spectroscopy as an emerging technique for this purpose.⁵

1.2 Two-Dimensional Electronic Spectroscopy

1.2.1 Overview of 2D Spectroscopic Measurement

2DES is a four-wave-mixing technique, where three interactions between the incident laser fields with the sample induce emission of a signal field. The measured signal is proportional to the third order polarization generated by the three incident laser fields,

$$P^{(3)}(r, t) = \int dt_3 \int dt_2 \int dt_1 S^{(3)}(t_3, t_2, t_1) E_3(r, t - t_3) E_2(r, t - t_3 - t_2) E_1(r, t - t_3 - t_2 - t_1) \quad (1.7)$$

where $E_j(r, t) = A_j(t) \{ e^{-i(\omega t + k_j \cdot r)} + e^{i(\omega t - k_j \cdot r)} \}$. This experiment can be performed with a variety of pulse geometries, methods of delay control, and pulse orderings.¹⁸ A schematic of the apparatus used for the experiments described here is shown in Fig. 1.3.¹⁹

The temporal sequence of the incident pulses is shown in Fig. 1.4a. In order to produce a 2D spectrum, four pulses impinge on the sample. Pulses 1, 2 and 3 generate the signal and pulse

4, called the local oscillator (LO), is used for heterodyne detection.⁵ The delay between pulses 1 and 2, τ , is known as the coherence time, between pulses 2 and 3, T , is known as the waiting time, and between pulses 3 and the signal emission, t , is known as the detection time. A Fourier-transform across τ and t for a given value of T produces a 2D spectrum, which is a correlation map of excitation and emission energies as a function of the time, T , between excitation and emission events.⁵

The excitation frequency is measured indirectly by scanning in time. Pulses 1 and 2 prepare, or excite, the system. When pulse 1 impinges on the sample, the oscillation of the electric field under the envelope of the laser pulse induces an oscillation of the transition dipoles within the ensemble of molecules in the sample, or a coherence $|g\rangle\langle e|$. The frequency of the oscillation of each member of the ensemble is proportional to the excited state energy, Ω_e , because every element contributing to the ensemble propagates with its phase factor, $e^{i\Omega_e\tau}$. The collective oscillation of the phases of the transition dipoles is shown in Fig. 1.4a, bottom. Scanning the coherence time samples this collective oscillation because it imprints phase onto the signal with increasing τ . Interaction of the sample with the second laser pulse stops the oscillation between the ground and excited states.^{5,20} Phase can accumulate during the waiting time, but only from coherence pathways.²¹ After excitation, or interaction with pulses 1 and 2, the system evolves until the arrival of pulse 3. The waiting time is the period over which the photophysics of the system are monitored. The arrival of the third pulse again produces a coherence in the ensemble, $|e\rangle\langle g|$. The resulting oscillatory macroscopic polarization within the sample drives the emission of an electric field, the signal field. Methods of isolating the signal field, which depends on interactions with all three incident beams, from other emitted electric fields will be discussed in Sec. 1.2.3.

In the experimental implementation of 2DES, the data are collected in the time domain along the τ axis, which is Fourier-transformed to produce the excitation frequencies. In most apparatuses, the Fourier-transform of the t axis into the frequency domain, however, is performed experimentally by frequency-dispersing the collinear signal and local oscillator and detecting by spectral interferometry.²² The detected interference, which oscillates in amplitude along τ and exhibits spectral fringes along ω_t , is depicted in Fig. 1.4b. In Fig. 1.4c, an example of raw 2D data is presented in which the oscillations along both axes are visible in the intensity of the detected signal. A Fourier-transform across the τ axis generates the 2D spectrum as shown in Sec. 1.3.2. The experimental implementation in Fig. 1.3, the apparatus used for the experiments described in this work, uses a fully non-collinear geometry.²³ Figure 1.3 shows an approach with mechanical delays and pairwise phase stability from a diffractive-optic based approach. The laser beam is first split by a beam splitter, after which the two pulses are delayed relative to each other by a retroreflector on a delay stage. The two beams are focused onto a diffractive optic optimized for ± 1 orders, which generates two pulse pairs. Glass wedges inserted into beams 1 and 2 introduce delays with attosecond precision. The signal emerges collinear with the local oscillator and the two beams are spectrally dispersed and detected on a charge coupled device in the frequency domain.

1.2.2 Phase stability

1.2.2.1 Phase in 2D spectroscopy. 2D spectroscopy is a measurement technique that recovers a complex-valued signal electric field by detecting at the amplitude, not intensity, level. Determining the phase of the electric field separates the real (absorptive) and imaginary

(dispersive) contributions to 2D spectra. In order to prevent mixing of the real and imaginary components, the two beams used to scan a Fourier-transformed axis must be phase stable, i.e. there must be pairwise phase stability. The measured signal is proportional to the complex-valued, third order polarization, which depends on the phase of the incident electric fields in the following way,²⁴

$$P^{(3)} \propto e^{-i\varphi_1} e^{i\varphi_2} e^{i\varphi_3} \quad (1.8)$$

where φ_i is the phase of the i^{th} field as defined in Eq. 1.7. Acquired phase or phase errors, $\delta\varphi_i$, in the laser fields that generate the signal become mapped onto the measured polarization. As this is a heterodyne experiment, the relationship between the interferometrically detected phase and the phase φ_{sig} has the following form,

$$\begin{aligned} \Delta\varphi_{\text{detected}} &= -\varphi_1 + \varphi_2 + \varphi_3 - \varphi_{LO} + \varphi_{\text{signal}} \\ &= -\Delta\varphi_{1,2} + -\Delta\varphi_{3,LO} \end{aligned} \quad (1.9)$$

which illustrates why pairwise phase stability is sufficient to remove phase errors.²² Therefore, any phase difference between pulse pairs introduced by interferometer imperfections in the setup imprints onto the signal, and in this way mixes the real and imaginary parts of the generated 2D spectrum.

There are both active and passive approaches to generate phase stable pulse pairs. Active phase stabilization methods involve running HeNe tracer beams across each arm of the 2D spectrometer and continuously correcting for path length errors.²⁵ This requires interferometers between each arm. Passive phase stabilization methods include diffractive-optic approaches^{22, 26}, approaches with conventional optics where phase errors cancel²⁷, and fully or partly collinear geometries where phase cycling isolates the signal²⁸. For adaptive- optic based apparatuses, using partially or fully collinear geometries can impede the introduction of phase errors. 2DES apparatuses generally have phase stability in the range of $\lambda/60$ to $\lambda/95$ over many hours.

1.2.2.2. Detection of complex signals. Heterodyne, or interferometric, detection has been described extensively in several references and is a method for measuring a complex field. In most 2D apparatuses, measurement occurs by spectrally dispersing the collinear signal and local oscillator fields and recording in the frequency domain.^{22, 29} The frequency domain, heterodyne-detected signal is the square modulus of the sum of the two fields,

$$\begin{aligned} I(\tau_0, T_0, \omega_t) &= \left| E_{LO}(\omega_t) e^{i\omega_t \Delta t} + E_{\text{sig}}(\tau_0, T_0, \omega_t) \right|^2 \\ &= \left| E_{LO}(\omega_t) \right|^2 + E_{LO}^*(\omega_t) E_{\text{sig}}(\tau_0, T_0, \omega_t) e^{-i\omega_t \Delta t} + E_{LO}(\omega_t) E_{\text{sig}}^*(\tau_0, T_0, \omega_t) e^{i\omega_t \Delta t} + \left| E_{\text{sig}}(\tau_0, T_0, \omega_t) \right|^2 \end{aligned} \quad (10)$$

One of the non-interferometric components, $|E_{LO}|^2$, can be measured separately and subtracted. The final term, which scales quadratically with the low amplitude signal field, becomes vanishingly small and so can be ignored. The interference fringes are illustrated along the ω_t axis of Figs. 1.4b and c. They can be written as $2\text{Re}[E_{\text{sig}}(\tau_0, T_0, \omega_t) E_{LO}(\omega_t)] \cos(\Delta\varphi(\omega_t))$, and so the interference term oscillates with the phase difference between the two fields. From this information, the total characterization of a field distribution, or the separation of the absorptive (real) and dispersive (imaginary) components, can be completed using a known reference field. That is, the frequency domain fringes in the cross term contain information about the phase of the signal with respect to the local oscillator. The frequency of the fringes $\Delta\varphi$ is the sum of acquired phase from the time delay, $\omega_t \Delta t$, and from the phase difference, $\varphi_s - \varphi_{LO}$, between the signal and the local oscillator. Because the temporal offset can be independently measured, the phase of the signal can be recovered.

In a 2D experiment, heterodyne detection offers two primary advantages over homodyne,

or intensity, detection. The first advantage is the separation of the real and imaginary components of the emitted field. The second is that simultaneous detection of two co-propagating fields aids in measuring a low amplitude signal. The magnitude of the cross terms scale linearly with the signal and with the local oscillator. Because the amplitude of the local oscillator can be set to an easily detectable level, the mixed term essentially enhances a low amplitude signal.

In the case of a perfectly functioning apparatus, with no phase offset between beams, precise time delays, and no errors in the arms of the interferometer, the heterodyne detected signal has the correct absolute phase, meaning no mixing of the real and imaginary components.

This accuracy and precision is very challenging to achieve experimentally. Both phase jitter underneath the pulse envelope and small temporal distortions manifest as phase errors in the detected signal. As can be seen from the form of the electric field given in Eq. 1.7, a timing error Δt has a similar effect to a phase error $\Delta\phi$, because it imprints phase $\omega\Delta t$. Thus, subwavelength temporal accuracy is required to maintain phase stability. For example, with the 660 nm pulses, as used in the experiments described in Chapters 2-4, an optical cycle has a duration of 2.2 fs. Therefore, a 1 fs error produces a phase error of almost π . This then requires the following temporal condition for phase stability,

$$-\Delta t_1 + \Delta t_2 + \Delta t_3 - \Delta t_{LO} \quad (1.11)$$

Experimental apparatuses often contain differences in lengths of the arms of the interferometer, jitter in the arms of the interferometer, small errors in time steps, and independent fluctuations of the four beam paths which destroy phase stability. There are experimental and analytical methods to correct for constant phase errors, which will be discussed in Sec. 1.2.2.4.

1.2.2.3. Retrieval of Excitation Energies. During the coherence time, the system evolves in a coherence, so for a given τ_0 , the system acquires a phase $e^{i\omega_\tau\tau_0}$, as illustrated in Fig. 1.4a, bottom. Because the experiment is performed on an inhomogeneously broadened ensemble, the slightly different excited state energy of each member produces an oscillation at a slightly different frequency, which causes the dephasing in the collective oscillation shown in Fig. 1.4a, bottom. Thus, for a given value ω_τ , the interference fringes exhibit an oscillation in amplitude along τ as shown by the red line in Fig. 1.4b, where for each additional increment $\Delta\tau = 2\pi / \omega_\tau$, the signal undergoes a full phase rotation. This resultant oscillation in signal amplitude can also be seen along the τ axis in the raw data shown in Fig. 1.4c. A Fourier-transform across the τ axis retrieves frequencies ω_τ and generates the 2D spectrum. Because the excitation energy is retrieved by scanning the time that the dipoles within the sample undergo a collective oscillation, the measurement requires highly accurate time delays and phase stable pulses. The phase stability is required because an additional phase offset will imprint phase onto the signal similarly to an additional time increment.

In this experiment, the time delay between beams 1 and 2 must be set with higher accuracy and precision than in other techniques. Because scanning this time delay constructs a temporal axis, which is then Fourier-transformed to generate frequencies, errors in temporal sampling produce errors in the frequency domain information. Sub-wavelength accuracy is required to retrieve excitation frequencies without the introduction of Fourier artifacts. The method by which temporal delays are introduced also varies among 2D apparatuses. In Fig. 1.3, the introduction of controllable amount of glass using wedges on stepper motors allows <50 attosecond precision, which is more precise than with conventional delay methods.

Because of the short period of an optical cycle, reconstructing the frequency information through sampling at the Nyquist frequency requires a very large number of data points. While the precision requirement remains, the number of data points needed can be decreased by two approaches, undersampling or sampling in the rotating frame. For the apparatus in Fig. 1.3, the τ delay is often sampled at approximately an odd multiple of the Nyquist frequency of the excitation frequency. The frequency components are limited to those within the bandwidth of the laser, so the detected signal can be unfolded to retrieve the frequency domain information. This method is described in detail in several references.^{19,22-23} In this way, temporal step size can be increased by undersampling the time axis and extracting the frequency through aliasing methods.

The second approach employed in 2D spectroscopy, although not in the apparatus used for the experiments described here, is to detect within the rotating frame. This approach is often employed for 2D apparatuses that use an adaptive optic, such as a spatial light modulator (SLM), to generate pulses and introduce delays.³⁰ We now describe two ways of thinking about applying delays using the rotating wave approximation. First, in the frequency domain, a time delay manifests as a phase factor, $e^{i\omega t}$. The additional phase accrued, therefore, is linear in frequency. Because an SLM directly controls the phase of the beams, an SLM can be used to essentially offset the additional phase along the frequency axis, which results in terms $e^{i(\omega - \omega_{RF})t}$, where the phase off-set along the frequency axis is the rotating frame frequency, ω_{RF} . Therefore, as additional time delays are applied, the oscillation frequency along the τ axis decreases.

In the second picture, delays introduced in the rotating frame can be understood as arising from the fact that the phase control introduced by the SLM allows both phase and time delays to be applied. When the temporal delay is introduced, a phase shift is added as well. The additional phase at each τ is chosen to maintain a constant phase at a selected carrier frequency, ω_{RF} , and all other frequencies components are delayed relative to this reference frequency. Instead of introducing only delay with $e^{i\omega\tau}$, both a time and phase component are mapped onto the pulse, $e^{i(\omega\tau - \omega_{RF}\tau)}$. While delays introduced using conventional techniques introduce delay $e^{i\omega\tau}$, in rotating wave detection, at each time step, the addition of a phase $\omega\Delta\tau - \Delta\phi$ means that scanning an optical cycle in τ does not necessarily correspond to a full phase rotation. In a typical SLM-based apparatus, the oscillatory cycle is often set to ~ 20 fs, which oversamples the oscillations for higher accuracy.

1.2.2.4. Methods to generate correctly phased spectra. 2D electronic spectroscopy almost always requires a phase correction factor to account for experimental phase offsets, which arise from problems such as unequal lengths between the two arms, e.g. $\phi_0 = \phi_1 - \phi_2$. In order to maintain phase stability, however, any phase jitter, $\delta\phi_i$, must occur on both beams, or during the course of data collection $\delta\phi_1 = \delta\phi_2$ and $\delta\phi_3 = \delta\phi_{LO}$. While there are no methods to account for any unequal phase jitter terms, there are several experimental and analytical methods to correct for a constant phase difference. An algorithm-based method has been developed, although it has yet to be widely implemented³¹. The analytical method does, however, offer the potential for significant experimental simplification.

In the passively-stabilized, diffractive optic based setup in Fig. 1.3, phase offset in 2D data is corrected by comparing to separately collected pump-probe data. The projection-slice theorem of Fourier transforms states that the projection in one domain is equivalent to a slice in another domain.^{5,20} This equivalency gives rise to a relationship between the pump-probe data

and the 2D data. The projection along the ω_τ axis is related to the slice at $\tau=0$, which is a pump-probe measurement. The projection slice theorem relates the real component of a projection of the 2D data to spectrally resolved pump-probe data in the following way,

$$S_{pump-probe}(\omega_t, T_0) = \text{Re} \left[\omega_t E_{probe}(\omega_t) \int_{-\infty}^{\infty} \frac{d\omega_\tau}{2\pi} S_{PE}(\omega_t, T_0, \omega_\tau) \right] \quad (1.12)$$

where $E_{probe}(\omega_t)$ is the electric field of the probe pulse. Transient absorption experiments are able to recover the correct phase because pump-probe experiments involve only two pulses, where the first two interactions are both from pulse 1 and the third interaction and the local oscillator are from pulse 2. Therefore, it is an inherently phased measurement. By fitting the projection of a 2D spectrum to the spectrally resolved pump-probe data, the absolute phase of the measured data can be retrieved. A zeroth and first order phase correction term, $e^{i\varphi_0 + i\omega_t \Delta t}$, is generally sufficient to match the 2D spectra to the pump-probe data. This approach, however, only works when the spectrum ($\omega_1 = \omega_2, \omega_3 = \omega_{LO}$) and the polarization ($\hat{E}_1 = \hat{E}_2, \hat{E}_3 = \hat{E}_{LO}$) are the same for each pulse pair.

1.2.3 Beam geometry

A 2D spectrum is a sum of the selected energy and momentum conserving pathways, $\mathbf{k}_s = -\mathbf{k}_1 + \mathbf{k}_2 - \mathbf{k}_3$. The experiment can be performed in fully, partially, or non-collinear beam geometries^{22, 32, 33}. In the case of non-collinear geometries, the condition of momentum conservation limits the spectrum from the signal detected in the spatially phase-matched direction to a subset of third-order signals, or a subset of molecular processes. The selected third-order signal can be extracted through spatially windowing and detecting using a box geometry. In this geometry, there is background free detection of the generated signal. In the case of fully or partially collinear geometries, phase cycling is used to isolate the signal^{28, 30}. In phase cycling, the signal is isolated by a linear combination formed from selectively multiplying each beam or combinations of beams by a phase factor, $e^{i\pi}$. For this process, because the signal has phase dependence on all three excitation pulses, multiplying any odd number of pulses by the phase factor $e^{i\pi}$ flips the phase of the signal. Multiplying an even number of pulses by the phase factor does not flip the phase of the signal. Subtracting the sum of the odd permutations from the even permutations separates the third order signal, which depends on all three incident pulses. A phase cycling sequence can also aid in background removal for fully non-collinear geometries because scattered light does not share the third order phase dependence.

1.2.4 Artifacts and spectral phase

In ultrafast experiments, transform-limited compression is often difficult to achieve, particularly for the case of broad bandwidths. Using laser pulses with different orders of spectral phase can lead to various artifacts within a 2D spectrum. Figure 1.5a-c are experimental, absolute value, correlation 2D spectra of the non-resonant response of sapphire. Three different spectral phases were applied to the four laser pulses using an SLM-based 2D apparatus. Figure 1.5a displays the spectrum in the case of almost transform-limited pulses. In this case, basically the spectral profile of the laser pulse is recovered. For the spectrum in Fig. 1.5b, a parabolic phase was applied to the laser pulse. It is important to note here that the peak shape generated by

the chirped pulse can easily be confused with correlated excited states, or an inhomogeneously broadened peak. For a non-resonant response, however, a correlation is physically impossible. Cubic spectral phase, as shown in Fig. 1.5c, is characterized by an x-shaped artifact.

For experiments such as pump-probe spectroscopies, after characterizing dispersion in the laser pulses, algorithms have been used to remove the effects of spectral phase. In 2D spectroscopy, however, algorithms to remove these artifacts from spectral phase are much more complicated.²⁴ Each peak within the generated spectrum is a function of four light-matter interactions. The two frequency axes of the spectrum, however, only provide information about the frequency of two of the four interactions. The two unknown frequencies complicate determination of the effect of sub-optimal compression, even for a well-characterized spectral phase.

The spectral phase can change the time delays between the four interactions. Sample Liouville pathways, corresponding to different molecular processes within the system, are shown in Fig. 1.5d. When all four interactions are at the same frequency, such as in the case of molecular processes corresponding to linear absorption $R_2^{\alpha\alpha}$, there is no effect on the peak. In the case of population transfer (Fig. 1.5e), $R_2^{\alpha\alpha,\beta\beta}$, where $\omega_1 = \omega_2$ and $\omega_3 = \omega_{LO}$, the intended and actual waiting times are different. Measured population dynamics can, therefore, be incorrect. Finally, for the case of $R_2^{\alpha\beta}$ where $\omega_1 \neq \omega_2$ and $\omega_3 \neq \omega_{LO}$, the Fourier-transformed time interval is altered, which leads to incorrect retrieval of frequencies. Essentially, these effects can change the time ordering of the incident pulses and introduce artifacts within the Fourier transform. In the case of spectra with waiting times after the decay of coherence contributions and much longer than the pulse length, chirp effects should no longer appear.

1.2.5 Polarization dependent 2D spectroscopy.

The ability to individually control the polarization direction of each one of the excitation beams (each one of the electric fields in Eq. 1.7) adds additional power to 2D spectroscopy. It is important to distinguish polarization-dependent 2D spectroscopy from those polarization dependent third-order spectroscopies where two interactions with electric fields are derived from the same beam and hence forced to share the same polarization. In fully non-collinear 2D spectroscopy it is possible to prepare polarization sequences that cannot be achieved with partially collinear nonlinear optical methods. Orientational effects in spectroscopy have long been recognized as an integral contributor to the detected signal, and a more complete description is available in many books.

Each light-matter interaction in a Liouville space pathway is a dot product between the light electric field and the sample transition dipole. Although the pigments in the protein are held in fixed angles with respect to each other, the experiments are performed on isotropic ensembles of proteins with no long-range order. For that reason, each Liouville space pathway is scaled by an orientational prefactor, which accounts for isotropic averaging of all four light-matter interactions in that pathway.³⁴⁻³⁶ The orientational prefactor has the following mathematical form,³⁵

$$\begin{aligned}
\langle i_\alpha j_\beta k_\gamma l_\delta \rangle &= \frac{1}{30} [\langle \cos \theta_{\alpha\beta} \cos \theta_{\gamma\delta} \rangle (4 \cos \theta_{ij} \cos \theta_{kl} - \cos \theta_{ik} \cos \theta_{jl} - \cos \theta_{il} \cos \theta_{jk}) \\
&+ \langle \cos \theta_{\alpha\gamma} \cos \theta_{\beta\delta} \rangle (4 \cos \theta_{ik} \cos \theta_{jl} - \cos \theta_{ij} \cos \theta_{kl} - \cos \theta_{il} \cos \theta_{jk}) \\
&+ \langle \cos \theta_{\alpha\beta} \cos \theta_{\gamma\delta} \rangle (4 \cos \theta_{il} \cos \theta_{jk} - \cos \theta_{ij} \cos \theta_{kl} - \cos \theta_{ik} \cos \theta_{jl})]
\end{aligned} \tag{1.13}$$

where $i, j, k,$ and l are the light polarizations in the lab frame and $\alpha, \beta, \gamma,$ and δ are the excited state transition dipole moments in the molecular frame (the pigment-protein complex frame) averaged over an isotropic distribution. This expression arises from the fourth rank tensor invariants, or the pathways which, when rotationally averaged, do not sum to zero. The relationships between the different frames which produce the above expression can be written as,

$$\langle i_\alpha j_\beta k_\gamma l_\delta \rangle = (p_\alpha q_\beta r_\gamma s_\delta) (a_i b_j c_k d_l) \langle a_p b_q c_r d_s \rangle \tag{1.14}$$

where the first term relates the dipole directions to an orthogonal system (p, q, \dots) fixed within the molecular frame. The second term relates the polarizations of the incident pulses to an orthogonal system (a, b, \dots) fixed within the laboratory frame and the final term is the isotropic average over the laboratory and molecular fixed frames. The angle between the transition dipole moments of the excited states participating in a given Liouville space pathway directly affects the orientational prefactor. This dependence can be exploited to decongest crowded 2D spectra by selecting out certain Liouville space pathways.³⁷⁻³⁹ A particularly useful polarization scheme is the ‘‘cross-peak specific’’ polarization sequence $(\pi/3, -\pi/3, 0, 0)$, where the angles refer to the relative polarizations of the three excitation beams E_1 - E_3 and the reference beam E_{ref} respectively. Since only polarizations in the same direction interfere and the signal is retrieved through interferometry with E_{ref} , selecting the polarization of E_{ref} also selects for the polarization direction of the signal. The utility of the cross-peak-specific polarization sequence is that it suppresses pathways that evolve as excited state populations without energy transfer during the waiting time. As a specific example, consider the case where all transition dipole directions in a Liouville space pathway are parallel to each other in the molecular frame. This is true, for example, when all interactions occur with the same dipole, such as the diagonal pathway in Fig. 3. These pathways cannot be accessed by the cross-peak specific polarization sequence because the corresponding orientational prefactor is zero. This approach can also suppress the signals from excited state absorption and incoherent energy transfer, while isolating the signal from pathways that evolve as quantum coherences between non-parallel dipoles during the waiting time.³⁷

In addition to decongesting 2D spectra, control over the polarization of the incident laser pulses offers a means to determine the geometry of the electronic structure (the relative directions of the exciton transition dipole moments).^{39, 40} Since excitons are superpositions of many molecular transitions, their transition dipole moment also becomes a vector sum of the dipole moments of the contributing pigments. The excitonic transition dipole moments, therefore, depend on site energies, couplings, and the relative orientations of the pigments and cannot be simply determined from x-ray diffraction data. The geometry can be inferred from the angles between the transition dipole moments of the excitons. The angles between transition dipole moments can be accessed by measuring the orientational prefactor by comparing the amplitude of a peak under two polarization sequences. Measuring the orientational prefactor using two known polarization sequences of the incident laser pulses provides a measurement of the angle between transition dipole moments of the excitons.

1.3 References

- (1) Dekker, J. P.; Boekema, E. J., Supramolecular organization of thylakoid membrane proteins in green plants. *Bba-Bioenergetics* **2005**, *1706* (1-2), 12-39.
- (2) Nield, J.; Barber, J., Refinement of the structural model for the Photosystem II supercomplex of higher plants. *Bba-Bioenergetics* **2006**, *1757* (5-6), 353-361.
- (3) Sundstrom, V., Femtobiology. *Annu Rev Phys Chem* **2008**, *59*, 53-77.
- (4) van Grondelle, R.; Novoderezhkin, V. I., Energy transfer in photosynthesis: experimental insights and quantitative models. *Phys Chem Chem Phys* **2006**, *8* (7), 793-807.
- (5) Jonas, D. M., Two-dimensional femtosecond spectroscopy. *Annu Rev Phys Chem* **2003**, *54*, 425-463.
- (6) Blankenship, R. E., *Molecular mechanisms of photosynthesis*. Blackwell Science: Oxford, 2002; p 321 p.
- (7) Liu, Z. F.; Yan, H. C.; Wang, K. B.; Kuang, T. Y.; Zhang, J. P.; Gui, L. L.; An, X. M.; Chang, W. R., Crystal structure of spinach major light-harvesting complex at 2.72 angstrom resolution. *Nature* **2004**, *428* (6980), 287-292.
- (8) Kirchhoff, H., Molecular crowding and order in photosynthetic membranes. *Trends in Plant Science* **2008**, *13* (5), 201-207.
- (9) Beddard, G. S.; Carlin, S. E.; Porter, G., Concentration Quenching of Chlorophyll Fluorescence in Bilayer Lipid Vesicles and Liposomes. *Chem Phys Lett* **1976**, *43* (1), 27-32.
- (10) Geacintov, N. E.; Breton, J.; Knox, R. S., Energy Migration and Exciton Trapping in Green Plant Photosynthesis. *Photosynthesis Research* **1986**, *10* (3), 233-242.
- (11) van Amerongen, H.; Valkunas, L.; van Grondelle, R., *Photosynthetic excitons*. World Scientific: Singapore ; River Edge, N.J., 2000; Vol. Ch. 8. Exciton Dynamics, p xiv, 590 p.
- (12) Beddard, G. S.; Porter, G., Concentration Quenching in Chlorophyll. *Nature* **1976**, *260* (5549), 366-367.
- (13) Ishizaki, A.; Fleming, G. R., Unified treatment of quantum coherent and incoherent hopping dynamics in electronic energy transfer: Reduced hierarchy equation approach. *J Chem Phys* **2009**, *130* (23), 234111.
- (14) Read, E. L.; Schlau-Cohen, G. S.; Engel, G. S.; Georgiou, T.; Papiz, M. Z.; Fleming, G. R., Pigment Organization and Energy Level Structure in Light-Harvesting Complex 4: Insights from Two-Dimensional Electronic Spectroscopy. *J Phys Chem B* **2009**, *113* (18), 6495-6504.
- (15) Kim, J.; Mukamel, S.; Scholes, G. D., Two-Dimensional Electronic Double-Quantum Coherence Spectroscopy. *Accounts Chem Res* **2009**, *42* (9), 1375-1384.
- (16) Ishizaki, A.; Calhoun, T. R.; Schlau-Cohen, G. S.; Fleming, G. R., Quantum coherence and its interplay with protein environments in photosynthetic electronic energy transfer. *Phys Chem Chem Phys* **2010**, *12* (27), 7319-7337.
- (17) Schlau-Cohen, G. S.; Calhoun, T. R.; Ginsberg, N. S.; Read, E. L.; Ballottari, M.; Bassi, R.; van Grondelle, R.; Fleming, G. R., Pathways of Energy Flow in LHCII from Two-Dimensional Electronic Spectroscopy. *J Phys Chem B* **2009**, *113* (46), 15352-15363.
- (18) Cho, M., *Two-Dimensional Optical Spectroscopy*. CRC Press: 2009.
- (19) Brixner, T.; Stiopkin, I.; Yang, M.; Fleming, G. R., Tunable two-dimensional femtosecond spectroscopy. *Abstr Pap Am Chem S* **2004**, *227*, U276-U276.

- (20) Ernst, R. R.; Bodenhausen, G.; Wokaun, A., *Principles of nuclear magnetic resonance in one and two dimensions*. Repr. ... 1988 (with corrections). ed.; Clarendon Press ; Oxford University Press: Oxford [England] New York, 1988; p xxiv, 610 p.
- (21) Cheng, Y. C.; Fleming, G. R., Coherence quantum beats in two-dimensional electronic spectroscopy. *J Phys Chem A* **2008**, *112* (18), 4254-4260.
- (22) Brixner, T.; Mancal, T.; Stiopkin, I. V.; Fleming, G. R., Phase-stabilized two-dimensional electronic spectroscopy. *J Chem Phys* **2004**, *121* (9), 4221-4236.
- (23) Brixner, T.; Stiopkin, I. V.; Fleming, G. R., Tunable two-dimensional femtosecond spectroscopy. *Opt Lett* **2004**, *29* (8), 884-886.
- (24) Mukamel, S., *Principles of nonlinear optical spectroscopy*. Oxford University Press: New York, 1995; p xviii, 543 p.
- (25) Bristow, A. D.; Karaiskaj, D.; Dai, X. C.; Cundiff, S. T., All-optical retrieval of the global phase for two-dimensional Fourier-transform spectroscopy. *Opt Express* **2008**, *16* (22), 18017-18027.
- (26) Nemeth, A.; Sperling, J.; Hauer, J.; Kauffmann, H. F.; Milota, F., Compact phase-stable design for single- and double-quantum two-dimensional electronic spectroscopy. *Opt Lett* **2009**, *34* (21), 3301-3303.
- (27) Selig, U.; Langhojer, F.; Dimler, F.; Lohrig, T.; Schwarz, C.; Gieseck, B.; Brixner, T., Inherently phase-stable coherent two-dimensional spectroscopy using only conventional optics. *Opt Lett* **2008**, *33* (23), 2851-2853.
- (28) Shim, S. H.; Zanni, M. T., How to turn your pump-probe instrument into a multidimensional spectrometer: 2D IR and Vis spectroscopies via pulse shaping. *Phys Chem Chem Phys* **2009**, *11* (5), 748-761.
- (29) Lepetit, L.; Joffre, M., Two-dimensional nonlinear optics using Fourier-transform spectral interferometry. *Opt Lett* **1996**, *21* (8), 564-566.
- (30) Gundogdu, K.; Stone, K. W.; Turner, D. B.; Nelson, K. A., Multidimensional coherent spectroscopy made easy. *Chem Phys* **2007**, *341* (1-3), 89-94.
- (31) Davis, J. A.; Dao, L. V.; Do, M. T.; Hannaford, P.; Nugent, K. A.; Quiney, H. M., Noninterferometric two-dimensional fourier-transform spectroscopy of multilevel systems. *Phys Rev Lett* **2008**, *100* (22), -.
- (32) Tian, P. F.; Keusters, D.; Suzuki, Y.; Warren, W. S., Femtosecond phase-coherent two-dimensional spectroscopy. *Science* **2003**, *300* (5625), 1553-1555.
- (33) Grumstrup, E. M.; Shim, S. H.; Montgomery, M. A.; Damrauer, N. H.; Zanni, M. T., Facile collection of two-dimensional electronic spectra using femtosecond pulse-shaping technology. *Opt Express* **2007**, *15* (25), 16681-16689.
- (34) Hochstrasser, R. M., Two-dimensional IR-spectroscopy: polarization anisotropy effects. *Chem Phys* **2001**, *266* (2-3), 273-284.
- (35) Dreyer, J.; Moran, A. M.; Mukamel, S., Tensor components in three pulse vibrational echoes of a rigid dipeptide. *Bulletin of the Korean Chemical Society* **2003**, *24* (8), 1091-1096.
- (36) Barron, L. D., *Molecular Light Scattering and Optical Activity*. 2 ed.; Cambridge University Press: 2004.
- (37) Zanni, M. T.; Ge, N. H.; Kim, Y. S.; Hochstrasser, R. M., Two-dimensional IR spectroscopy can be designed to eliminate the diagonal peaks and expose only the crosspeaks needed for structure determination. *P Natl Acad Sci USA* **2001**, *98* (20), 11265-11270.

(38) Read, E. L.; Engel, G. S.; Calhoun, T. R.; Mancal, T.; Ahn, T. K.; Blankenship, R. E.; Fleming, G. R., Cross-peak-specific two-dimensional electronic spectroscopy. *P Natl Acad Sci USA* **2007**, *104* (36), 14203-14208.

(39) Schlau-Cohen, G. S.; Calhoun, T. R.; Ginsberg, N. S.; Ballottari, M.; Bassi, R.; Fleming, G. R., Spectroscopic elucidation of uncoupled transition energies in the major photosynthetic light-harvesting complex, LHCII. *P Natl Acad Sci USA* **2010**, *107* (30), 13276-13281.

(40) Read, E. L.; Schlau-Cohen, G. S.; Engel, G. S.; Wen, J. Z.; Blankenship, R. E.; Fleming, G. R., Visualization of excitonic structure in the Fenna-Matthews-Olson photosynthetic complex by polarization-dependent two-dimensional electronic spectroscopy. *Biophysical Journal* **2008**, *95* (2), 847-856.

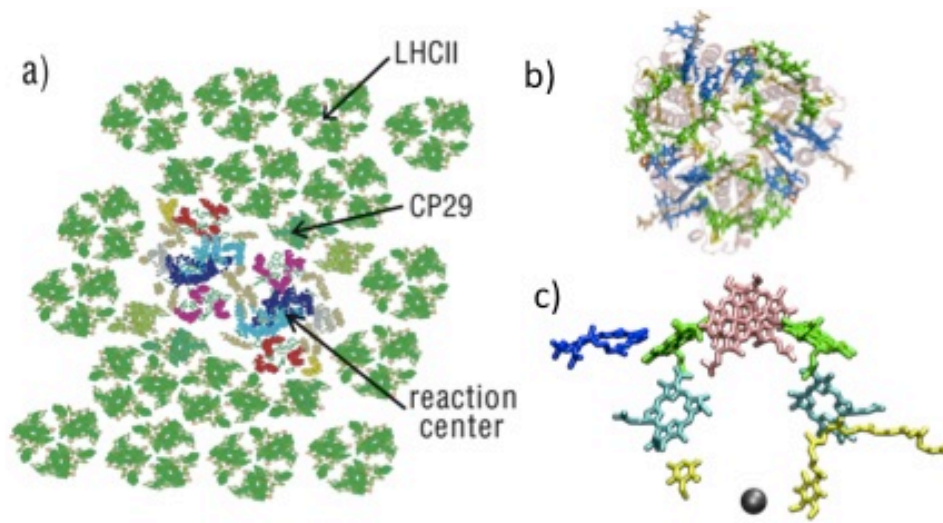


Figure 1.1. Structural models of the light-harvesting pigment protein complexes (a) shows a model of the Photosystem II supercomplex from green plants, (b) a structural model from X-ray crystallography of LHCII, and (c) a structural model from X-ray crystallography of the bacterial reaction center.

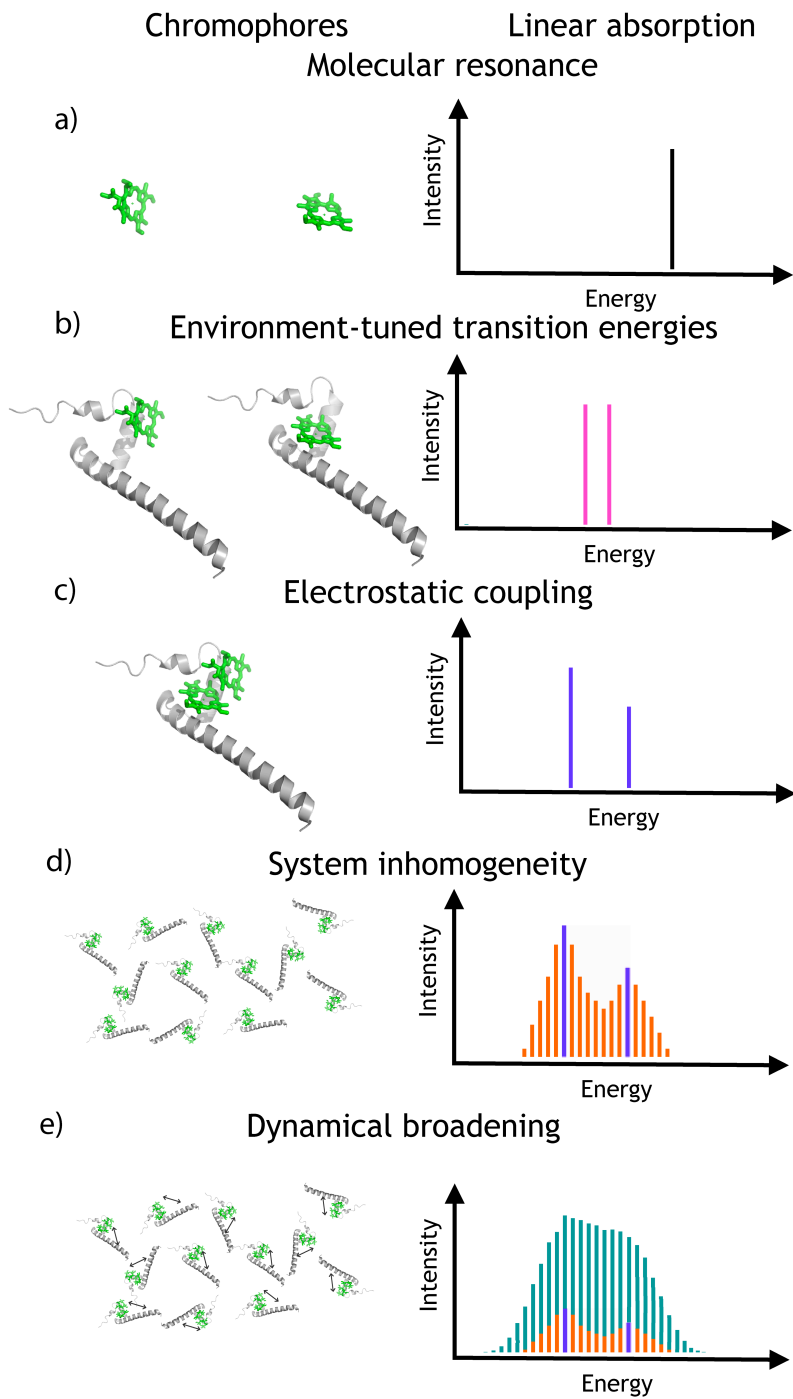


Figure 1.2. a) Two non-interacting chlorophylls without a surrounding environment (left) exhibit a single, narrow resonance (right). b) Two non-interacting chlorophyll in a static surrounding protein environment (left) give rise to two narrow resonances (right) due to differences in the protein surrounding the two chlorophylls. c) Two interacting chlorophylls in a static protein environment (left) give rise to two narrow resonances at different energies (right) due to increased splitting from their coupling. d) Ensemble measurements of a slowly fluctuating sample (left) give rise to an inhomogeneous distribution of resonances (right). e) Vibrational motion (right) gives rise to homogeneous broadening (right).

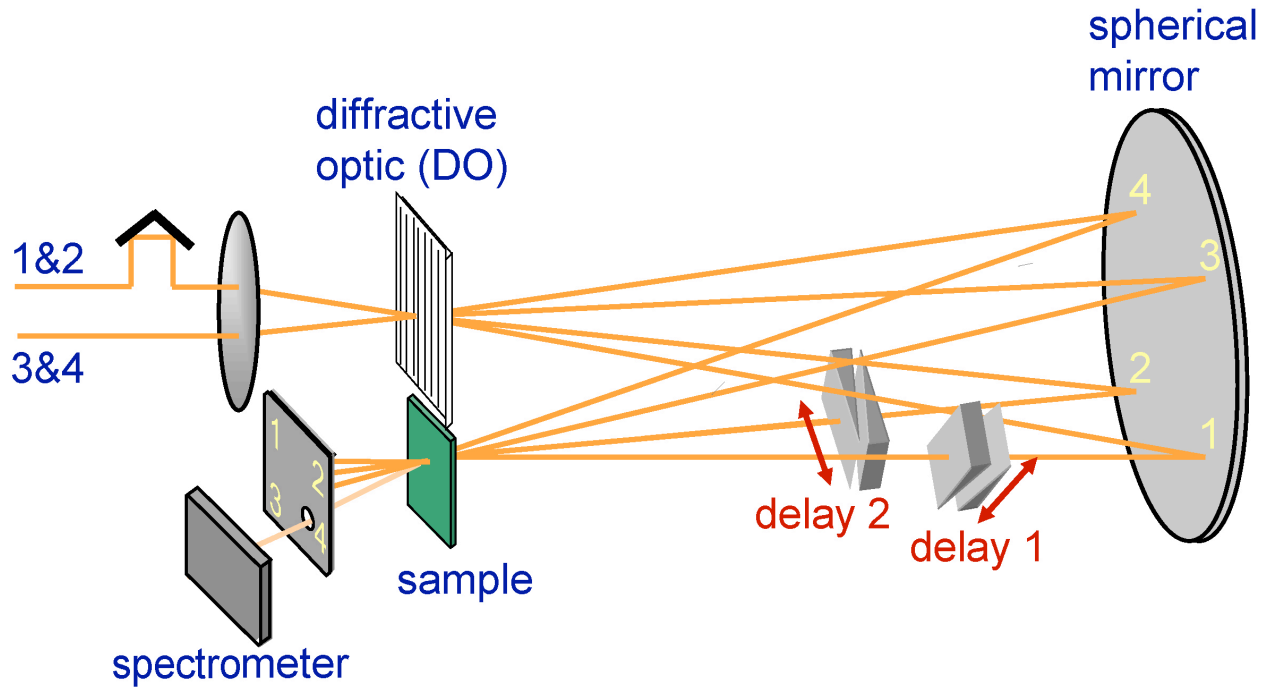


Figure 1.3. A diffractive-optic based apparatus. Two pulses (generated by a beamsplitter and delayed by a retroreflector on a stage) are focused onto a diffractive optic, optimized for ± 1 orders, to generate two pulse pairs. The four beams are focused onto the sample, with beams 1 and 2 delayed with attosecond precision by glass wedges. The signal emerges phase-matched with beam 4 and is spectrally dispersed and detected in the frequency domain on a CCD camera.

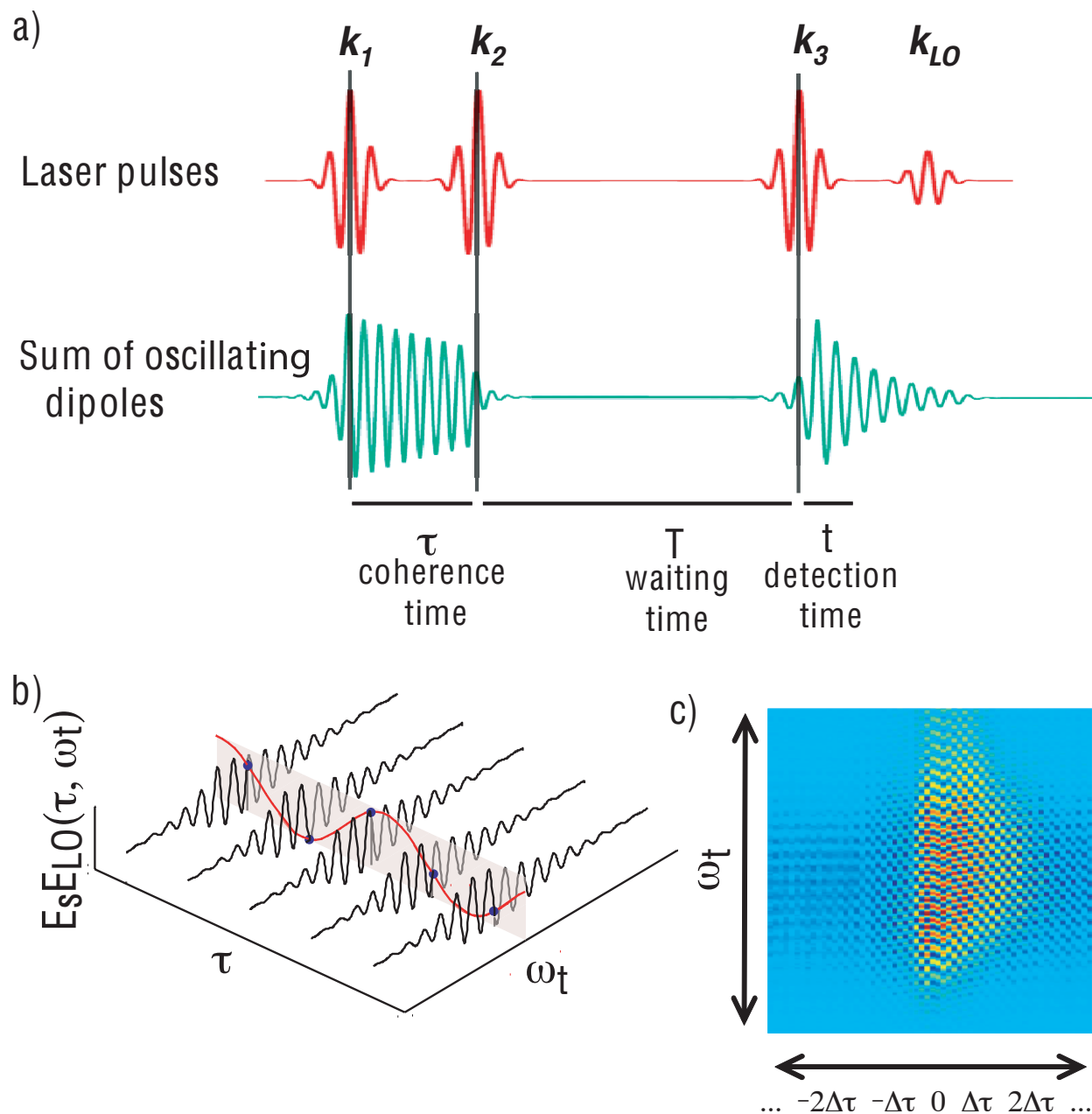


Figure 1.4. 2D spectroscopy can retrieve the excitation energy of the system, usually implemented by sampling the phase evolution of the signal through interferometry. (a) The incident laser pulses and the collective phase of the oscillating dipoles. (b) The form of the detected signal. The fringes along the ω_t axis shows interference from heterodyne detection. The oscillation for a fixed ω_t along the τ axis is the coherent oscillations of the sum of all dipoles in the system. (c) Experimental 2D data, where the ω_t axis shows fringe pattern and the τ axis shows the oscillation from the phase accumulated as a function of τ . The τ axis is Fourier-transformed to generate a 2D spectrum.

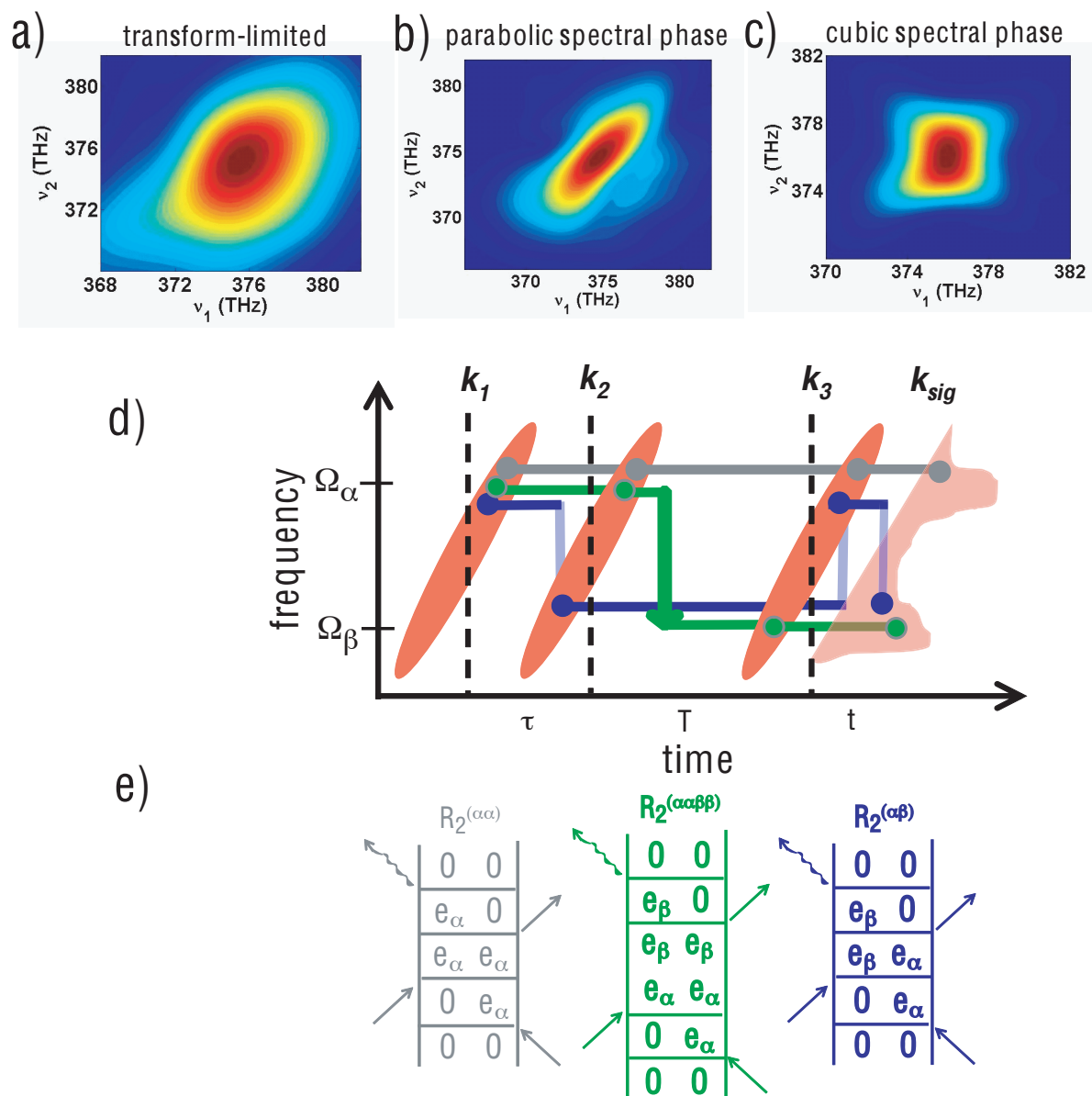


Figure 1.5. Experimental 2D spectra of the nonresonant response of sapphire for transform-limited (a), linearly chirped (b), and cubic applied spectral phased (c) pulses. Spectral phase was applied to the pulses using an SLM-based apparatus. (d) A depiction of linearly chirped pulses for a FWM experiment with trajectories for three sample Liouville pathways. As seen by the trajectories, chirped pulses can result in errors in time spacings. (e) Feynman diagrams to illustrate the Liouville pathways in (d).

Chapter 2

The Pathways of Energy Flow in LHCII from Two-Dimensional Electronic Spectroscopy

This chapter is reproduced with permission from
G. S. Schlau-Cohen, T. R. Calhoun, N. S. Ginsberg, E. L. Read, M. Ballottari,
R. Bassi, R. van Grondelle, G. R. Fleming
“Pathways of energy flow in LHCII from two-dimensional electronic spectroscopy”
Journal of Physical Chemistry B (2009), **113**, 15352-15363
© 2009 American Chemical Society

2.1 Abstract

Photosynthetic light-harvesting complexes absorb energy and guide photo-excitations to reaction centers with speed and efficacy that produce near-perfect efficiency. Light-Harvesting Complex II (LHCII) is the most abundant light-harvesting complex and is responsible for absorbing the majority of light energy in plants. We apply two-dimensional electronic spectroscopy to examine energy flow in LHCII. This technique allows for direct mapping of excitation energy pathways as a function of absorption and emission wavelength. The experimental and theoretical results reveal that excitation energy transfers through the complex on three timescales: previously unobserved sub-100 fs relaxation through spatially overlapping states, several hundred femtosecond transfer between nearby chlorophylls, and picosecond energy transfer steps between layers of pigments. All energy is observed to collect into the energetically lowest and most delocalized states, which serve as exit sites. We examine the angular distribution of optimal energy transfer produced by this delocalized electronic structure and discuss how it facilitates the exit step in which the energy moves from LHCII to other complexes towards the reaction center.

2.2 Introduction

Photosynthesis, the process by which plants and bacteria harvest light energy and convert it to chemical energy, fuels most life on Earth. In the initial steps of photosynthesis, pigment-protein complexes (PPCs) complete the light-to-charge separation steps with a near unity quantum efficiency. Photosynthetic light-harvesting systems function by having a large array of dedicated light-harvesting pigments that absorb energy and funnel the excitation to the reaction center. In the reaction center, the excitation drives a charge separation which begins the photosynthetic chemical reactions.¹ The light-harvesting pigments are grouped locally into complexes with highly specific arrangements within a protein matrix. In higher plants, the majority of photoabsorption occurs in a single type of PPC – Light-Harvesting Complex II (LHCII). Over 50% of plant chlorophylls are bound into this complex.¹ LHCII absorbs in a broad spectral region and then directs the photoexcitation to an exit site. From the exit states, the energy traverses across other LHCII and minor light-harvesting complexes toward the reaction center.^{1,2}

A full understanding of how LHCII harvests light and directs the photoenergy requires identifying the energy flow pathways as dictated by the proximity and orientation of the pigments and relative energies at which they absorb. In LHCII, the excitation travels from higher energy into lower energy states to the exit site, and then transfers from the low energy states to nearby complexes. The chromophores are all held at non-equivalent sites³ which, along with the distance and relative orientations of the molecules⁴, produce the manifold of delocalized excited state wavefunctions. The spatial overlap and energy gaps between these states give rise to the dynamical behavior of the complex. Examining how the structure of the complex produces highly efficient directional energy flow provides insight into the design principles employed in achieving the light harvesting functionality.

LHCII is a hetero-trimeric system composed of three similar monomeric subunits (Lhcb1-3) arranged with C_{3v} symmetry. Each monomer contains chromophores embedded in a protein matrix which itself is held within the thylakoid membrane. Recently, the crystal structure of LHCII was solved with 2.72 Å⁵ and 2.5 Å⁶ resolution, allowing identification of the chlorophyll species and of the orientation of the chromophores within the complex. Figure 2.1 shows the crystal structure of the trimeric LHCII complex, looking onto the plane of the membrane. Each LHCII monomer contains fourteen chlorophyll molecules, eight of chlorophyll a (Chl-a) and six of chlorophyll b (Chl-b), four carotenoids, three full-transmembrane alpha-helices, and two partial-transmembrane alpha-helices. Chl-b differs from Chl-a in that it has an additional carbonyl group which yields a higher energy S_0 to S_1 (Q_y) transition.¹ According to the crystal structure and site-specific mutational analysis, the majority of chlorophyll binding sites are specific to a Chl-a or Chl-b molecule which suggests that the type of molecule plays an integral role in producing the energy transfer pathways.^{5,7} The chlorophylls are arranged in two layers, the stromal and lumenal layers, so-called because of their orientation in the thylakoid membrane. Figure 2.2a displays both layers separately with strongly coupled clusters (~ 20 - 100 cm⁻¹) of neighboring chlorophylls indicated as described by Novoderezhkin, et al.⁸ Spectroscopic studies to probe the energies and timescales of energy transfer, when combined with the structural information from crystallography, have the potential to show how molecular structure gives rise to the electronic structure and the pathways of energy transport.

Components of the pathways of energy transport in LHCII have been mapped using spectroscopic and biochemical tools.^{7,9-11} Ultrafast spectroscopic techniques have identified several timescales of energy transfer within the Q_y excitation region.^{10,12-14} LHCII gives rise to a highly congested spectrum such that multiple timescales appear in features at the same energies due to contributions from different chlorophylls. That is, there are similar energy gaps but different energy transfer rates, perhaps due to different spatial relationships, between states on separate chlorophylls within the complex. Three-pulse photon echo peak shift studies (3PEPS) found Chl-b to Chl-b energy transfer had 300 fs and 800 fs timescales and Chl-a to Chl-a energy transfer occurred on 350 fs, 3 ps, and 6 ps time scales.^{12,14} Chl-b to Chl-a transfer was seen from two distinct groups of Chl-b with several different rates of energy transfer. The higher energy excitons within the Chl-b manifold transferred energy to the Chl-a band with 600 fs and 4 ps time constants and the lower energy excitons of the Chl-b band transferred energy to the Chl-a band with 150 fs and 600 fs time constants. The region between the Chl-b and Chl-a

bands has been examined selectively with pump-probe experiments and these studies have shown a long-lived intermediate state in the region between the two bands.^{10,13} Energy transfer out of this state was found to be almost two orders of magnitude slower than the other Chl-b to Chl-a dynamics observed,¹⁰ suggesting a different relative structure of this intermediate state.

The pigment-based origin of some of the oscillator strength at certain energies has been identified by correlating spectral sub-bands with individual binding sites using mutated LHCII complexes.^{7,11,15} The spectrum of the mutant lacking the chlorophyll at site 614 identified this chromophore as absorbing primarily in the region between the Chl-a and Chl-b bands.¹¹ The lowest energy portion of the spectrum was found to arise from Chl-a 612 through a mutant lacking this pigment.¹¹ Additionally, in the spectra from the mutant including lacking two of the Chl-a molecules (a611 and a612) from the stromal layer chlorophyll trimer, the red-most region of the Chl-a absorption band was also missing.⁷ This suggests that the lowest energy state is located on Chl-a 611 and/or 612, i.e. corroborating the finding that the lowest energy oscillator strength is delocalized across the presumed Chl-a trimer exit site. This result is in agreement with calculations and fitting to results from pump-probe, fluorescence and linear dichroism experiments,^{8,10} all of which were used to produce a Hamiltonian for the complex.⁸ Recent low temperature fluorescence and hole burning experiments¹⁶ have examined the excitonic structure of LHCII. The work of Gibasiewicz, et al. and Pieper, et al. discussed the possibility of the relative energies of the excitonic states rearranging from 4.2 K to room temperature.¹⁶ The temperature dependence of the structural assignments of the excitonic states is not yet clarified.

The work in this chapter presents the energy transfer dynamics of LHCII as determined through two-dimensional (2D) electronic spectroscopy over the Q_y region. The highly congested linear LHCII spectrum contains closely spaced energy levels, static disorder, and homogeneous broadening, all of which prevent easy identification of energy levels and energy transfer. Our technique extends the emitted signal along a second frequency axis, excitation, which results in displaying the pathways of energy flow. Each 2D spectrum is a frequency-frequency map of absorption, energy transfer and coupling at a given delay time.¹⁷ The energies of the spectral features correspond to the exciton basis energies, or the eigenvalues of the site basis Hamiltonian. The site basis Hamiltonian has off-diagonal Coulombic coupling terms and diagonal terms consisting of uncoupled transition energies for individual pigments, and so its eigenvectors describe the delocalized excited states of the system, or excitons.⁹ In photosynthetic complexes, electronic coupling between nearby molecules based on their relative orientations and proximity within the protein matrix effectively re-diagonalizes the system into the exciton basis. It has been shown that the combination of 2D spectroscopic data and theoretical modeling enables the excitons at different energy levels to be mapped back onto the chlorophylls which contribute to those states.^{18,19} Using 2D spectroscopy, the relationship between the relative locations of the excited state wavefunctions and the dynamics of transfer between them can then be elucidated.

An additional question addressed here is how the level of delocalization of excited state wavefunctions guides energy flow through the complex and creates an effective connection to the rest of the PSII supercomplex. The strength of molecular interaction determines the spatial extent of the wavefunction. Because spatial overlap facilitates

very fast relaxation steps between excited state wavefunctions and slower steps correspond to traversing larger spatial distances, the physical size of the wavefunction affects the energy transfer pathways within the complex. The combination of spatial separation and energetic gaps ensures directionality of the energy transfer.¹⁸ Understanding how these optical and dynamical properties arise from a level of delocalization controlled by the specific, finely tuned structural arrangement of chromophores may have applications for designing solar light-harvesting devices.

2.3 Experimental Methods

2.3.1 Theoretical Methods

Trimeric LHCII from *Arabidopsis thaliana* was grown and isolated as described by Caffari, et al.²⁰ LHCII was dissolved in 50 mM HEPES buffer (pH 7.6) with the detergent n-dodecyl α -D-maltoside 0.03% and mixed with glycerol at 30:70 (v/v). The sample was sealed in an Oxford Instruments cryostat using a silanized 200 μ m quartz cell (Starna). The OD of the sample at 660 nm was measured to be 0.13 (per 200 μ m). To ensure no aggregation occurred at the concentration used, a sample at much lower concentration was prepared as well, and the normalized linear absorption of the two samples were compared to confirm correspondence of all features.

Ultrafast (18 fs) laser pulses centered at 640 nm with 80 nm FWHM were generated in a home-built non-collinear optical parametric amplifier (NOPA). The NOPA was pumped with a home-built Ti:sapphire regenerative amplifier that is seeded by a home-built Ti:sapphire oscillator and that produces a 3.4 kHz pulse train of 45 fs pulses near 800 nm.^{21,22} During the experiment, the energy on the sample from each of beams 1, 2 and 3 was 6 nJ per pulse and beam 4 was attenuated, focused to a 100 μ m beam waist. All measurements were performed at 77 K.

The details of the experimental apparatus, data acquisition and analysis have been described in detail elsewhere.²¹ In brief, the single pulse is split into four with a beamsplitter and a diffractive optic. The use of the diffractive optic allows for phase stability between pulse pairs. Four ultrafast beams are incident on the sample in a so-called box geometry. The signal is generated by the interaction of three of the beams with the sample, causing the signal to emerge in the phase-matched direction, $\mathbf{k}_s = -\mathbf{k}_1 + \mathbf{k}_2 + \mathbf{k}_3$, collinear with the fourth beam, a local oscillator pulse. The local oscillator is attenuated to ensure it does not interact strongly with the sample. Using spectral interferometry, the signal is heterodyne-detected in the frequency domain.

The measured electric field is a function of the three time delays between the pulses. The time delay between the first two pulses is known as the coherence time, τ , and is controlled to interferometric precision with movable glass wedges, which were scanned from -566.5 to 566.5 fs in 5.5 fs steps. Negative coherence times generate the non-rephasing signal and positive times generate the rephasing signal. Between the second and third pulses, the system evolves dynamically during a so-called “waiting time,” T . The third time delay, between pulse three and the signal pulse is the rephasing time, t . The frequency-frequency 2D spectrum at fixed T is produced by spectrally resolving the signal along ω_t and then Fourier-transforming along the coherence time axis, τ . In this frequency domain representation, the spectrum directly correlates

excitation and emission energies.²¹ The ensemble of PPCs evolves in a coherence during both the coherence time and the rephasing time. If the system progresses in conjugate frequencies during these two time periods, this allows for the reversal of dephasing and the generation of a photon echo signal. To produce a non-rephasing signal, the ensemble of PPCs evolves with a phase factor of the same sign during the coherence time and the rephasing time, thus generating a free induction decay signal. The rephasing and non-rephasing signals are separated experimentally by the time ordering of pulses one and two. The signal generated over the entire scan, or the sum of the photon echo and free induction decay contributions, produces a relaxation spectrum. 2D spectra were recorded for waiting times in 10 fs steps from 0 to 500 fs and in 1 ps steps from 1 ps to 20 ps. Phasing was performed using the projection-slice theorem by separately measuring the spectrally-resolved pump-probe (SRPP) signal for each waiting time.¹⁷

2.3.2 Theoretical Methods

The theoretical spectra were generated as described in Zigmantas, et al.¹⁹ using non-linear optical response theory. In brief, a Frenkel exciton model Hamiltonian of monomeric LHCII was used to calculate single and double exciton states. The Hamiltonian was constructed from transition density cube couplings⁴ with signs assigned from the ideal dipole approximation (IDA)⁸ calculations and site energies determined through fitting to the linear absorption spectrum. Although there may well be mixed binding sites, the structure determined by x-ray crystallography^{5,6} is used as a starting point. The site energies were further refined by adjustment of their values to generate simulated 2D spectra that had the strongest agreement with the experimental 2D spectra. The 2D spectra serve as a more sensitive indicator of the accuracy of the fitted transition energies than the linear spectrum. Vibronic transitions on the chlorophylls were not included in the Hamiltonian. The model spectral density included discrete vibrational modes of the bath coupled to the chromophores as previously described.²³ Forty-eight vibrational modes were coupled to the transitions through electron-phonon interaction and weighted according to their Huang-Rhys factors, determined experimentally using fluorescence line narrowing and rescaled to fit the data.²⁴ Fast nuclear motion contributing to the homogeneous broadening was additionally included in the lineshape with a single overdamped Brownian oscillator. Quantum dynamical calculations were performed using modified Redfield theory.²⁵ The inhomogeneous broadening, or the effects of slow nuclear motion, was described by explicit averaging over a Gaussian distribution around the site transition energy with $\sigma=80\text{ cm}^{-1}$ through 200 realizations.

2.4 Experimental Results

The linear absorption spectrum in the region of the first electronic excited state of the chlorophyll molecules in the LHCII complex is shown in Figure 2.2b. The combination of the two species of chlorophyll present in LHCII, differences in the local environment of each chromophore within the asymmetric structural motif, and variation in how each pigment couples to its neighbors creates a broadened, highly congested spectrum. The linear absorption spectrum of the Q_y region shows both Chl-a and Chl-b bands, centered at $14,925\text{ cm}^{-1}$ and $15,385\text{ cm}^{-1}$ respectively. The Chl-b peak has a

vibronic tail^{11,26} on the high energy side of the peak, which also contains a small contribution from the Chl-a S_0 to S_2 (Q_x) transition.¹⁵

The real (absorptive) portions of experimental 2D electronic spectra of LHCII are displayed in Figure 2.3 at waiting times selected to summarize the dynamics of the system. In the relaxation spectra of Figure 2.3, left, the peaks along the diagonal predominantly correspond to the linear absorption spectrum, with two Chl-a peaks (the main peak and the shoulder peak) at $14,775\text{ cm}^{-1}$ and $14,900\text{ cm}^{-1}$ and the Chl-b peak at $15,400\text{ cm}^{-1}$. The energy transfer pathways appear as positive features, or cross-peaks, below the diagonal, since energy transfers downhill to the lower energy states. Pronounced excited state absorption (ESA) is seen as a strong negative peak above the diagonal. The intensity of the negative feature arises from the collective oscillator strength of the large manifold of double-exciton states (91 for each monomer).

The relaxation spectra, which display the purely absorptive lineshape, are shown next to their corresponding isolated non-rephasing contributions in Figure 2.3. The non-rephasing spectra display a characteristic “phase-twisted” lineshape, or mixed absorptive and dispersive character which results in extension in the anti-diagonal direction.²⁷ In order to identify and isolate the energy transfer cross-peaks, the non-rephasing spectra provide a useful tool because the off-diagonal portion generally contains mostly contributions from energy transfer and ESA, two processes which produce signal fields of opposite sign. Because coherence peaks appear only on the diagonal in the non-rephasing spectra, the off-diagonal region of the non-rephasing spectra lacks the coherent beating characteristic of relaxation or rephasing spectra.²⁸ Therefore, evolution of positive features off the diagonal results from energy transfer as opposed to coherent beating features.²⁹

Energy transfer cross-peaks appear along two discrete values of ω_t , corresponding to the two resolved diagonal peaks within the Chl-a band ($\omega_t=14,775\text{ cm}^{-1}$; $\omega_t=14,900\text{ cm}^{-1}$). The excitation region can be divided into three main sections: 1) Chl-b ($\omega_\tau>15,200\text{ cm}^{-1}$); 2) the range between Chl-a and Chl-b, or the intermediate region ($15,000\text{ cm}^{-1}<\omega_\tau<15,200\text{ cm}^{-1}$); and 3) Chl-a ($\omega_\tau<15,000\text{ cm}^{-1}$), which contains two peaks (mid-energy Chl-a and low energy Chl-a). Energy transfers out of these three regions into the states which produce the two Chl-a peaks. This gives rise to five cross-peaks (marked with arrows in Figure 2.3a-d, right). The major cross-peak on the picosecond timescale is indicated separately as cross-peak 6 (CP6) in Figure 2.3e. Square regions with a side of 85 cm^{-1} around each cross-peak were integrated in the absolute value non-rephasing spectra to elucidate timescales of energy transfer. The absolute value spectra were used for this analysis to eliminate amplitude variations due to uncertainty in the spectral phase. To examine the very fast early time dynamics (up to 300 fs), the normalized peak traces were subtracted from a normalized integrated region around the lowest energy diagonal rephasing signal. The rephasing low energy diagonal peak is invariant with respect to the dynamics of the system; it only evolves with overall signal decay and time-point specific experimental fluctuation. The peak does not decay as population relaxes and coherence pathways appear off the diagonal in rephasing spectra.³⁰ The subtraction was performed in order to isolate the dynamical evolution in cross-peak amplitude by removing noise that changes at each time-point. The resulting difference traces were smoothed using a 5 point moving filter and are plotted in Figure 2.4a. The slower timescale of the several hundred femtosecond energy transfer processes allows the evolution to be seen directly in

the smoothed traces of the integrated regions, since the smoothing function does not damp the dynamics. These smoothed integrated regions are plotted in Figure 2.4b for 360-430 fs. We examine relaxation processes on three distinct timescales: sub-100 fs, several hundred femtoseconds, and over picoseconds. Absorption across all regions shows eventual relaxation to the lowest energy state.

The energy transfer processes within 100 fs seen here show faster dynamics than found in previous experiments^{10,12-14} or predicted theoretically⁸. For waiting times of 30 fs and 70 fs ($T=30$ fs and $T=70$ fs), the spectra highlight the appearance and evolution of these ultrafast dynamics. Energy transfer at all five cross-peaks appears around 30 fs. Initially, there is previously unobserved higher relative amplitude of the peaks in the mid-energy Chl-a region. These two peaks show energy transfer from the intermediate region, cross-peak 3 (CP3), and the Chl-b region, cross-peak 5 (CP5). By 70 fs, the relative amplitude of the cross-peaks indicating transfer to the low energy Chl-a region is larger. This rise is seen in the increased amplitude of cross-peaks 2 (CP2) and 4 (CP4) in the 70 fs spectrum.

The cross-peak between the mid-energy Chl-a region and the lowest energy Chl-a region ($\omega_r=14,980$ cm^{-1} ; $\omega_i=14,795$ cm^{-1}), labeled as cross-peak 1 (CP1) in Figure 2.3, is directly probed for the first time here. Previous photon echo peak shift experiments¹² monitored population decay as the excitation transferred out of the states encompassed by the limited bandwidth of the laser pulse used. In our 2D data, after the sub-100 fs initial population of this cross-peak, the peak again increases quickly to a maximum at ~ 130 fs, and then grows slowly until ~ 250 -300 fs as shown by the integrated trace of Figure 2.4a. The slower component is similar to that seen in the transient grating experiments¹², but the very rapid component has not been observed previously. This is perhaps due to the significantly shorter pulse duration achieved here or the ability to precisely resolve excitation and emission frequencies, thus better separating this region from other dynamics of the system.

The evolution observed here after ~ 100 fs and over the next several hundred femtoseconds agrees with previous experiments and theoretical predictions.¹⁰ Energy transfer peaks appear from the intermediate region, which lies between the Chl-a and Chl-b bands and so contains contributions from high energy Chl-a and low energy Chl-b. Energy transfer peaks connecting the intermediate region to each band within the main Chl-a region are labeled as CP2 ($\omega_r=15,100$ cm^{-1} ; $\omega_i=14,775$ cm^{-1}) and CP3 ($\omega_r=15,100$ cm^{-1} ; $\omega_i=14,900$ cm^{-1}) in Figures 2.3 and 2.4. After the sub 100 fs appearance of these two cross-peaks, a second component of energy transfer from the intermediate region to the mid-energy Chl-a region, or CP3, grows between 210 fs and 280 fs. This is seen most readily in Figure 3c&d, right, where the relative amplitude of CP3 has again increased compared to the peak below it (CP2) from the $T=200$ fs spectrum to the $T=300$ fs spectrum. CP2, which arises from energy transfer out of the intermediate region to the lowest energy states, rises rapidly to a second maximum at ~ 130 fs, followed by slower growth from ~ 150 -300 fs, as seen in the difference trace of Figure 2.4a. The increased absolute amplitude of CP2 is also seen directly in the $T=200$ fs non-rephasing spectrum (Figure 3c, right). CP3 decays after ~ 300 fs, as is seen in the traces of the integrated regions of Figure 2.4b. CP2 grows in over the same time period, starting at ~ 360 fs. The relative dynamics over 300-500 fs illustrate the correlation between the decrease of CP3 and the increase of CP2, which suggests a multistep mechanism for relaxation into the

lowest energy state.

Rapid relaxation within the Chl-b band around $15,400\text{ cm}^{-1}$ is seen by 70 fs through the asymmetry on the lower right of the Chl-b diagonal band in the relaxation spectra. The antidiagonal broadening characteristic of non-rephasing signals can obscure cross-peaks near the diagonal. In this case, due to the small energy gaps within the Chl-b band, the cross-peaks are more clearly visible in the relaxation spectra than in the non-rephasing spectra, and can be seen in the left-hand column of Figure 2.3a-d. On the picosecond timescale, the cross-peak is no longer evident as seen in Figure 2.3e.

Energy transfer from the Chl-b band to the Chl-a band also shows a several hundred femtosecond component. In the $T=300\text{ fs}$ spectrum in Figure 2.3, the cross-peak showing transfer from the Chl-b region to the mid-energy Chl-a region, CP5 ($\omega_{\tau}=15,290\text{ cm}^{-1}$; $\omega_{\tau}=14,880\text{ cm}^{-1}$), has grown in strongly as compared to the $T=200\text{ fs}$ spectrum. Over the next several hundred femtoseconds CP5 slowly decays, as presented in Figure 4b. The cross-peak from the Chl-b band to the low energy Chl-a region, CP4 ($\omega_{\tau}=15,290\text{ cm}^{-1}$; $\omega_{\tau}=14,745\text{ cm}^{-1}$), grows in significantly at $T=360\text{-}400\text{ fs}$. The decay of CP5 begins shortly after. CP4 strengthens further over the next hundred femtoseconds. The relative evolution of these two peaks again demonstrates a multi-step relaxation mechanism where Chl-b absorbed energy transfers to the lowest energy state both directly and through mid-energy Chl-a states. The integrated regions for these two cross-peaks in Figure 4b and their similarity to the integrated regions for CP2 and CP3 show that there are fairly comparable dynamics for both sets of cross-peaks. In other words, the same multistep relaxation process out of the intermediate region, seen in the anticorrelated behavior of CP2 and CP3, also occurs out of the Chl-b band, seen in the anticorrelated behavior of CP4 and CP5.

Differences in the rates of transfer into the Chl-a band from the intermediate and Chl-b regions can also be seen in the traces of Figure 2.4. In Figure 2.4a, the later rise of CP4, as compared to CP2 over the 200-300 fs range, suggests slower transfer from the Chl-b band than from the intermediate region. The slightly earlier decrease of CP3 than CP5 in Figure 2.4b also indicates faster intermediate region to Chl-a transfer. Although transfer out of the intermediate region and the Chl-b band display similar stepwise relaxation through the Chl-a region, the greater energy gap gives rise to slower transfer from the Chl-b band than from the intermediate region into the mid-energy Chl-a peak. While both sets of cross-peaks along the two ω_{τ} bands (CP2 & CP4 and CP3 & CP5) often exhibit similar dynamics, the differences seen in this stepwise relaxation, as well as in earlier energy transfer times, corroborate the theoretical model which predicts that these regions correspond to separate states and thus display separate dynamics. The differences in their dynamical evolution are also seen clearly in the early time behavior as shown in the traces of Figure 2.4a.

On the picosecond timescale, a long-lived intermediate state, appearing at the red edge of the Chl-b absorption, and indicated as CP6 ($\omega_{\tau}=15,250\text{ cm}^{-1}$; $\omega_{\tau}=14,880\text{ cm}^{-1}$), in Figure 2.3e, right, shows an alternate pathway of energy transfer from the red edge of the Chl-b band to the Chl-a band. As shown by the decay of CP3 and CP5 in Figure 2.4b, energy transfers out of the mid-energy Chl-a band by 500 fs. At one picosecond, another cross-peak has emerged showing relaxation into a state in the mid-energy Chl-a region, the energy remains trapped in this state and the strength of CP6, which is the cross-peak corresponding to this process, decays with the overall signal. All picosecond spectra (1-

20 ps) display the same cross-peak, whose only evolution is the overall signal decay. The T=13 ps spectrum is presented as an example to illustrate the intermediate state during this time range. This suggests the existence of access to the lowest energy state via alternate states, in this case most likely a monomeric chlorophyll spatially and energetically separated from the lowest energy states.⁸ The location of this molecule could select for distinct energetic transfer pathways, as opposed to a step-down relaxation through all states available in the complex. The excitation is channeled to the low energy state based also on spatial proximity as opposed to simply across the smallest possible energy gap.

2.5 Discussion

We base our discussion of energy relaxation pathways on the Hamiltonian developed here and also on the dynamical modeling of Novoderezhkin, et. al.⁸ which uses the 2.72 Å LHCII structure of Liu et al.⁵ The exciton energies used for analysis are those determined through the coherent beating signal in a recent study,³¹ while the pigment participations, and resultant site basis attributions for energy flow, are those from the Hamiltonian developed in this work. This model will be discussed in the theoretical discussion later in this manuscript. We use the monomeric LHCII as a subunit to discuss the absorption and energy transfer dynamics of LHCII. This is a reasonable starting point as only one coupling greater than 10 cm⁻¹ was calculated between monomers (35.7 cm⁻¹ between two Chl-b molecules), while within the Q_y region, strong intramonomeric electronic couplings of over 100 cm⁻¹ exist.⁴ Although neglect of this Chl-b – Chl-b coupling yields a red shift in the exciton energies of the Chl-b band, the strong couplings between Chl-b and Chl-a, and the major Chl-a to Chl-a couplings, are limited to within an individual monomer. Therefore, the Chl-b to Chl-a and Chl-a to Chl-a relaxation pathways are essentially localized on the monomer. In this paper, we confine ourselves, with the exception of a few brief comments, to the dynamics of these relaxation steps. The site basis contributions to each spectral region, grouped into the strongly coupled clusters of chlorophyll as shown in Figure 2.2a, are averaged over disorder and plotted in Figure 2.2b. In this figure, the effect of fast nuclear motion on the lineshape is only included as a linear shift in transition energies. Although each pigment contributes to absorption across a range of energies because of both static disorder and participation in multiple excitons, the region at which it absorbs begins to provide a basis for isolating the energy transfer dynamics into the contributions from individual pigments. The energy transfer pathways discussed within the following paragraphs are summarized in Figure 2.5. The major site basis contributions to each exciton are indicated in the figure. The timescales written indicate the time of the approximate maximum of the amplitude of the portion of the cross-peak corresponding to that energy transfer step.

2.5.1 Chl-a -> Chl-a

The electronic coupling between chlorophyll molecules in LHCII is strong enough that most of the exciton states have significant amplitude on two or three chromophores. The strong interaction (~20-100 cm⁻¹) and consequently significant energetic splitting between the excitons localized within several groups of pigments

allow large energy ‘jumps’ by relaxation within an excitonic manifold as was observed (between effective dimer pairs) in the Fenna-Matthews-Olsen (FMO) complex, another photosynthetic complex that has been studied with 2D spectroscopy.¹⁸ In other words, spatial overlap between exciton states is more important in controlling the pathway of energy flow than stepwise transfer down the energetic ladder. For LHCII, the strongly coupled groupings obtained from Novoderezhkin, et al.⁸ are circled in Figure 2.2a.

An example of the phenomenon of strong coupling between chlorophylls and the resultant splitting in energy levels allowing large energetic steps in the relaxation pathways is seen in transfer out of the intermediate and mid-energy Chl-a region and into the lowest energy excitons in the Chl-a manifold. According to the Hamiltonian used to simulate the spectra, one of the higher energy Chl-a excitons ($k=5$) is found on the a610-a611-a612 trimer. The pigment-based oscillator strength from the trimer on the high energy side of the Chl-a peak is also shown in Figures 2.2b with the amplitude in green and the dynamical relaxation is indicated in Figure 2.5. The other two exciton levels on the trimer are the two lowest excitons ($k=1, 2$) of the 14 excitons in the monomeric LHCII model. The large spatial overlap gives rise to fast relaxation between these excitonic states. As seen in Figure 2.3a & b, CP1 connects the mid-energy Chl-a ($k=5$) with the lower energy portion ($k=1, 2$) on a sub-100 fs timescale, as expected for processes expedited through spatial overlap. The highest energy exciton ($k=5$) on the trimer also contributes to the intermediate region in some realizations over static disorder, which would appear as similarly rapid transfer out of the intermediate region to the middle Chl-a (the middle energy exciton on the trimer), CP3, and low energy Chl-a (the lowest energy state), CP2. The rates for one such realization were calculated theoretically by Novoderezhkin, et al.¹⁰ The theoretical rate predictions for one typical realization over static disorder produced energy transfer rates between spatially overlapped excitonic states at around 100 fs. In the case of the three excitons localized on the chlorophyll trimer, which in this realization are $k=1, 2$, and 8, the time constants are $\tau_{8 \rightarrow 2}=90$ fs and $\tau_{8 \rightarrow 1}=220$ fs. The cross-peaks corresponding to these two pathways would therefore appear in a 2:1 amplitude ratio corresponding reasonably well to the CP3:CP2 amplitude in the 30 fs spectrum.

According to the model for monomeric LHCII, two of the cross-peaks which appear in under 100 fs correspond to transitions within the two excitons on the Chl-a dimers. Based on the exciton energies of the model, the dimer on the stromal level (a602-a603) contributes to CP1, which exhibits energy transfer within 50 fs. The amplitude of this peak continues to increase rapidly until ~ 150 fs. This dimer is more weakly coupled than other clusters (17.4 cm^{-1}), leading to more localized excitonic states and therefore slower energy transfer than other intra-cluster relaxation steps. The increase in the amplitude of CP1 between 50-150 fs could arise from the transition on this stromal dimer. According to the model, the site basis transition energies of the luminal dimer (a613-a614) are higher, so relaxation within this dimer would appear in CP3. This cross-peak connects the intermediate and mid-energy Chl-a region ($k=7$ to $k=4$), and shows significant amplitude in the 70 fs spectrum. The contribution of Chl 613 and 614 to energy transfer between the intermediate and mid-energy Chl-a regions is also consistent to the proposed mixed specificity of these chlorophyll binding sites, with mid- and high-energy Chl-a and low energy Chl-b.⁷ In order to reduce the complexity of the system we preferred to maintain the Chl-a specificity of the Chl 613 and 614 sites

proposed by the crystal structure of LHCII.^{5,6} The theoretical calculations of Novoderezhkin, et al.⁸ predict intra-dimer energy transfer of $\tau_{4 \rightarrow 2} \approx 300$ fs and $\tau_{7 \rightarrow 3} \approx 150$ fs (for excitons generated in one typical realization over static disorder) for the stromal and luminal dimers, respectively. The ratio of the rates from the spectra is similar to that found theoretically, however, the rates themselves seen experimentally are faster than those predicted or seen with other techniques. The sub-100 fs dynamics found here, which are observable due to the shorter pulse duration in our experiment, are evidence for short-time energy transfer. Previous theoretical investigations lacked the data to which a short-time dynamical model could be matched. The mismatch between the faster rates observed in our experiment and the theoretical simulations could arise from neglect of relaxation between vibronic levels and correlated motion at two or more sites in the protein bath which could contribute to coherence transfer processes.¹⁹

The next group of energy transfer processes appears over the course of several hundred femtoseconds and is thought to occur between nearby clusters of chlorophylls. CP1, the mid-energy Chl-a band transferring to the low energy Chl-a band, shows a slower rise from ~ 150 -250 fs. This likely arises from transfer from the lower energy state of the luminal (higher energy, a613-a614) dimer to the stromal trimer and dimer. CP3, the intermediate region transferring to the mid-energy Chl-a region, also shows an increase from 210-280 fs. In this case, the higher energy exciton on the luminal dimer ($k=7$) could transfer to the stromal dimer ($k=6, 3$) and stromal trimer ($k=5, 1, 2$). Additionally, the complex displays a multistep relaxation that would agree with a relaxation route through the stromal dimer to the stromal trimer. CP2, the intermediate region to low energy Chl-a peak, rises to a maximum at ~ 440 fs, concomitant with the decay of CP3, the intermediate region to the mid-energy Chl-a peak.

Greater spatial as well as spectral separation leads to much slower energy transfer mechanisms illustrated by CP6 in Figure 2.3e. Upon occupation of the model's highest energy Chl-a exciton ($k=8$), located mostly on a604, the excitation remains in this state for much longer than any other step in the relaxation pathway. Very slow relaxation out of this state to lower energy states in the Chl-a band is seen in the delayed appearance of CP6. Photon echo peak shift experiments by Agarwal, et al.¹² also showed a distinctly slower component of Chl-a-Chl-a energy transfer compared to the fast initial energy transfer detected. The slow timescale of this decay was probed directly with TA experiments.¹⁰ The series of 2D spectra clearly shows population continuing into the picosecond region in this long-lived intermediate, or "bottleneck" state as illustrated in the $T=13$ ps spectrum. Some population remains in the intermediate state as the signal dies at $T=20$ ps. These picosecond transitions to lower energy Chl-a excitons ($k=1, 2, 3, 6$) are also shown in Figure 5. The model of Novoderezhkin predicts slow transfer out of this intermediate state. The exciton predominantly localized on a604 ($k=8$) is essentially monomeric and the spatial distance to lower energy excitonic wavefunctions creates a bottleneck state in the model. This step of energy transfer proves to be the slowest step in the relaxation pathways in the complex though the 20 ps extent of the 2D spectroscopy cannot pinpoint the exact decay constant.

2.5.2 Chl-b \rightarrow Chl-b

The Chl-b exciton levels in the Novoderezhkin et al. model are rather extensively

mixed⁸ in the highest six excitons, and this produces energetically close states with large spatial overlap, so relaxation between them is very fast (Figure 2.3a-d, left). The similar rates and spectral congestion preclude more precise identification of different energy transfer pathways. By one picosecond, energy has transferred out of the Chl-b band almost entirely, so that the Chl-b to Chl-b cross-peaks disappear (as seen in the T=13 ps spectrum in Figure 2.3e).

2.5.3 Chl-b -> Chl-a

The role of excitonic spatial overlap in facilitating relaxation over a large energy gap is also important in explaining Chl-b to Chl-a energy transfer. Because relaxation rates scale with spatial overlap, two distinct pathways between the Chl-b and Chl-a manifolds occur. The structural arrangement of the chromophores into the stromal and luminal layers produces parallel pathways of relaxation located on each of them.

The previously unobserved sub-100 fs component of energy transfer between the Chl-b and Chl-a bands, revealed in the growth of CP4 and CP5 in Figure 2.3a and b, has several potential contributions. In addition to Chl-b contributions, ultrafast relaxation of Chl-a vibrational states that are similar in energy to Chl-b states could contribute to these cross-peaks as the Chl-a bandshape shows a significant vibronic contribution isoenergetic with the Chl-b region.³² Examining the electronic transitions of the model, the strong Chl-b to Chl-a coupling within the complex results in excitons delocalized over both chlorophyll species. On the luminal level, Chl-a, a604, is strongly coupled to its neighboring Chl-b, b605. The resultant splitting yields a lower energy exciton (k=8) localized mostly on the Chl-a and a higher energy exciton (k=10) localized mostly on the Chl-b. The spatial overlap from the two delocalized states over the two sites gives rise to fast relaxation over the Chl-b to Chl-a energy gap, which could contribute to the previously unobserved component of energy transfer from Chl-b to the mid-energy Chl-a band in the 30 fs spectrum (CP5). In the picosecond spectra (e.g. Figure 3e), CP6, which corresponds to where energy transfer from the other two luminal Chl-b molecules would appear in the model, also emerges clearly once the excitation remains trapped on a Chl-a, a604. The appearance of this cross-peak first in the 1 ps spectrum indicates that some relaxation steps occur on a much longer, or picosecond, timescale.

On the stromal level, another pathway could contribute to the sub 100 fs Chl-b to Chl-a energy transfer. Within 100 fs, CP4, transfer from Chl-b to low energy Chl-a, has weak amplitude. The very rapid dynamics could arise from the strong coupling (71.6 cm^{-1}) between Chl-b 609 and Chl-a 603. Other Chl-b molecules within the trimer of which b609 is a part are also strongly coupled (47 cm^{-1} , -21.9 cm^{-1}) to the dimer of which a603 is a part. This strong coupling leads to spatial overlap between these two excitonic states, and thus a potential sub-100 fs relaxation pathway.

The spatial overlap and resulting splitting produces a two step pathway for energy to travel from Chl-b to the exit site. Energy can transfer from the Chl-b bands to the low energy excitons via the higher energy dimer exciton (k=6) or the higher energy trimer exciton (k=5) as shown in Figure 2.5. Energy transfer into the mid-energy Chl-a peak (CP5) reaches a maximum around 290 fs, and then decays. One of the things that leads to this decay is transfer out of the mid-energy Chl-a band to the lower energy Chl-a states. Concurrent with this decay is the growth of a cross-peak, CP4, between the Chl-b

band and the low energy Chl-a, which continues to grow from 350-500 fs (the first part of this process is shown directly in Figure 4b). The energy probably transfers first into the mid-energy Chl-a states because of the small energy gap, and then exploits the spatial overlap to transfer down to the lowest energy excitons ($k=1,2$) in the complex, as mapped out in the discussion of energy transfer within the Chl-a manifold.

2.5.4 Theoretical Discussion

In Figure 2.6, we compare the experimental and calculated non-rephasing spectra at $T=200$ fs along with the experimental and calculated linear absorption spectra. In general, the simulated 2D spectra display the features seen in the experimental results, corroborating the working Hamiltonian developed here as representing the electronic structure reasonably well. The theoretical calculation accurately reproduces the emergence of two distinct cross peaks between the Chl-a and Chl-b bands (CP4 and CP5), clearly showing the relaxation to two separate regions within the Chl-a band. The horizontal band along the lowest energy states in the theoretical spectrum displays transfer into the low energy states from all initially excited levels in accord with experiment. In addition, the experimental multi-step relaxation mechanisms within the complex are reproduced theoretically, when the two bands of cross-peaks eventually turn into a single low-energy band. We do, however, see mechanisms on different timescales than in the experimental spectra perhaps due to an inaccurate bath model. Relaxation between vibronic states as well as correlated bath motions are neglected here, though recent work has indicated correlations between the environments of individual binding sites are important in photosynthetic complexes.³³

The Chl-b band displays significantly less oscillator strength in the simulated non-rephasing spectrum than in the experimental one in Figure 2.6. Coherence effects appear along the diagonal in non-rephasing spectra, so variations in oscillator strength could result from the weaknesses in the bath model. Additionally, the Chl-b band is red-shifted in the simulated spectra, which has been found previously to arise from neglect of inter-monomer coupling.⁸ The match in the linear absorption spectra could arise from the long vibronic tail effectively red-shifting the peak of the Chl-b band in the experimental linear data.

Generating simulated spectra which reproduced the experimental results reasonably well required adjusting the site energies from the previously determined model Hamiltonian⁸ to better match the data. The new site energies produce two distinct peaks in the Chl-a region, a feature lacking in simulations that use the site energies of Ref. 7. With the latter model, the 150 cm^{-1} energy gap between the two bands within the Chl-a region seen in the 2D spectra was not reproduced in simulations. 2D non-rephasing spectra in particular, because they show elongation in the antidiagonal direction, allow for easier identification of exciton position and clearer visualization of the double peak structure.

The new site energies can also produce energetically separated excitons located on the same chromophores. These increased intra-cluster energy gaps also give rise to smaller energy differences between clusters, facilitating cluster-to-cluster transfer. Overall, we see more evenly spaced excitonic energies resulting from greater variation in the site energies used to match the experimental results.³¹ Additionally, the resultant

excitonic structure contains nearby or overlapping states in different spectral regions causing cross-peaks to emerge very rapidly, as seen in the dynamics of the experimental spectra. Despite the improvements made here, the limitations in the simulations and the remaining mismatch between the experimental and calculated results indicate that the Hamiltonian requires further refinement.

2.5.5 Inter-Complex Transfer

It is interesting to compare the low energy states of LHCII and the FMO complex^{10,18}, two light harvesting complexes that have been studied in detail by a variety of spectroscopic methods including 2D spectroscopy. The two complexes have rather different functions and this is represented in their excitonic structure. FMO functions as an excitonic wire connecting the chlorosome to the reaction center. The lowest energy state is proximal to the reaction center and is localized on an essentially monomeric exciton (site 3).^{18,34} In contrast, LHCII sits in a network of light harvesting complexes comprising the antenna portion of the Photosystem II supercomplex. Its function would not be well served by having the excitation be rapidly focused onto a single Chl-a molecule. On the contrary, by having the lower energy states delocalized over a number of molecules, energy transfer may be facilitated over a broad range of exit directions enabling both LHCII→LHCII transfer and LHCII→minor complex transfer within the supercomplex. Our analysis shows that this is indeed the case as we now demonstrate.

Figure 2.7 shows the calculated inverse participation ratio – a measure of excitonic delocalization³⁵ – averaged over 2,000 realizations of static disorder. The figure was generated with the modified Hamiltonian used for the theoretical simulations. The inverse participation ratio (P_α^{-1}) of an exciton α is expressed in terms of its wavefunction ϕ_α ,

$$P_\alpha^{-1} = \frac{1}{\sum_m |\phi_\alpha(m)|^4}$$

where m indexes the site energies.³⁵ As shown in Figure 2.7, the two lowest energy excitons are clearly the most delocalized. In a typical single realization over static disorder, excitons 1 and 2 have inverse participation ratios of 2.86 and 2.00, respectively. Proposed inter-complex transfer pathways are located on the trimeric site over which these two excitons are delocalized.² For example in Ref. 2, Chl-a 612 is found to be ~17 Å from Chl 11 of the PSII core complex inner subunit CP43,² and Chl-a 610 is also thought to be important in intercomplex energy transfer.¹⁰ The two lowest energy excitons, at 14,700 cm⁻¹ and 14,770 cm⁻¹,³¹ are separated by an energy gap of less than k_BT at room temperature. This small energy difference, and the large spatial overlap between the states, allows for rapid transfer between them. Because both states have non-negligible amplitude on the chlorophylls thought to participate in the exit pathway (the chromophores are located on the external edge of the complex), they can both serve as donors in inter-complex energy transfer.

While the two lowest energy states overlap spatially, they are oriented at different angles in the membrane plane. This angle between them allows for energy transfer from the LHCII exit site in a range of directions and to a range of acceptor state transition dipole angles. Figure 2.8 shows the donor-acceptor coupling magnitude integrated over all acceptor angles for excitons 1 and 2 directed outward from the exit site. Since the two

excitons are optimized for transfer in different directions, together they allow for energy to exit LHCII across a broad distribution of angles. This is ideal for transfer to the various relative positions of nearby complexes, as shown in Figure 2.8. Energy transfer between complexes can be described by Förster theory when they are separated by a distance larger than the exciton size.³⁶ The resulting rates depend on a coupling factor based on the relative geometry and distances of the donor and acceptor states. In the case of the LHCII exit site, where the donor-acceptor distance is the same order of magnitude as the extent of the wavefunction, an accurate description of the coupling factor is given by the potential calculated with the distributed dipole approximation³⁷,

$$V = \sum_{m,n} \frac{\lambda_m \lambda_n \kappa_{mn} |\mu_m^I| |\mu_n^I|}{r_{mn}^3}$$

where m and n are the sites that give rise to the donor and acceptor wavefunctions respectively, λ_m is the coefficient corresponding to the contribution for that site to the excitonic wavefunction, and r_{mn} is the donor-acceptor distance. A result of this equation is that when two donor excitons have different site basis participations, the coupling factors are optimized for excitation energy transfer in different directions relative to the two donor transition dipoles. This effect comes from the need to look at the distances and relative angles between not only the donor exciton and the acceptor, but also between the site basis contributions to the donor exciton and the acceptor. This is clearly seen in Figure 8. In this equation, the angular dependence is given by κ_{mn} ,

$$\kappa_{mn} = \cos(\theta_{mn}) - 3 * \cos(\theta_{mr}) * \cos(\theta_{nr})$$

where θ_{mn} is the angle between the transition dipoles of sites m and n and θ_{mr} is the angle between the transition dipole of site m and the interchromophore vector between sites m and n. For transfer from site m of the donor wavefunction to site n of the acceptor wavefunction, the orientational factor can be rewritten as:

$$\kappa = \cos(\theta_{\mu_m - \mu_n}) - 3 * \cos(\theta_{\mu_m - R}) * \cos(\theta_{\mu_m - R} - \theta_{\mu_m - \mu_n})$$

The distributed dipole coupling factor was calculated for dipoles projected into the membrane plane as a function of radial distribution around the exit site ($\theta_{\mu k-R}$, for exciton k) and acceptor angle ($\theta_{\mu k-A}$) with LHCII exciton 1 as the acceptor. It was assumed that there was no displacement perpendicular to the membrane plane. Because these complexes are held within the thylakoid membrane, the orientational coupling factor was determined as a function of the angle between the exciton m and acceptor dipoles, calculated for all angles, and the acceptor position, placed 60 Å from the point in between the center of excitons 1 and 2 and scanned for all physically relevant angles. In order to examine only the angular contributions to the coupling factor, the values from both excitons were normalized and summed. Figure 2.9 shows the relative strengths of the orientation factors for excitons 1 and 2 for all acceptor angles at each of the inter-nuclear directions, and also the sum of the two excitons' contributions. Depending on its placement within the PSII supercomplex, LHCII transfers to other LHCII complexes, to other monomers within the complex, to one of multiple minor complexes, or to core complex inner antenna subunits.² As shown in the sum of orientational factor contributions, the delocalized low energy states, and resultant two potential donors, serve to optimize donor-acceptor overlap across all directions and angles in the membrane plane. From this design, the energy transfer pathway is more robust to variations in acceptor state angle and position.

2.6 Conclusions

2D electronic spectroscopy maps the dynamical behavior of a system as a function of both excitation and emission frequencies. This is particularly useful in examining photosynthetic systems in which the manifold of closely-spaced electronic states and broadening through static disorder yield highly congested spectra. By extending the measured signal into a second frequency dimension, previously unresolved dynamical evolution and peak location are identified. Non-rephasing signals allow further isolation of energy transfer peaks since dynamics of positive, off-diagonal features arise from energy transfer processes without coherent contributions.

The 2D spectra presented here illustrate the pathways along which LHCII, as the major light harvester in plants, collects energy from its pigments. The coupling between the pigments produces delocalized excited state wavefunctions through which the complex guides energy to exit states, the characteristics of which are optimized for transfer to nearby complexes. Theoretical models of experimental results show that energy transfer from Chl-b to Chl-a occurs first within each layer (lumenal and stromal) of chlorophylls, and then from the lumenal to the stromal layer, where the lowest energy excitonic states are localized. These types of parallel energetic pathways where the complex exploits the spatial overlap of delocalized excited states to relax across large energy gaps has been seen in other photosynthetic complexes¹⁸ and could contribute to the efficiency of photosynthetic energy transfer. The existence of multiple pathways located on different regions of the complex allows for the most direct route to the exit states.

The energy transfer pathways seen here are partially determined by the gradation of site basis transition energies. The Chl-b molecules on the outer edges of the LHCII monomer and the higher energy Chl-a molecules on the lumenal layer conduct the excitation to the centrally-located, lower energy exit site on the stromal layer. The more evenly spaced manifold of excitonic states produced by the site energy adjustments in this work agrees qualitatively with a recent study in which coherent beating was exploited to determine the exciton energies in LHCII.³¹ Furthermore, the work of Renger and co-workers has described the various factors within the surrounding protein matrix that alters the local environment, and therefore changes the site-basis transition energies for FMO.³ Similar calculations for the LHCII complex would indicate more definitively how the local environment shifts the site energies to produce the variation within and between clusters which results in the directional pathways of energy flow.

In extending these design principles to artificial light-harvesting systems, delocalized excited states could be applied in synthetic systems to facilitate ultrafast relaxation and more robust energy transfer between light harvesting complexes. The delocalization of the excited state wavefunctions plays an important role in inter- and intra-complex energy flow by producing multi-step relaxation pathways which effectively channel energy absorbed by many states to the exit states and then to nearby pigment protein complexes. The highly specific molecular interactions and local environment of each site which determine the photosynthetic relaxation pathway could be applied in synthetic devices to optimize their quantum efficiency.

2.7 References

- (1) Blankenship, R. E. *Molecular mechanisms of photosynthesis*; Blackwell Science: Oxford ; Malden, MA, 2002.
- (2) Nield, J.; Barber, J. *Biochimica Et Biophysica Acta-Bioenergetics* **2006**, *1757*, 353.
- (3) Adolphs, J.; Renger, T. *Biophysical Journal* **2006**, *91*, 2778.
- (4) Frahmcke, J. S.; Walla, P. J. *Chemical Physics Letters* **2006**, *430*, 397.
- (5) Liu, Z. F.; Yan, H. C.; Wang, K. B.; Kuang, T. Y.; Zhang, J. P.; Gui, L. L.; An, X. M.; Chang, W. R. *Nature* **2004**, *428*, 287.
- (6) Standfuss, R.; van Scheltinga, A. C. T.; Lamborghini, M.; Kuhlbrandt, W. *Embo Journal* **2005**, *24*, 919.
- (7) Remelli, R.; Varotto, C.; Sandona, D.; Croce, R.; Bassi, R. *Journal of Biological Chemistry* **1999**, *274*, 33510.
- (8) Novoderezhkin, V. I.; Palacios, M. A.; van Amerongen, H.; van Grondelle, R. *Journal of Physical Chemistry B* **2005**, *109*, 10493.
- (9) van Amerongen, H.; Valkunas, L.; van Grondelle, R. *Photosynthetic excitons*; World Scientific: Singapore ; River Edge, N.J., 2000; Vol. Ch. 8. Exciton Dynamics.
- (10) van Grondelle, R.; Novoderezhkin, V. I. *Physical Chemistry Chemical Physics* **2006**, *8*, 793.
- (11) Rogl, H.; Schodel, R.; Lokstein, H.; Kuhlbrandt, W.; Schubert, A. *Biochemistry* **2002**, *41*, 2281.
- (12) Agarwal, R.; Krueger, B. P.; Scholes, G. D.; Yang, M.; Yom, J.; Mets, L.; Fleming, G. R. *Journal of Physical Chemistry B* **2000**, *104*, 2908.
- (13) Palacios, M. A.; Standfuss, J.; Vengris, M.; van Oort, B. F.; van Stokkum, I. H. M.; Kuhlbrandt, W.; van Amerongen, H.; van Grondelle, R. *Photosynthesis Research* **2006**, *88*, 269.
- (14) Salverda, J. M.; Vengris, M.; Krueger, B. P.; Scholes, G. D.; Czamoleski, A. R.; Novoderezhkin, V.; van Amerongen, H.; van Grondelle, R. *Biophysical Journal* **2003**, *84*, 450.
- (15) Georgakopoulou, S.; van der Zwan, G.; Bassi, R.; van Grondelle, R.; van Amerongen, H.; Croce, R. *Biochemistry* **2007**, *46*, 4745.
- (16) Gibasiewicz, K.; Rutkowski, M.; Van Grondelle, R. *Photosynthetica* **2009**, *47*, 232. Pieper, J.; Ratsep, M.; Irrgang, K. D.; Freiberg, A. *Journal of Physical Chemistry B* **2009**, *113*, 10870.
- (17) Jonas, D. M. *Annual Review of Physical Chemistry* **2003**, *54*, 425.
- (18) Brixner, T.; Stenger, J.; Vaswani, H. M.; Cho, M.; Blankenship, R. E.; Fleming, G. R. *Nature* **2005**, *434*, 625.
- (19) Zigmantas, D.; Read, E. L.; Mancal, T.; Brixner, T.; Gardiner, A. T.; Cogdell, R. J.; Fleming, G. R. *Proceedings of the National Academy of Sciences of the United States of America* **2006**, *103*, 12672.
- (20) Caffarri, S.; Croce, R.; Breton, J.; Bassi, R. *Journal of Biological Chemistry* **2001**, *276*, 35924.
- (21) Brixner, T.; Mançal, T.; Stiopkin, I. V.; Fleming, G. R. *Journal of Chemical Physics* **2004**, *121*, 4221.

- (22) Brixner, T.; Stiopkin, I. V.; Fleming, G. R. *Opt Lett* **2004**, *29*, 884.
- (23) Novoderezhkin, V. I.; Palacios, M. A.; van Amerongen, H.; van Grondelle, R. *Journal of Physical Chemistry B* **2004**, *108*, 10363.
- (24) Peterman, E. J. G.; Pullerits, T.; vanGrondelle, R.; vanAmerongen, H. *Journal of Physical Chemistry B* **1997**, *101*, 4448.
- (25) Zhang, W. M.; Meier, T.; Chernyak, V.; Mukamel, S. *Journal of Chemical Physics* **1998**, *108*, 7763. Yang, M. N.; Fleming, G. R. *Journal of Chemical Physics* **2003**, *119*, 5614.
- (26) Linnanto, J.; Martiskainen, J.; Lehtovuori, V.; Ihalainen, J.; Kananavicius, R.; Barbato, R.; Korppi-Tommola, J. *Photosynthesis Research* **2006**, *87*, 267.
- (27) Ernst, R. R., Bodenhausen, Geoffrey, Wokaun, Alexander *Principles of Nuclear Magnetic Resonance in One and Two Dimensions*; Oxford Science Publications: Oxford, 1987.
- (28) Cheng, Y. C., Fleming, G.R. *Journal of Physical Chemistry A* **2008**, *in press*.
- (29) Read, E. L.; Engel, G. S.; Calhoun, T. R.; Mancal, T.; Ahn, T. K.; Blankenship, R. E.; Fleming, G. R. *Proceedings of the National Academy of Sciences of the United States of America* **2007**, *104*, 14203.
- (30) Cheng, Y. C.; Fleming, G. R. *Journal of Physical Chemistry A* **2008**, *112*, 4254.
- (31) Calhoun, T. R., Ginsberg, N.S., Schlau-Cohen, G.S., Cheng, Y.-C., Ballottari, M., Bassi, R., Fleming, G.R. *Journal of Physical Chemistry B* **submitted**.
- (32) Rivadossi, A.; Zucchelli, G.; Garlaschi, F. M.; Jennings, R. C. *Photochemistry and Photobiology* **2004**, *80*, 492.
- (33) Lee, H.; Cheng, Y. C.; Fleming, G. R. *Science* **2007**, *316*, 1462.
- (34) Wen, J., Zhang, H., Gross, M. L., Blankenship, R. E. *Proceedings of the National Academy of Sciences of the United States of America* **in press**.
- (35) Poliakov, E. Y.; Chernyak, V.; Tretiak, S.; Mukamel, S. *Journal of Chemical Physics* **1999**, *110*, 8161.
- (36) Scholes, G. D. *Annual Review of Physical Chemistry* **2003**, *54*, 57.
- (37) Scholes, G. D.; Jordanides, X. J.; Fleming, G. R. *Journal of Physical Chemistry B* **2001**, *105*, 1640.

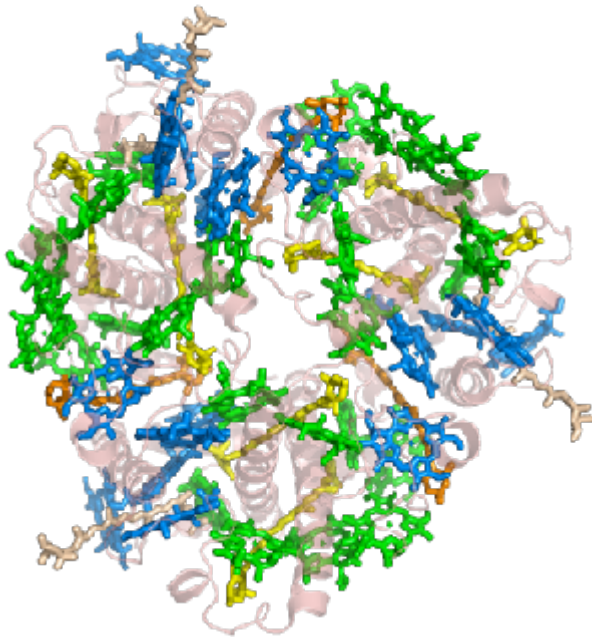


Figure 2.1. Trimeric LHCII complex which contains pigments (Chl-a in green, Chl-b in blue, carotenoids in orange for violaxanthin, yellow for lutein and off-white for neoxanthin) in a protein matrix.⁵

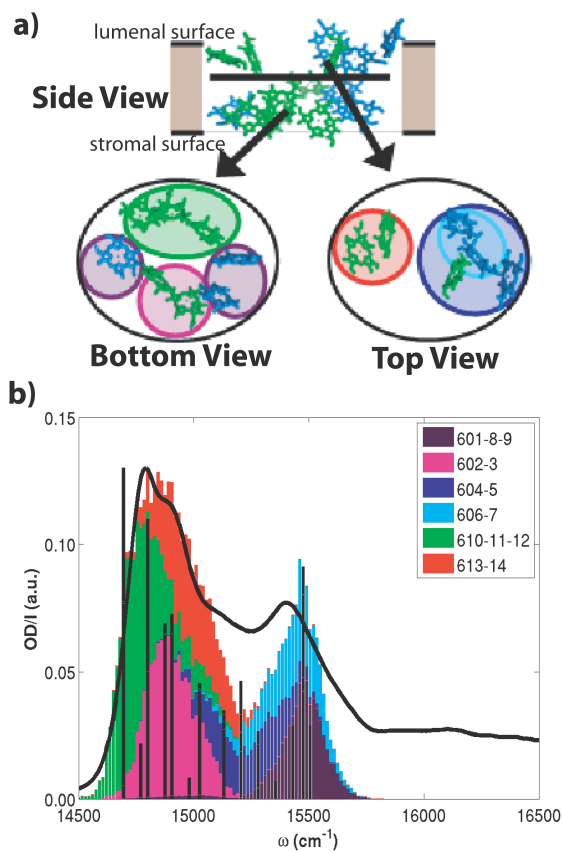


Figure 2.2. a) The chlorophyll arrangement of monomeric LHCII (Chl-a in green, Chl-b in blue). The strongly coupled clusters within the stromal layer (bottom) and luminal layer (top) are indicated and the color coding corresponds to the spectral regions labeled in b. b) The linear absorption spectrum of LHCII at 77K with the calculated site basis contributions averaged over disorder (color) for the excitons (black) plotted. The congested spectrum can be partially decomposed into its site basis contributions by identifying the chlorophylls which absorb in each spectral region (labeled according to the 2.72 Å crystal structure⁵).

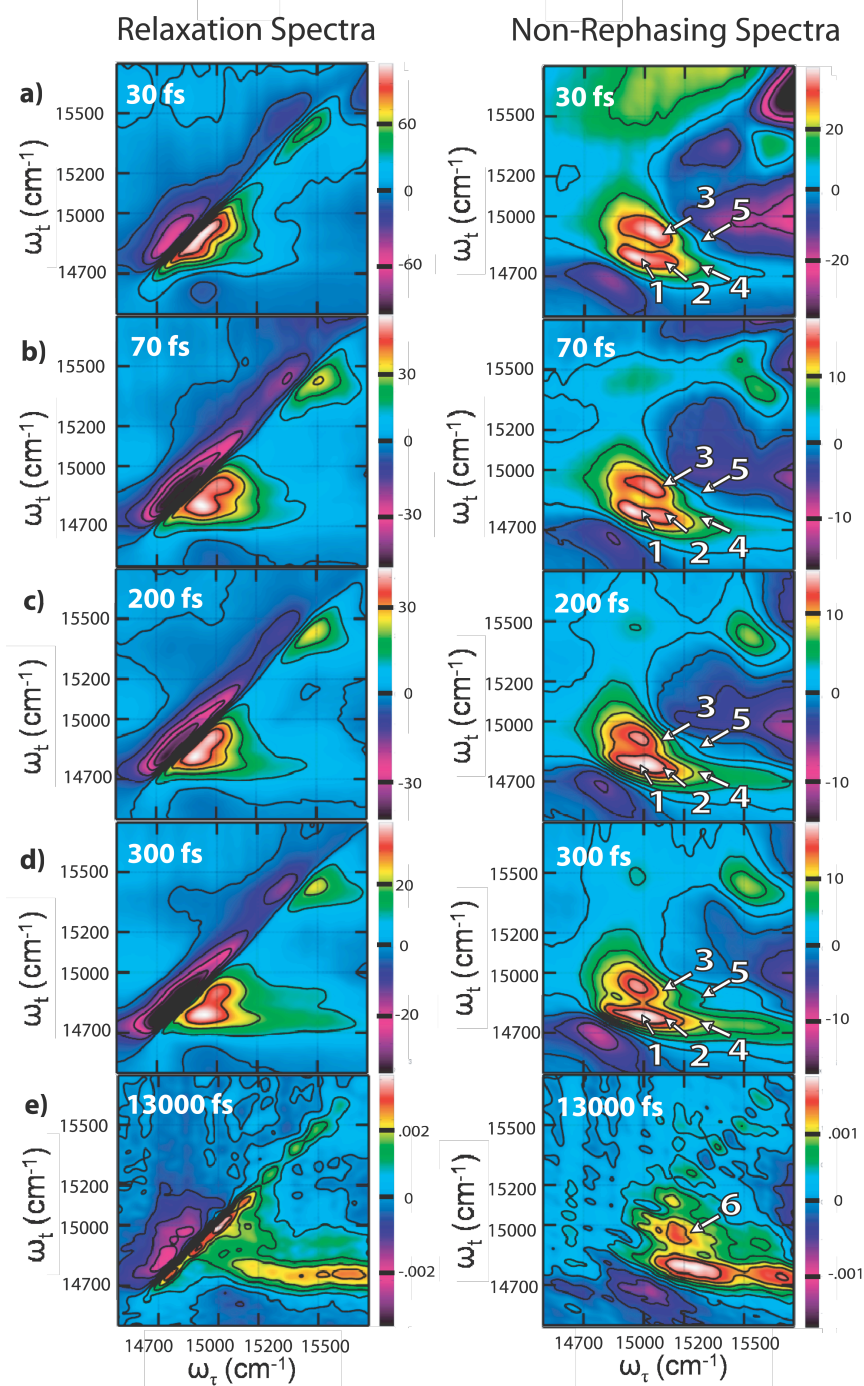


Figure 2.3. Experimental real 2D relaxation (left) and non-rephasing (right) spectra of LHCII at 77K for $T=30, 70, 200, 300$ fs, and 13 ps. Arrows point to cross-peaks on the non-rephasing spectra to highlight energy transfer dynamics and the tick marks as drawn delineate the regions of the spectrum discussed in the text.

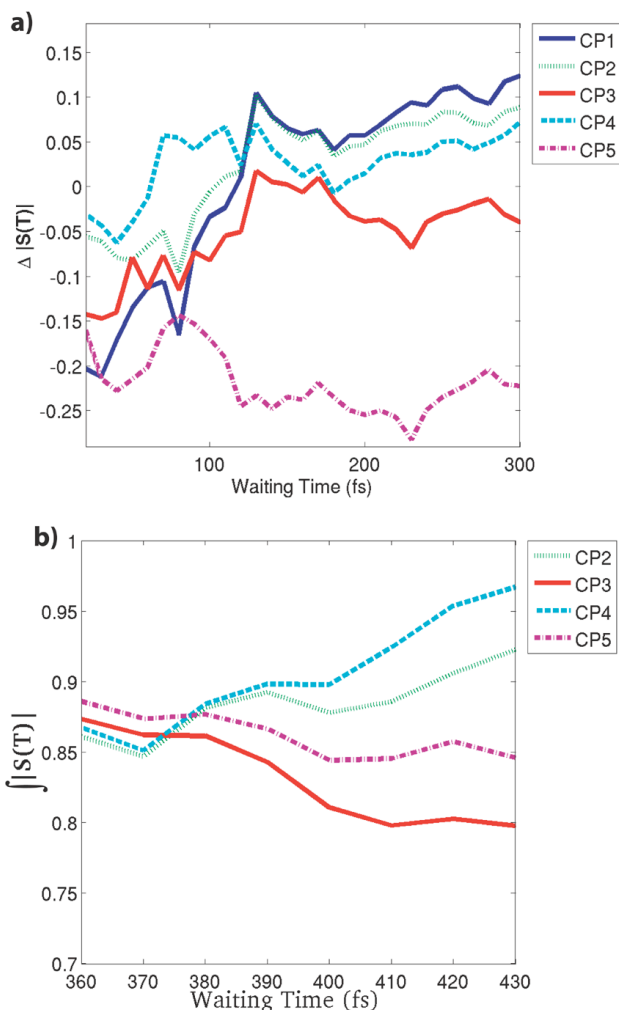


Figure 2.4. a) Integrated square regions (85 cm^{-1} per side) around each cross-peak are shown for waiting times of 20-300 fs (the 0-20 fs dynamics are not shown because they are dominated by pulse overlap effects). The normalized integrated regions are subtracted from the normalized integrated region around the low energy diagonal rephasing peak to eliminate variations at each population time and then the difference trace is smoothed. The cross-peak numbers are as shown in Figure 2.3 (CP1: mid Chl-a -> low Chl-a; CP2: intermediate region -> low Chl-a; CP3: intermediate region -> mid Chl-a; CP 4: Chl-b -> low Chl-a; and CP5: Chl-b -> mid Chl-a). b) The integrated square regions are smoothed and plotted without subtraction for CP2 – 5. The concomitant decay of CP3 & 5 and rise of CP2 & 4 indicate a multistep relaxation process.

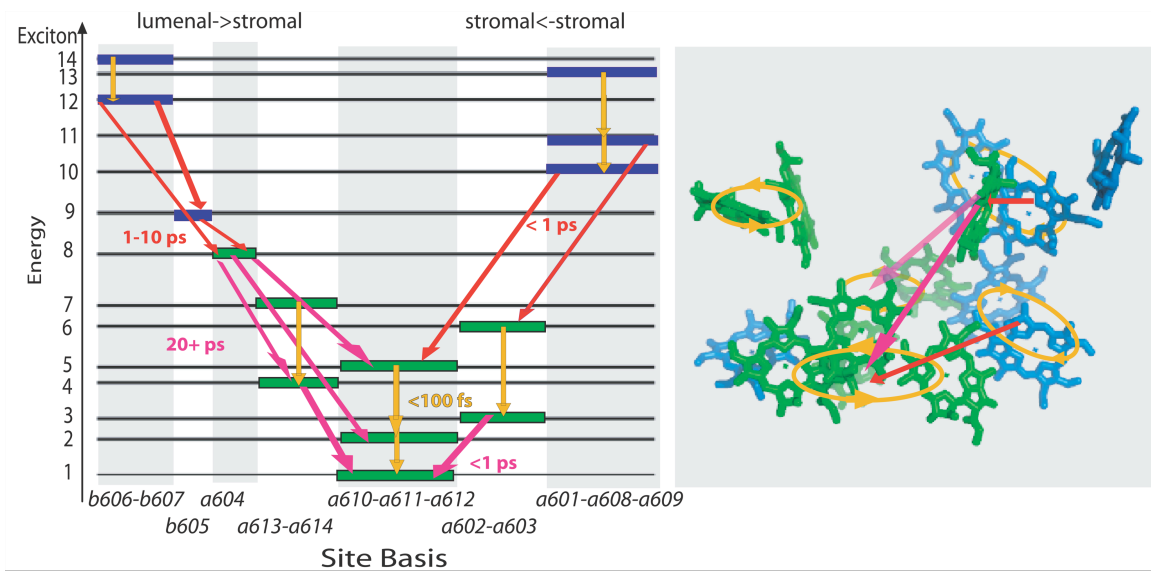


Figure 2.5. Summary of the pathways of energy flow and their locations on the crystal structure as mapped onto the crystal structure.^{5,10} The major pigments with contributions to each exciton are determined by the working Hamiltonian, and the excitonic energy is found with the electronic coherence beating signal.³¹ The timescales indicate the approximate time at which the cross-peak signal corresponding to that pathway reaches its maximum.

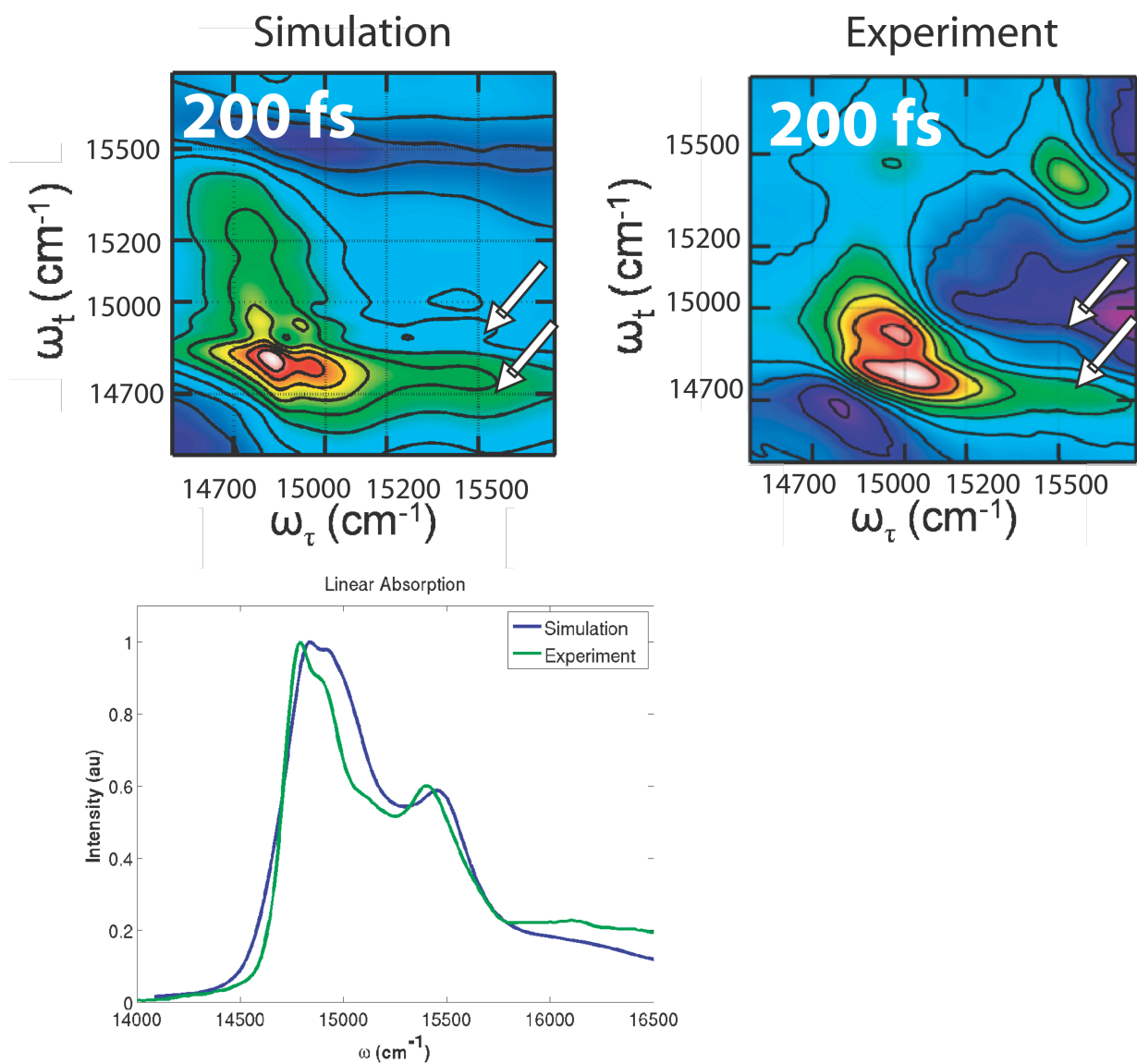


Figure 2.6. LHCII 77K normalized experimental and simulated linear absorption and real non-rephasing 2D electronic spectra shown for $T=200$. Energy transfers from Chl-b and the intermediate region into two distinct Chl-a bands, as indicated with arrows on the spectra. Most population is collected in the lowest state.

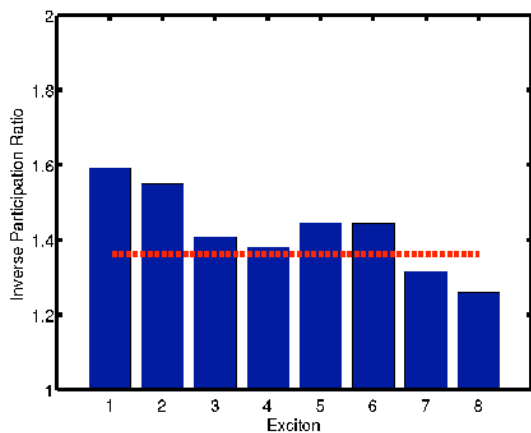


Figure 2.7. The inverse participation ratios of the excitons in the Chl-a region, averaged over 2,000 realizations of static disorder, indicate the high level of delocalization of excitons 1 and 2. The average of the inverse participation ratios of the Chl-a excitons without significant contributions from the trimeric exit site is plotted in red.

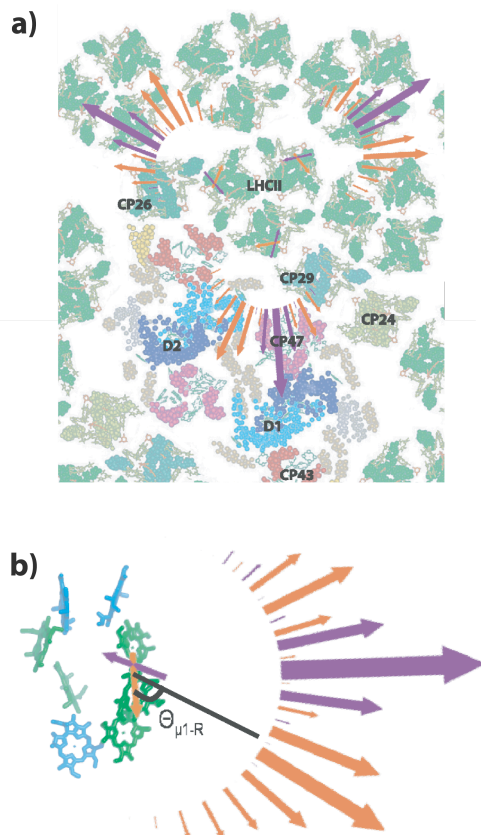


Figure 2.8. a) The magnitude of the angular contribution to the orientation factor for three monomers in an LHCII trimer is shown for exciton 1 (orange) and exciton 2 (purple), for each angle on a structural model of PSII. The positions and angles of excitons 1 and 2 are displayed on the sample LHCII trimer, in the same colors as their corresponding outcoupling factors. The length of the emergent arrows indicates the strength of the factor for the exciton to which its color corresponds integrated over all realistic orientations of the acceptor dipole. b) Outcoupling factors for an isolated monomer.

Orientalional Energy Transfer Factors

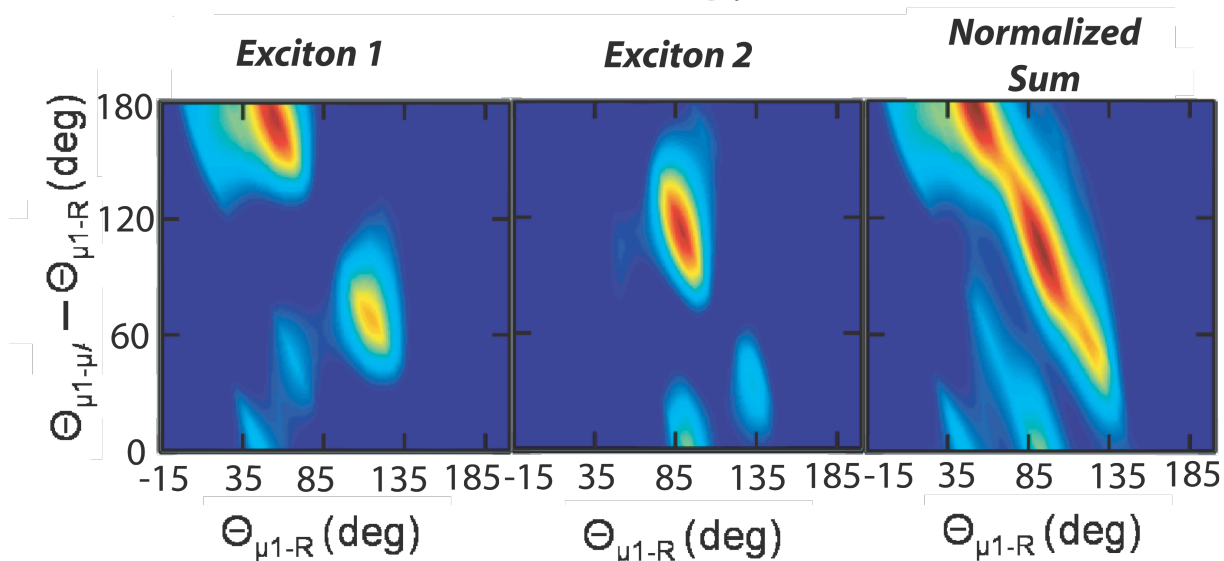


Figure 2.9. The orientational outcoupling factors for energy transfer from excitons 1 and 2 individually and the sum of both normalized contributions are plotted. The values are calculated with the distributed-dipole method. In order to compare their magnitudes across the range examined, for both exciton 1 and exciton 2 they are plotted as a function of the angle between the exciton 1 dipole and the internuclear line and the exciton 1 dipole and the acceptor dipole at a distance of 60 Å. The range was chosen based on likely orientations as determined by the position of excitons 1 and 2 within the complex.

Chapter 3

Spectroscopic Elucidation of Uncoupled Transition Energies in the Major Photosynthetic Light Harvesting Complex, LHCII

This chapter is reproduced with permission from
G. S. Schlau-Cohen, T. R. Calhoun, N. S. Ginsberg, E. L. Read, M. Ballottari,
R. Bassi, R. van Grondelle, G. R. Fleming
Proceedings of the National Academy of Science (2010), **107**, 13276-13281
© 2010 National Academy of Science

3.1 Abstract

Electrostatic couplings between chromophores in photosynthetic pigment-protein complexes, and interactions of pigments with the surrounding protein environment, produce a complicated energy landscape of delocalized excited states. The resultant electronic structure absorbs light and gives rise to energy transfer steps that direct the excitation towards a site of charge separation with near unity quantum efficiency. Knowledge of the transition energies of the uncoupled chromophores is required to describe how the wavefunctions of the individual pigments combine to form this manifold of delocalized excited states that effectively harvests light energy. In an investigation of the major light-harvesting complex of Photosystem II (LHCII), we develop a novel method based on polarized two-dimensional electronic spectroscopy to experimentally access the energies of the S_0 - S_1 transitions in the chromophore site basis. Rotating the linear polarization of the incident laser pulses reveals previously hidden off-diagonal features. We exploit the polarization dependence of energy transfer peaks to find the angles between the excited state transition dipole moments. We show that these angles provide a spectroscopic method to directly inform on the relationship between the delocalized excitons and the individual chlorophylls through the site energies of the uncoupled chromophores.

3.2 Introduction.

In photosynthetic light-harvesting, networks of pigment-protein complexes (PPC) absorb light energy and direct the excitation towards a central site where it initiates electron transfer. Under low light conditions, photosynthetic organisms complete energy transfer steps to reach the reaction center (the site of charge separation) with near unity quantum efficiency¹. The sophisticated arrangement of hundreds of chlorophyll molecules into the PPCs which form the photosynthetic apparatus produces an efficient, directional, and controllable energy flow^{2,3}. Most absorption of sunlight occurs on arrays of a single type of PPC, the major light harvesting complex of Photosystem II (LHCII). LHCII both absorbs light and transfers the resultant excitation towards the reaction center. The nanostructuring of the chromophores within each PPC fixes the relative orientation of the individual chlorophylls and their position in a surrounding protein. The low energy density of sunlight requires the light-absorbing pigments to be densely packed, and

electrostatic interactions between chromophores determine the electronic structure and dynamics.

Relating molecular structure to function through an accurate quantum dynamical theory^{4,5} requires the following inputs: 1) spatial structure; 2) electronic structure, including both site energies of the (uncoupled) chromophores and electronic couplings between chlorophylls, which in turn depend on both spatial separation and orientation; and 3) electron nuclear coupling spectrum and dynamical timescales including intramolecular and protein motions. While the spatial structure of PPCs is often available from x-ray crystallography, the couplings and site energies are inter-related and are much more difficult to obtain because they depend on the interactions between the thousands of atoms contained in a PPC. The couplings can be estimated from the spatial structure, but the site energies have remained more elusive. Their values have been accessible only through theoretical models⁶, indirectly through fitting simulations to spectroscopic data⁷⁻¹¹, or by comparing wild type and mutated species¹²⁻¹⁴. The site energies depend on tuning of the local optical and electrochemical properties by the protein environment through effects such as electrostatic interactions with amino acid side chains, ligation of the central Mg of the chlorophyll, hydrogen bonding, conformation of the pigment, and the electric field originating from the dipole of the α -helix backbone⁶. Understanding to what extent each chromophore contributes to each delocalized excited state, known as an exciton¹⁵, which requires the site energies, enables a description of how the arrangement of the pigments and proteins gives rise to the highly effective photosynthetic energy landscape. Greater variation in site energies produces greater variation in exciton energies, which yields increased spectral coverage, and a larger number of energetically distinct states to serve as intermediates in relaxation pathways.

An incisive way to obtain information on site energies is to exploit the ability to vary the polarizations of the four optical fields of a two-dimensional (2D) electronic spectroscopic measurement. 2D spectroscopy is a technique that directly correlates absorption and emission frequencies as a function of a delay between absorption and emission events for all energies within the laser bandwidth^{16,17}. Spectra are plotted as a function of absorption and emission, and cross peaks appear where the two frequencies are unequal indicating energy transfer. Rotation of the linear polarization of the incident laser pulses highlights or suppresses cross peaks to reveal off-diagonal features obscured by stronger peaks under all parallel polarizations^{18,19}. The polarization dependence of a cross peak amplitude determines the angle between the transition dipole moments (etdm) of the excitonic states²⁰, which in turn relates the excitonic states to the individual chromophores¹⁵. Here, we show the direction of etdms (which are linear combinations of those of the individual chromophores) enables an estimate of the original site energies of the uncoupled chromophores within a model of the molecular structure of a PPC.

We apply this method to LHCII, which binds over 50% of the chlorophyll in green plants. Each monomer within the trimeric LHCII complex^{21,22} contains 14 chlorophylls in two spectral variants, 8 Chl*a* and 6 Chl*b*, giving 14 closely spaced energy levels with varied, but overlapping, spectral signatures. Using two polarization sequences, we reveal energy transfer features and determine the angle between donor and acceptor etdms, a value which adds an experimental test to refine the transition energies of individual chlorophylls in previous models. From the transition energies, we can determine the electronic structure within specific regions of the molecular structure, and

thus better resolve how pigment position and orientation yields efficient, directional energy flow.

3.3 Experimental Results.

A 2D spectroscopic measurement requires four interactions with the light field, where switching the time-ordering of the first two interactions generates rephasing and non-rephasing spectra²³. Figure 3.1 displays absolute value, non-rephasing spectra of the Q_y region of the chlorophyll in LHCI under two different polarization sequences of the incident laser fields, with all-parallel (0,0,0) on the left and “cross-peak specific” ($\pi/3, -\pi/3, 0, 0$) on the right^{10, 24}. Under the cross-peak specific polarization, the signal along the diagonal corresponding to peaks in the linear absorption spectrum is removed and the relative amplitudes of off-diagonal features change^{10, 18, 24}. On the 2D spectra, tickmarks divide three regions: 1) Chla (14,700 cm^{-1} – 15,000 cm^{-1}), with a low and mid energy band; 2) intermediate (15,000 cm^{-1} – 15,200 cm^{-1}), with high energy Chla and low energy Chlb; and 3) Chlb (15,200 cm^{-1} – 15,500 cm^{-1}). Peaks below the diagonal grow in due to relaxation because in non-rephasing spectra, off-diagonal features that appear with increasing delay time arise primarily from energy transfer²⁰. Energy transfers from the intermediate, Chlb and the vibronic tail of the Chlb band into the Chla bands.

The greatest collective oscillator strength is in the Chla region where the 8 Chla molecules per monomer produce overlapping energy transfer pathways. The Chla region is characterized by two separate diagonal peaks and a cross-peak showing relaxation between these two bands, which is indicated by the white arrow in Fig. 3.1a ($\omega_{\tau}=14,900$ cm^{-1} ; $\omega_{\tau}=14,775$ cm^{-1})⁸. At 60 fs, the spectra display an increased relative intensity of this mid-energy Chla to low energy Chla peak under the cross-peak specific polarization sequence over that seen in the all-parallel spectrum.

The close spacing and broad linewidths of the 14 excitonic levels prevent many individual diagonal and off-diagonal peaks from being discernible⁸. Highlighted by white arrows in Fig. 3.1b, the region around ($\omega_{\tau}=15,400$ cm^{-1} ; $\omega_{\tau}=15,176$ cm^{-1}) contains a peak showing energy transfer from Chlb to the intermediate region under the cross-peak specific polarization, whereas only a shoulder of the Chlb to mid-energy Chla peak appears under the all-parallel polarization.

Figure 3.2 contains vertical cuts from the 2D spectra along a single excitation energy to enable a clearer examination of the relative intensity at each emission energy, and to show that these intensities change with both waiting time and polarization sequence. The coordinate for the cut is the approximate maximum of the cross-peak along the excitation axis ($\omega_{\tau}=15,400$ cm^{-1}). Figures 3.2a and b show the parallel and cross-peak specific data, respectively. The region within the black, dashed rectangle clearly shows the different scaling under the two polarization conditions. Under the all-parallel polarization, the mid-energy Chla band ($\omega_{\tau}=14,920$ cm^{-1}) appears as a broad peak with a higher energy tail in Fig. 3.2a. Under the cross-peak specific polarization, the higher energy tail is isolated into a separate peak in Fig. 3.2b. Figure 3.2c contains an expanded view under the cross-peak specific polarization. By fitting the intensity across the ω_{τ} axis (shown as the dotted lines in Fig. 3.2c) and taking the center of the Gaussian fit at all waiting times (which may be slightly red-shifted by a contribution from the tail

of the Chla peak), the emission energy, corresponding to the acceptor in this energy transfer step, was found to be at $\omega_t=15,176 \pm 60 \text{ cm}^{-1}$.

The vertical cuts also reveal dynamics of the cross-peak by allowing clear comparison between waiting times. Because of the large number of energy levels in LHCII, this peak contains more complex dynamics than a mono-exponential population and depletion and some amplitude from nearby features. Normalized vertical cuts of the polarized 2D spectra are plotted in Fig. 3.2d. The peak has clearly appeared by 100 fs, and at one picosecond the intermediate state reaches its highest relative amplitude, meaning that energy transfer into the intermediate state occurs on a sub-picosecond timescale. At 5 ps, as seen in Fig. 3.2b, the cross-peak has similar relative amplitude, suggesting it is a long-lived intermediate state.

3.4 Discussion.

2D spectra directly – and dynamically – resolve the absorption frequency-emission frequency correlation for all wavelengths within the bandwidth of the laser. Multiple Liouville pathways, corresponding to different processes within the molecular system²⁵, can all give rise to interfering peaks at the same energetic coordinates, which is particularly likely in the complex systems typical of biological processes. The cross-peak specific polarization sequence changes the relative amplitude of off-diagonal peaks, thus enabling enhancement of features obscured by overlapping peaks.

The linear polarizations of the laser pulses and the relative orientation of the etdms produce the following orientational factor, which scales the amplitude of each peak¹⁸,

$$\begin{aligned} \langle i_\alpha j_\beta k_\gamma l_\delta \rangle &= \frac{1}{30} [\langle \cos \theta_{\alpha\beta} \cos \theta_{\gamma\delta} \rangle (4 \cos \theta_{ij} \cos \theta_{kl} - \cos \theta_{ik} \cos \theta_{jl} - \cos \theta_{il} \cos \theta_{jk}) \\ &+ \langle \cos \theta_{\alpha\gamma} \cos \theta_{\beta\delta} \rangle (4 \cos \theta_{ik} \cos \theta_{jl} - \cos \theta_{ij} \cos \theta_{kl} - \cos \theta_{il} \cos \theta_{jk}) \\ &+ \langle \cos \theta_{\alpha\beta} \cos \theta_{\gamma\delta} \rangle (4 \cos \theta_{il} \cos \theta_{jk} - \cos \theta_{ij} \cos \theta_{kl} - \cos \theta_{ik} \cos \theta_{jl})] \end{aligned} \quad (1)$$

where i, j, k , and l are laser polarizations in the lab frame and α, β, γ , and δ are etdms in the molecular frame. For a given polarization sequence, the orientational factor depends only on the projection angle between the etdms of the excitons involved in a Liouville pathway²⁰. The relationship between the orientational factor and the angle between donor and acceptor etdms for energy transfer^{10,25} under all-parallel and cross-peak specific polarizations is shown in Fig. 3.3a.

The all-parallel and cross-peak specific sequences weight signals in an inverse manner and thus uncover complementary features. Transitions for which the projection angle between the two dipole moments is $\sim 90^\circ$ have a maximum intensity under the cross-peak specific polarization and a minimum under the all-parallel polarization. A cross-peak enhanced under the cross-peak specific polarization must correspond to an energy transfer process between etdms with a projection angle near 90° , because the prefactor is large enough to increase relative amplitude compared to other cross-peaks only within a fairly small range around this angle between etdms.

The cross-peak at $\omega_t=15,400 \text{ cm}^{-1}$, $\omega_t=15,176 \text{ cm}^{-1}$ arises from energy transfer into a long-lived intermediate state, a step most likely localized on the chlorophylls in green in Fig. 3.4 (Chlbs 605, 606 and 607, with numbering from the x-ray crystallography structure in ref.²¹). The relative enhancement of this cross-peak indicates

an angle between donor and acceptor etdms of $\sim 90^\circ$. The acceptor energy is in the intermediate region, between the Chla and Chlb peaks, and corresponds to the energy of exciton 9²⁶, suggesting the acceptor is the lowest energy Chlb exciton and making it an obvious intermediate in relaxation from Chlb to Chla. Previous fitting to experimental results^{7,8} found the lowest energy Chlb exciton predominantly originated from Chlb 605. Chlb 605 is coupled ($J=11.5 \text{ cm}^{-1}$, 23.5 cm^{-1}) to two other Chlb molecules, Chlbs 606 and 607, which are likely donors in the sub-picosecond energy transfer process observed here. Chlb 605 is weakly coupled to the Chla band, meaning the excitation remains on Chlb 605 for picoseconds as opposed to the femtosecond timescale of other energy transfer steps, and this behavior is seen here in the relatively constant amplitude of the cross-peak at 5 ps.

The excitation must reach the reaction center to initiate charge separation. This requires a net flux of energy out of LHCII to nearby complexes, which occurs via the excitation relaxing onto exit sites (low energy chromophores on the external edge of the complex). The observed long-lived intermediate state, as well as a second long-lived intermediate state detected previously⁸, could facilitate unidirectional energy transfer from the complex. The energy gap seen in the data between the donor and putative acceptor, Chlb 605, ($\sim 300 \text{ cm}^{-1}$) is larger than kT at room temperature ($\sim 200 \text{ cm}^{-1}$), which prevents thermal hopping between the two states. The weak coupling between the intermediate and lower energy states suppresses a long-lived superposition between chromophores, ensuring localization of the excitation onto the acceptor pigment.

The angle between donor and acceptor etdms can enable estimates of site energies. The excitonic structure, the spectroscopic observable, depends on the site-basis Hamiltonian and site-basis transition dipole moments (stdms). The off-diagonal terms of the site-basis Hamiltonian, which are the couplings between chromophores, can be estimated from electrostatic interactions based on the structure from x-ray crystallography^{7,27}. The stdms of the Q_y transition can be extracted from the position and orientation of the chlorophylls¹. Although diagonal terms (site energies) of the site-basis Hamiltonian are not directly accessible, the angle between etdms depends on the site energies, and therefore can inform on the site energies. The angle between etdms is a function of mixing angle (a function of site energy gap and electronic coupling) and stdms¹⁵. In order to illustrate the dependence of etdm direction on site energy, the angle between etdms versus site-basis transition energy gap (with fixed electronic coupling and stdms) is plotted for a model dimer system in Fig. 3.3b. The analytical form is derived and presented in Appendix B. Where the coupling between two chromophores is greater than, or on the same order of magnitude as, the difference in their site energies ($|\Delta E| \leq |J|$), the angle between etdms is highly sensitive to the site-basis transition energy gap. Due to the steep slope where $|\Delta E| \leq |J|$, the angle between etdms measures the site energy gap within the dimer system. Even though both exciton energy and etdm direction depend on the site-basis Hamiltonian, etdm direction can be a much more sensitive probe of the site energies than the excitonic energy. Etdm direction depends non-linearly on site-basis transition energies, while exciton energies mostly increase linearly with increasing site energy (shown analytically for a dimer in Appendix B). When the site energy gap of the dimer model changes from $\Delta E = -100 \text{ cm}^{-1}$ to $\Delta E = 0 \text{ cm}^{-1}$, the angle between etdms changes by about 30° (and the scaling factor is almost halved). However, with this change in site energy gap, the exciton energy changes by less than 70 cm^{-1} , which is

within the inhomogeneous linewidth of most photosynthetic PPCs. Variation in etdm direction manifests as a change in peak amplitude, which can be more visible than an energy shift in a broadened spectrum.

In order to employ this method of determining site energies from the angle between etdms, the following are required: 1) a model of the molecular structure of the participating pigments; 2) restrictions on site-energies based on experimental results from genetic mutations and spectroscopic measurements; 3) an energy gap less than or approximately equal to the coupling ($|\Delta E| \leq |J|$). This analysis also requires 2D spectroscopy because multiple combinations of site energies can give rise to the same linear absorption spectrum. In 2D spectroscopy, cross-peaks must share excitation and emission energies and timescales to overlap spectroscopically. According to the assignments presented earlier, the energy transfer step that gives rise to the uncovered cross-peak potentially involves Chl b s 605, 606, and 607 which produce three excitonic states. The acceptor state, the exciton at $15,176 \text{ cm}^{-1}$, is most likely localized solely on Chl b 605, due to its lower energy, and so larger energy gap (ΔE) relative to coupling (J) to the rest of the Chl b band, and the weak coupling and large energy gap with respect to the Chl a band. The donor energy is in the middle of the Chl b band ($\sim 15,400 \text{ cm}^{-1}$), so one or both of the remaining two excitons could be the donor state(s). One of these possible donor states is mostly localized on Chl b 606, with a contribution from Chl b 607, and vice versa for the second potential donor. While Chl b 606 is also strongly coupled to Chl a 604, the energy gap imposed by the two spectral variants prevents a large mixing of the two wavefunctions.

The approach is limited to where etdm direction is sensitive to site energies ($|\Delta E| \leq |J|$), as shown in Fig. 3.3b. Because the acceptor state is at the low energy edge of the Chl b band and essentially monomeric, we expect the Chl b 605 site energy to be lower than Chl b s 606 and 607 site energies by an amount greater than the coupling. Thus, the acceptor's etdm direction is mostly insensitive to site energies. The directions of the two potential donor etdms (produced by Chl b s 606 and 607) are sensitive to site energies, because Chl b s 606 and 607 can have a site energy gap on the same order as their coupling to each other. The dependence of etdm direction on coupling and site energy gap is illustrated in Fig. 3.4a-c with the absence of coupling, in the presence of coupling ($E_{\text{Chl}b606} = 15,680 \text{ cm}^{-1}$, $E_{\text{Chl}b607} = 15,730 \text{ cm}^{-1}$, $J_{\text{Chl}b606-607} = 23.7 \text{ cm}^{-1}$), and in the presence of coupling with different site energies for Chl b s 606 and 607 ($E_{\text{Chl}b606} = 15,780 \text{ cm}^{-1}$, $E_{\text{Chl}b607} = 15,700 \text{ cm}^{-1}$, $J_{\text{Chl}b606-607} = 23.7 \text{ cm}^{-1}$), respectively. The change in etdm direction introduced by a shift in site energy (Figs. 4b and c) displays the impact of the site energies of Chl b s 606 and 607 on the direction of the donors' etdms, and therefore on the angle between the donors' and acceptor's etdms for the cross-peak at $\omega_{\tau} = 15,400 \text{ cm}^{-1}$, $\omega_{\tau} = 15,176 \text{ cm}^{-1}$.

In order to estimate the site-energies of Chl b s 606 and 607, the angle between the etdms of the acceptor and one potential donor (localized mostly on Chl b 606) is shown as a function of the Chl b 606 and Chl b 607 site energies in Fig. 3.5a. For these calculations, a model of monomeric LHCII is employed using the Hamiltonian from ref. ⁸ and stdms from the model from x-ray crystallography ²¹. Using site-directed mutagenesis, the approximate energy of the exciton predominantly localized on Chl b 606 was determined to be $\sim 15,338 \text{ cm}^{-1}$ ¹², which corresponds most closely to exciton 11 ²⁶, and the site energies are restricted to a range that maintains the energetic ordering. These limits are

plotted in pink. The sharp turns in the pink boundaries occur when the site energies of two coupled chromophores become degenerate, because a large increase in mixing angle drastically changes the energies of excitonic states. The angle between donor and acceptor etdms is indicated by a bimodal color scheme, with angles between 70°-110° shown in yellow, reflecting the experimental precision in extracting angular information from a comparison of the spectra under the two polarization sequences. The angle between etdms of the second potential donor and the acceptor was found to be far from 90° for all physically reasonable values of the site energies of Chlbs 606 and 607 (Fig. B2). Photosynthetic complexes have a Gaussian distribution around the transition energy¹⁵, which for LHCII is thought to have a width of 85 cm⁻¹⁷. Therefore, the site energies of the chromophores must have a distribution around their values where a majority of etdm angles are ~90° (contains a majority of yellow). The region where all criteria are met (from site-directed mutagenesis, angle between etdms, and values within the distribution are mostly close to 90°) is shown in an off-white box in Fig. 3.5a. Thus, ranges on the site energies of Chlb 606 are 15,630 – 15,710 cm⁻¹ and of Chlb 607 are 15,680 – 15,760 cm⁻¹. The site-energy of Chlb 606 is potentially red-shifted because its formyl group hydrogen bonds with water, as opposed to with the amide group from Gln as is the case for Chlb 607²¹. However, competing molecular factors preclude facile determination of site energy shifts from the molecular structure as multiple interactions are likely to have similar magnitudes⁶. The values found here may provide a benchmark for results of sophisticated computational models. Chlbs 606 and 607 site energies result in excitonic states in the high energy region of the Q_y band, thereby contributing to spectral coverage and serving as initial sites in an energy transfer chain to the low energy exit site. They neighbor Chlb 605, red shifted by its site energy, which serves to sequester the excitation from back transfer and also moves the excitation closer in energy to the Chla band (and exit site).

While the relaxation step discussed above successfully characterized the site-basis transition energies of Chlbs 606 and 607 by exploiting the polarization-induced isolation of a cross-peak, the same polarization dependence can potentially dissect and describe a more congested region of the spectrum. The mid-energy Chla to low energy Chla cross-peak (shown in Fig. 3.1a), despite interference from overlapping cross-peaks and the edges of diagonal peaks, shows an increase in relative intensity neither seen in other near-diagonal peaks nor in peaks from energy transfer into the same band of acceptor states. We therefore assume sufficient isolation for an analysis of the angle between etdms.

According to the working model,⁸ at 60 fs the cross-peak mostly contains contributions from relaxation between the two excitons delocalized over the dimer formed by Chlas 602 and 603. With increasing waiting time, the enhanced relative intensity of this peak diminishes from contributions by slower relaxation steps within the same spectral region. The relative enhancement again indicates a donor-acceptor projection angle of ~90°. In this case, two additional constraints exist. Because transitions within 60 fs require a large mixing angle, meaning a large relative magnitude of electronic coupling to site energy gap, the site energy gap must be small²⁸. Second, the site-basis transition energies must produce a cross-peak at the energetic coordinates measured (ω_{τ} =14,900 cm⁻¹; ω_{ν} =14,775 cm⁻¹), disallowing high or very low frequency site energies. The angle between the etdms of the two excitons delocalized over the Chla 602/603 dimer is plotted versus site-basis transition energies of the two uncoupled

chlorophylls in Fig. 5b. The criteria required by experimental results are that site energies produce an angle close to 90° between etdms, energetic coordinates give rise to the cross-peak observed, and mostly $\sim 90^\circ$ values within a Gaussian distribution around the site energies as in the previous case. The region that matches these restrictions is $15,040 - 15,080 \text{ cm}^{-1}$ for Chla 602 and $15,080 - 15,110 \text{ cm}^{-1}$ for Chla 603 (highlighted by an off-white box in Fig. 3.5b). These values, which position the site energies of Chlas 602 and 603 in the red half of the Chla band, are potentially from the polar environment around Chla 602 (it is coordinated by a Glu that forms an ion bridge with an Arg)²², the alignment, and resultant van der Waals contact, between the π systems of Chla 603 and one of the luteins²², and the coordination of Chla 603 by a His, which introduces a red-shift with its aromatic ring²¹. The excitons localized on these chromophores, because of red-shifted site energies, are within kT at room temperature of the low energy excitons on the exit site. As a result, energy can transfer back and forth between the exit site and these states *in vivo*. The location of Chlas 602 and 603 on the inner side within trimeric LHCII could allow for transfer between LHCII monomers as linkers in a potential pathway to exit trimeric LHCII via energy transfer across a different monomer of the trimer.

Employing a range of site energies can also play a role in determining etdm directions that maximize the efficacy of light-harvesting. In order to collect incident light, LHCII must absorb photons that impinge from all directions and across as many wavelengths of the solar spectrum as possible. LHCII has an essentially isotropic etdm distribution^{21,22}. Total etdm direction is a conserved quantity, and so is dictated by the directions of the etdms. Due to coupling across spectral regions, however, the direction of the etdms in each energy range is not conserved. The site-basis transition energies play an important role in determining etdm direction and could aid in producing an isotropic distribution within each spectral region. Table 3.1 illustrates this point for the Chla band. The collective oscillator strength for excitons 1-4 (the lower energy half of the Chla band) and for excitons 5-8 (the upper energy half of the Chla band) are calculated in the x, y, and z directions for the case of (a) heterogeneous site energies (taken from the working Hamiltonian) and (b) homogeneous site energies (taken to be $15,165 \text{ cm}^{-1}$, the median of the Chla band), where variation in exciton energy arises solely from splitting due to coupling. For each Cartesian component, the standard deviation of the total transition dipole strength in both halves of the Chla band is calculated. The average value of the standard deviation in x, y, and z is 0.33 for the heterogeneous case and 0.84 for the homogeneous case. Therefore, oscillator strength in each direction is more evenly distributed across wavelength as a result of the variation in site energies. Within this model, the site energies serve to optimize both excited state energies (by increased spectral coverage) and directions (by isotropic transition dipole strength at each energy).

3.5 Conclusion.

We have shown the use of polarization sequences in 2D spectroscopy separates obscured peaks and provides an incisive new tool to experimentally refine site-basis transition energies. We demonstrate the utility of these techniques on LHCII, the most important light-harvester in green plants. LHCII contains a large number of pigments with overlapping transitions, and so requires the additional information from polarized

2D spectroscopy to disentangle its dynamics and electronic structure. The cross-peak specific polarization sequence enhances buried peaks in crowded off-diagonal regions, and this enhancement measures relative directions of etdms of coupled transitions. Once related to individual pigments, the angle between etdms can experimentally access site-basis transition energies. Knowledge of site energies, tuned by the protein environment surrounding each chromophore, are required to map how individual pigments contribute to the excitonic structure, and how the excitonic structure produces efficient energy flow. Overall, variation in these values for the chlorophyll within a PPC both increases spectral coverage to absorb across more of the solar spectrum using a single type of light-harvesting molecule and also tunes the direction of etdms at all resonant energies to absorb across a more isotropic distribution of incident light polarization, which aids photosynthetic organisms in utilizing incoherent sunlight. In future experiments, polarization sequences could iteratively maximize each cross-peak to determine dynamics of an energy transfer step and the angle between donor and acceptor etdms. Through energy transfer steps in which each chromophore is involved, the site energy of each uncoupled pigment could be found. Additionally, this approach, in which decongestion enables access to molecular information, could be extended to extricate peaks from within spectra of even larger, more complex systems such as PSI or the PSII supercomplex.

3.6 Experimental Methods.

Trimeric LHCII isolated from *Arabidopsis thaliana* as described previously²⁹ was dissolved in 50 mM HEPES buffer (pH 7.6) with *n*-dodecyl α -D-maltoside 0.03%, mixed with glycerol at 30:70 (v/v), placed in a 200 μ m quartz cell and cooled to 77 K. An OD of 0.13 was measured at 670 nm.

Details of the experiment have been described in detail elsewhere³⁰. In brief, a home-built amplified Ti:Sa laser system pumped a home-built NOPA to produce 80 nm bandwidth pulses centered at 650 nm and compressed to a duration of 22 fs⁸. Four beams (three beams with 6 nJ per pulse and a local oscillator attenuated by four orders of magnitude) were focused to a spot size of 100 μ m.

The 2D apparatus is a diffractive optic based design in which four beams in a box geometry are generated by a beam-splitter, followed by a transmissive grating optimized for the ± 1 orders^{30,31}. Each spectrum is constructed by scanning the delay between pulses 1 and 2, known as the coherence time (τ), by the movement of paired glass wedges. The waiting time, or the period over which the monitored dynamics occur, is the delay between pulses 2 and 3 and is set by a retroreflector delay stage. The signal emitted in the phase-matched direction, $\mathbf{k}_s = -\mathbf{k}_1 + \mathbf{k}_2 + \mathbf{k}_3$, collinear with the local oscillator, is heterodyne-detected using a spectrometer and charge coupled device camera to form the emission axis. Achromatic, $\frac{1}{2}$ -wave retarders inserted into beams 1, 2 and 3 control the linear polarization¹⁰. The coherence time was scanned from -566.5 fs to 566.5 fs for the all-parallel data, (0,0,0,0), and from -451 fs to 451 fs for the cross-peak specific data, ($\pi/3, -\pi/3, 0, 0$), where negative time points denote the arrival of pulse 2 before pulse 1, which are the non-rephasing spectra²³. For each waiting time, a Fourier transform over the coherence time axis generates the excitation axis.

3.7 References

- (1) Blankenship, R. E., *Molecular mechanisms of photosynthesis*. Blackwell Science: Oxford ; Malden, MA, 2002; p 321 p.
- (2) Muller, P.; Li, X. P.; Niyogi, K. K., Non-photochemical quenching. A response to excess light energy. *Plant Physiology* **2001**, *125* (4), 1558-1566.
- (3) Nield, J.; Barber, J., Refinement of the structural model for the Photosystem II supercomplex of higher plants. *Biochimica Et Biophysica Acta-Bioenergetics* **2006**, *1757* (5-6), 353-361.
- (4) Zigmantas, D.; Read, E. L.; Mancal, T.; Brixner, T.; Gardiner, A. T.; Cogdell, R. J.; Fleming, G. R., Two-dimensional electronic spectroscopy of the B800-B820 light-harvesting complex. *Proceedings of the National Academy of Sciences of the United States of America* **2006**, *103* (34), 12672-12677.
- (5) Ishizaki, A.; Fleming, G. R., Theoretical examination of quantum coherence in a photosynthetic system at physiological temperature. *Proceedings of the National Academy of Sciences of the United States of America* **2009**, *106* (41), 17255-17260.
- (6) Adolphs, J.; Muh, F.; Madjet, M. E. A.; Renger, T., Calculation of pigment transition energies in the FMO protein. *Photosynthesis Research* **2008**, *95* (2-3), 197-209.
- (7) Novoderezhkin, V. I.; Palacios, M. A.; van Amerongen, H.; van Grondelle, R., Excitation dynamics in the LHCII complex of higher plants: Modeling based on the 2.72 angstrom crystal structure. *Journal of Physical Chemistry B* **2005**, *109* (20), 10493-10504.
- (8) Schlau-Cohen, G. S.; Calhoun, T. R.; Ginsberg, N. S.; Read, E. L.; Ballottari, M.; Bassi, R.; van Grondelle, R.; Fleming, G. R., Pathways of Energy Flow in LHCII from Two-Dimensional Electronic Spectroscopy. *Journal of Physical Chemistry B* **2009**, *113* (46), 15352-15363.
- (9) Brixner, T.; Stenger, J.; Vaswani, H. M.; Cho, M.; Blankenship, R. E.; Fleming, G. R., Two-dimensional spectroscopy of electronic couplings in photosynthesis. *Nature* **2005**, *434* (7033), 625-8.
- (10) Read, E. L.; Engel, G. S.; Calhoun, T. R.; Mancal, T.; Ahn, T. K.; Blankenship, R. E.; Fleming, G. R., Cross-peak-specific two-dimensional electronic spectroscopy. *Proceedings of the National Academy of Sciences of the United States of America* **2007**, *104* (36), 14203-14208.
- (11) van Grondelle, R.; Novoderezhkin, V. I., Energy transfer in photosynthesis: experimental insights and quantitative models. *Physical Chemistry Chemical Physics* **2006**, *8* (7), 793-807.
- (12) Remelli, R.; Varotto, C.; Sandona, D.; Croce, R.; Bassi, R., Chlorophyll binding to monomeric light-harvesting complex - A mutation analysis of chromophore-binding residues. *Journal of Biological Chemistry* **1999**, *274* (47), 33510-33521.
- (13) Rogl, H.; Schodel, R.; Lokstein, H.; Kuhlbrandt, W.; Schubert, A., Assignment of spectral substructures to pigment-binding sites in higher plant light-harvesting complex LHC-II. *Biochemistry* **2002**, *41* (7), 2281-2287.
- (14) Georgakopoulou, S.; van der Zwan, G.; Bassi, R.; van Grondelle, R.; van Amerongen, H.; Croce, R., Understanding the changes in the circular dichroism of light

harvesting complex II upon varying its pigment composition and organization. *Biochemistry* **2007**, *46* (16), 4745-4754.

(15) van Amerongen, H.; Valkunas, L.; van Grondelle, R., *Photosynthetic excitons*. World Scientific: Singapore ; River Edge, N.J., 2000; Vol. Ch. 8. Exciton Dynamics, p xiv, 590 p.

(16) Jonas, D. M., Two-dimensional femtosecond spectroscopy. *Annual Review of Physical Chemistry* **2003**, *54*, 425-463.

(17) Ginsberg, N. S.; Cheng, Y. C.; Fleming, G. R., Two-Dimensional Electronic Spectroscopy of Molecular Aggregates. *Accounts of Chemical Research* **2009**, *42* (9), 1352-1363.

(18) Hochstrasser, R. M., Two-dimensional IR-spectroscopy: polarization anisotropy effects. *Chemical Physics* **2001**, *266* (2-3), 273-284.

(19) Dreyer, J.; Moran, A. M.; Mukamel, S., Tensor components in three pulse vibrational echoes of a rigid dipeptide. *Bulletin of the Korean Chemical Society* **2003**, *24* (8), 1091-1096.

(20) Read, E. L.; Schlau-Cohen, G. S.; Engel, G. S.; Wen, J. Z.; Blankenship, R. E.; Fleming, G. R., Visualization of excitonic structure in the Fenna-Matthews-Olson photosynthetic complex by polarization-dependent two-dimensional electronic spectroscopy. *Biophysical Journal* **2008**, *95* (2), 847-856.

(21) Liu, Z. F.; Yan, H. C.; Wang, K. B.; Kuang, T. Y.; Zhang, J. P.; Gui, L. L.; An, X. M.; Chang, W. R., Crystal structure of spinach major light-harvesting complex at 2.72 angstrom resolution. *Nature* **2004**, *428* (6980), 287-292.

(22) Standfuss, R.; van Scheltinga, A. C. T.; Lamborghini, M.; Kuhlbrandt, W., Mechanisms of photoprotection and nonphotochemical quenching in pea light-harvesting complex at 2.5Å resolution. *Embo Journal* **2005**, *24* (5), 919-928.

(23) Ernst, R. R., Bodenhausen, Geoffrey, Wokaun, Alexander, *Principles of Nuclear Magnetic Resonance in One and Two Dimensions*. Oxford Science Publications: Oxford, 1987.

(24) Zanni, M. T.; Ge, N. H.; Kim, Y. S.; Hochstrasser, R. M., Two-dimensional IR spectroscopy can be designed to eliminate the diagonal peaks and expose only the crosspeaks needed for structure determination. *Proceedings of the National Academy of Sciences of the United States of America* **2001**, *98* (20), 11265-11270.

(25) Mukamel, S., *Principles of nonlinear optical spectroscopy*. Oxford University Press: New York ; Oxford, 1995; p xviii, 543 p.

(26) Calhoun, T. R.; Ginsberg, N. S.; Schlau-Cohen, G. S.; Cheng, Y. C.; Ballottari, M.; Bassi, R.; Fleming, G. R., Quantum Coherence Enabled Determination of the Energy Landscape in Light-Harvesting Complex II. *Journal of Physical Chemistry B* **2009**, *113* (51), 16291-16295.

(27) Frahmcke, J. S.; Walla, P. J., Coulombic couplings between pigments in the major light-harvesting complex LHC II calculated by the transition density cube method. *Chemical Physics Letters* **2006**, *430* (4-6), 397-403.

(28) Ishizaki, A.; Fleming, G. R., Unified treatment of quantum coherent and incoherent hopping dynamics in electronic energy transfer: Reduced hierarchy equation approach. *Journal of Chemical Physics* **2009**, *130* (23), -.

(29) Caffarri, S.; Croce, R.; Breton, J.; Bassi, R., The major antenna complex of photosystem II has a xanthophyll binding site not involved in light harvesting. *Journal of Biological Chemistry* **2001**, *276* (38), 35924-35933.

(30) Brixner, T.; Mancal, T.; Stiopkin, I. V.; Fleming, G. R., Phase-stabilized two-dimensional electronic spectroscopy. *Journal of Chemical Physics* **2004**, *121* (9), 4221-4236.

(31) Cowan, M. L.; Ogilvie, J. P.; Miller, R. J. D., Two-dimensional spectroscopy using diffractive optics based phased-locked photon echoes. *Chemical Physics Letters* **2004**, *386* (1-3), 184-189.

Table 3.1: Etdm directional distribution across energy from site energy heterogeneity

Direction	Excitons 1-4 (heterogeneous)	Excitons 5-8 (heterogeneous)	$\sigma_{\text{heterogeneous}}$	Excitons 1-4 (homogeneous)	Excitons 5-8 (homogeneous)	$\sigma_{\text{homogeneous}}$
X	2.9	2.3	0.40	3.3	1.8	1.03
Y	1.4	1.4	0.019	1.6	1.7	0.093
Z	1.9	1.1	0.55	2.6	0.6	1.40

Table 3.1. Total dipole moment in each Cartesian direction for Chla band excitons split into lower and higher energy halves using site energies in the model and using homogeneous site energies of $15,165 \text{ cm}^{-1}$, which produce an average standard deviation of 0.33 and 0.84 between the two halves, respectively.

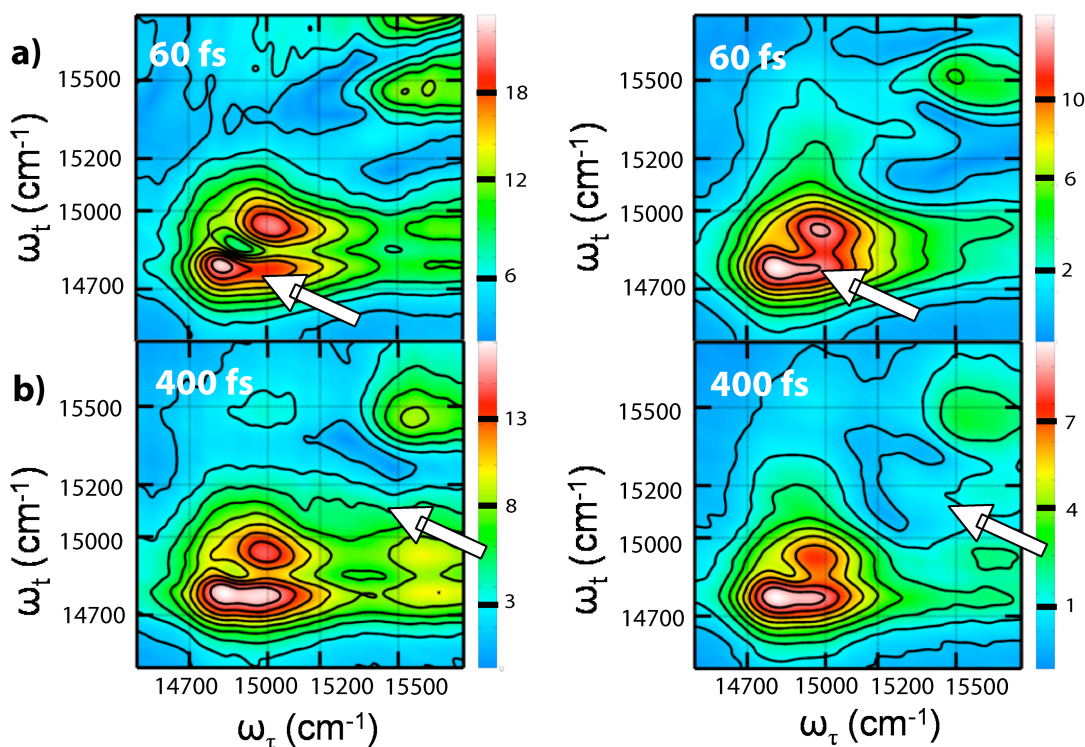


Figure 3.1. Absolute value, non-rephasing 2D spectra under all-parallel polarization sequence (left) and cross-peak specific polarization sequence (right) for $T=60$ and 400 fs . Arrows indicate regions with the most variation under the two polarization sequences.

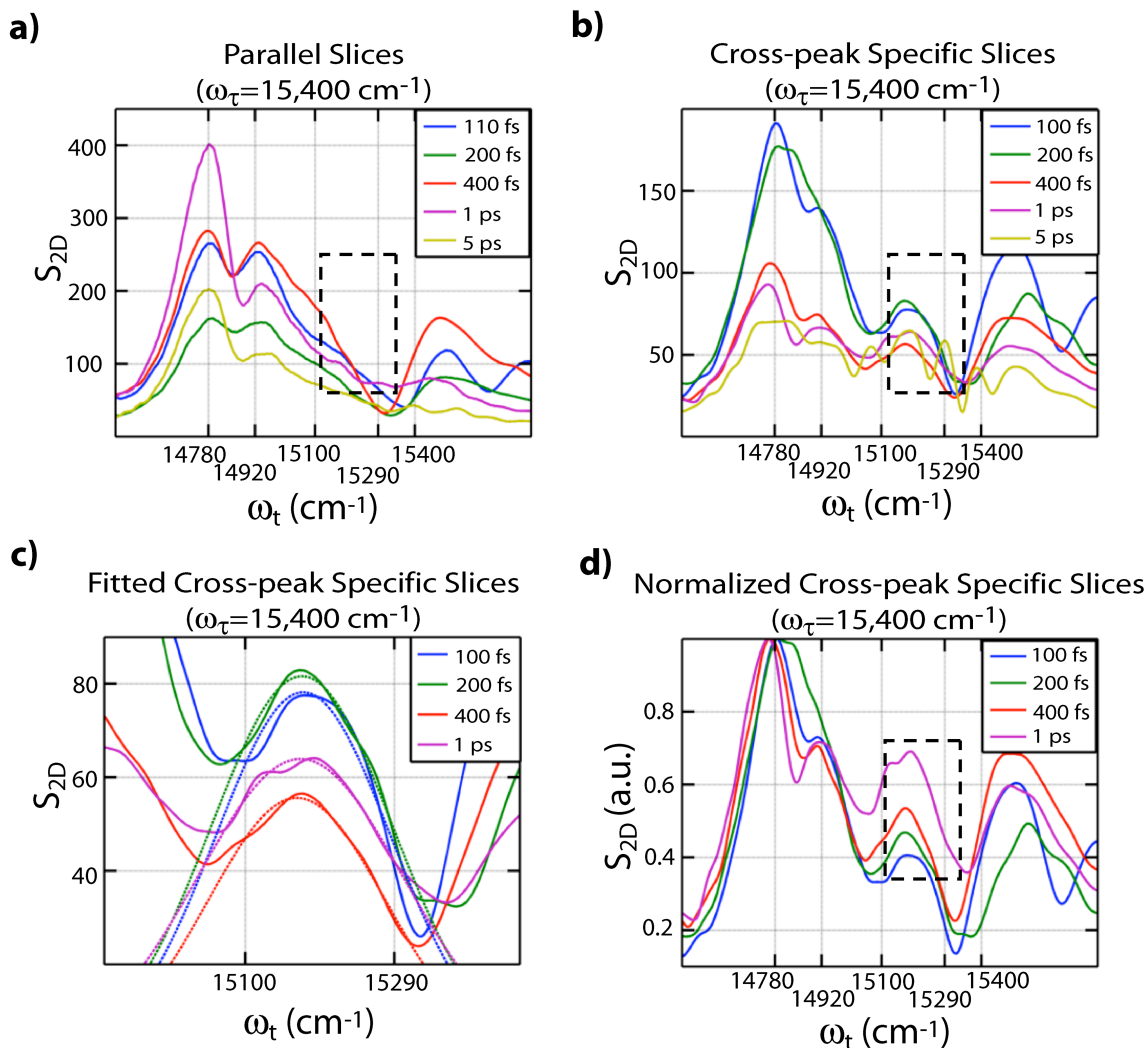


Figure 3.2. Vertical slices from the non-rephasing, absolute value 2D spectra (S_{2D}) along an excitation energy of $\omega_\tau = 15,400 \text{ cm}^{-1}$: a) under all-parallel polarization with a box highlighting the region of the buried cross-peak; b) under cross-peak specific polarization with a box highlighting the revealed cross-peak; c) zoomed in on the boxed region under cross-peak specific polarization with fits of the slices plotted; d) normalized under cross-peak specific polarization.

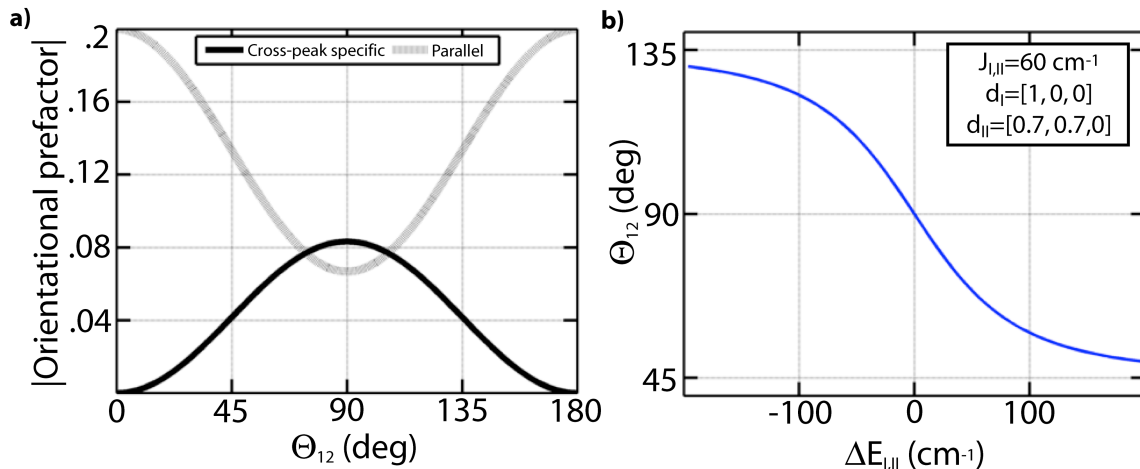


Figure 3.3. a) Absolute value of the orientational prefactor for pathways of population transfer (cross-peaks) in the non-rephasing spectra under cross-peak specific and all-parallel polarizations as a function of angle between donor and acceptor etdms; b) angle between etdms as a function of site energy gap for a dimer system with stdm directions d_I and d_{II} and coupling $J_{I,II}$.

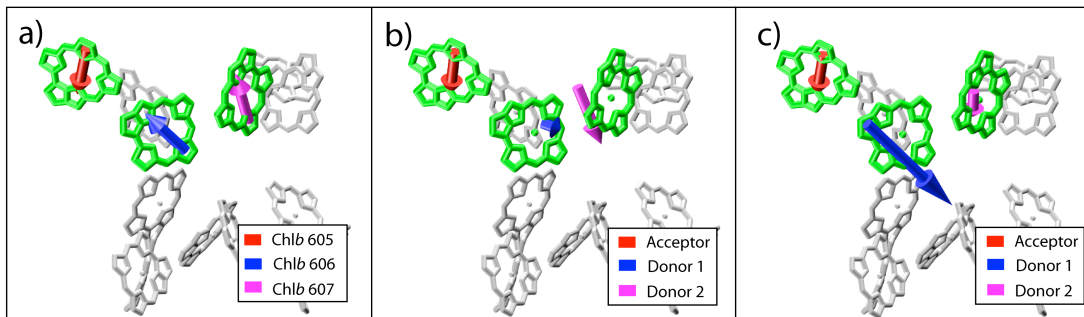


Figure 3.4. Transition dipole moments localized on Chl 605, 606 and 607 in an LHCII monomer for a) site-basis transition dipole moments ($J_{\text{Chl}606-607}=0$); b) excitonic transition dipole moments with site energy estimates of $E_{\text{Chl}606}=15,680 \text{ cm}^{-1}$, $E_{\text{Chl}607}=15,730 \text{ cm}^{-1}$, $J_{\text{Chl}606-607}=23.7 \text{ cm}^{-1}$; c) excitonic transition dipole moments with site energies $E_{\text{Chl}606}=15,780 \text{ cm}^{-1}$, $E_{\text{Chl}607}=15,700 \text{ cm}^{-1}$, $J_{\text{Chl}606-607}=23.7 \text{ cm}^{-1}$.

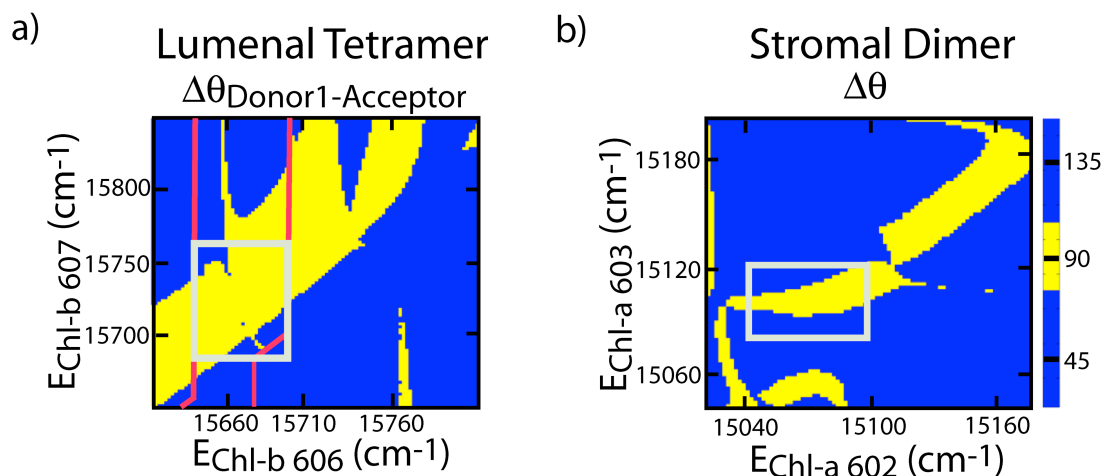


Figure 3.5. Plots of the angle between etdms as a function of site energies of two chromophores coupled to each other for: a) angle between etdms of donor 1 (localized mostly on Chl*b* 606) and the acceptor (localized on a third chromophore, Chl*b* 605) as a function of the site energies of the two Chl*b*s which give rise to the donor excitons. Bounds from site-directed mutagenesis are shown in pink. The off-white box indicates the range of site energies for Chl*b*s 606 and 607 that matches experimental results; b) angle between etdms of the two states delocalized across the Chl*a* 602/603 dimer as a function of site energies of two coupled chromophores, Chl*a*s 602 and 603. The off-white box indicates the range of site energies for Chl*a*s 602 and 603 imposed by experimental results.

Chapter 4

Direct Imaging of Quantum Coherence in LHCI

4.1 Abstract

Photosynthetic organisms harvest sunlight with near unity quantum efficiency. The initial absorption and energy transfer steps occur on networks of pigment-protein complexes (PPCs) made up of strongly interacting chromophores. The complexity of the electronic structure and energy transfer pathways within the PPCs obscures the mechanisms behind the efficiency of the light absorption to charge separation process. Recent experiments have detected long-lived quantum coherence, and theoretical models suggest that this phenomenon may contribute to the efficiency of photosynthetic energy transfer. In particular, multidimensional spectroscopy has been used to investigate quantum coherence. In order to better elucidate the role of coherent dynamics from within congested photosynthetic spectra, we present a polarization sequence of the incident laser pulses, called a coherence-specific polarization sequence, which isolates the spectral contributions of excitonic quantum coherence from the stronger signals corresponding to linear absorption that also appear. We apply this polarization sequence for the first time in the electronic regime and determine the overall measurable lifetime of excitonic coherence in the major light-harvesting complex of Photosystem II.

4.2 Introduction

Photosynthetic plants and bacteria fuel most life on earth by absorbing sunlight and converting it to chemical energy with near unity quantum efficiency¹. Complicated networks of densely packed pigment protein complexes (PPCs) absorb and then translocate the photoenergy to a central site of charge separation, known as the reaction center.² The relatively low intensity of sunlight at the Earth's surface (1000 W/m^2), drives a dense packing of pigments within the PPCs, which produces electrodynamic coupling between pigments that are highly sensitive to the molecular structure. The strength of these couplings means they determine the pathways and mechanisms by which energy transports from initial absorption site to the reaction center. Furthermore, these strong couplings drive the existence of quantum-coherent electronic excitations between multiple pigments, even at physiological temperatures. We present a new extension of 2D spectroscopy, the application of a coherence-specific polarization sequence, which directly probes coherence, and offers the potential to isolate coherence related phenomena, such as coherence transfer.

Emerging experimental and theoretical results have revealed that electronic excitations move through photosynthetic complexes as quantum mechanical wavepackets that maintain their phase coherence,^{3,4} or exhibit long-lasting oscillatory motion between multiple chromophores. This effect, quantum coherence, is a coherent superposition of delocalized excited states, which theoretical results have suggested could be one potential contributor to the remarkable efficacy of photosynthetic light-harvesting. While long-standing experiments have observed indications of quantum coherence, definitive

detection of quantum coherence within the complex dynamics of photosynthetic dynamics was not possible. Only recently have two-dimensional (2D) and non-degenerate photon echo experiments begun to provide methods to clearly access signals from quantum coherence⁵. Four wave mixing experiments have detected long-lived quantum beating in PPCs from bacterial, algal and plant systems at ambient and cryogenic temperatures.⁶⁻⁹ The signals from coherence are detectable beyond the femtosecond timescale of much of photosynthetic energy transfer⁸. The coincidence of timescales has fueled discussion that coherence may play a role in ensuring the efficiency of energy transfer^{10, 11}. One component of understanding the role of quantum coherence is quantifying the correlation between the long-lived quantum beating and energy transfer. Specifically, this requires elucidating the energies of the excitonic states exhibiting strong quantum beating as compared to the energies of the donor and acceptor and the timescales of the quantum beating signals, and identifying the energy transfer timescales between these pairs of excited states. Correlating the lifetime of the beating and the rate of energy transfer may allow for a better understanding of their interplay.

In the case of all-parallel 2D spectroscopy, probing oscillatory behavior requires recording a large number of time delays in order to sample at enough time intervals to create an additional frequency axis to visualize beating. The oscillation, however, appears on top of a background of signals corresponding to linear absorption¹². Here, we present a coherence-specific pulse sequence, applied for the first time to electronic transitions, which isolates the signal from quantum beating without requiring the collection of many timepoints¹³. In this pulse sequence ($\pi/4$, $-\pi/4$, $\pi/2$, 0), the two excitation beams are orthogonal to each other, as are the two emission beams. This selects for pathways where the two beams excite in the ensemble non-parallel transition dipole, or a coherence, and only stimulate emitted signals from a coherence, as beam 3 and the detection polarization (local oscillator polarization) are non-parallel as well.

In 2D spectroscopy, a broadband femtosecond pulse, encompassing multiple transitions, excites the sample and then monitors its evolution by spectrally resolving both absorption and emission with a variable delay (the time period over which oscillatory motion from quantum coherence is observed) between absorption and emission¹⁴. 2D spectra are plotted as a function of absorption and emission frequency for each delay time and contain the sum of all phase and energy conserving processes within the system, including signals corresponding to linear absorption, energy transfer, coupling, and coherence^{14, 15}. A 2D measurement requires interaction with four laser pulses. Careful manipulation of their polarization has been shown to be able to extricate information about molecular processes from more intense, overlapping peaks, which often obscure the desired signal^{16, 17}. In this case, by varying the polarization of the incident beams, we generate coherence-specific spectra to examine the energies and timescales of states giving rise to quantum coherence free from a background of linear absorption, population transfer, coupling and excited state absorption signals. The ability to observe the separated quantum beating signal allows a clearer understanding of which excited states contribute to coherent motion and therefore how excitonic coherence coincides with, and thus potentially contributes to, energy transfer.

In understanding photosynthesis, light-harvesting complex II (LHCII) from green plants is the most important complex to examine because it contains more than 50% of the world's chlorophyll.¹⁸ In a recent all-parallel 2D experiment on LHCII, the existence

of coherence was demonstrated and observed to persist through the 500 fs timescale of the experiment, which is notable because multiple energy transfer processes have been detected to occur within LHCII in less than 500 fs.^{9, 19} While all-parallel 2D experiments determined the existence of a long-lived beating signal^{3, 20}, the long collection times precluded examination of quantum coherence through the decay of the signal. Here, we apply the coherence-specific polarization scheme to LHCII. Under the coherence-specific polarization, a non-zero signal at a single waiting time indicates the presence of coherence. Because these peaks arise at the energies of the excited states exhibiting coherence, it provides a means to better understand the contribution of individual excited states to quantum coherence, the lifetime of coherence within each spectral region and the overall measurable lifetime of this phenomenon in LHCII. This additionally allows for examination over a larger range of waiting times, useful for analyses such as determining the lifetime of this phenomenon.

4.3 Experimental Methods

Trimeric LHCII was isolated from *Arabidopsis thaliana* as described previously²¹. LHCII was dissolved in 50 mM HEPES buffer (pH 7.6) with *n*-dodecyl α -D-maltoside 0.03%, mixed with glycerol at 30:70 (v/v), placed in a 200 μ m quartz cell and cooled to 77 K. An OD of 0.13 for the sample was measured at 670 nm (per 200 μ m). The details of the experimental apparatus, data acquisition, and analysis have been described in detail elsewhere.^{22, 23} In brief, a home-built Ti:sapphire oscillator seeded a home-built Ti:sapphire regenerative amplifier which pumped a home-built NOPA to produce a 3.4 kHz pulse train of 80 nm bandwidth pulses centered at 650 nm and compressed to a duration of 22 fs^{19, 24}. During the experiment, the four beams (three beams with 6 nJ per pulse and a local oscillator attenuated by four orders of magnitude) were focused to a spot size of 100 μ m.

The 2D apparatus is a diffractive optic based design in which four beams in a box geometry are generated by a beam-splitter, followed by a transmissive grating optimized for the ± 1 orders^{22, 25}. Each spectrum is constructed by scanning the delay between pulses 1 and 2, known as the coherence time (τ), by the movement of paired glass wedges. The waiting time (T), or the period over which the monitored dynamics occur, is the delay between pulses 2 and 3 and is set by a retroreflector delay stage. The signal emitted in the phase-matched direction, $\mathbf{k}_s = -\mathbf{k}_1 + \mathbf{k}_2 + \mathbf{k}_3$, collinear with the local oscillator, is heterodyne-detected using a spectrometer and charge coupled device camera to form the emission axis (ω_t). Achromatic, $\frac{1}{2}$ -wave retarders inserted into beams 1, 2 and 3 control the linear polarization¹⁶. The coherence time was scanned from -566.5 fs to 566.5 fs for the all-parallel data, (0,0,0,0), and from -319 fs to 319 fs for the coherence-peak specific data, ($\pi/4, -\pi/4, \pi/2, 0$) where negative time points denote the arrival of pulse 2 before pulse 1, which are the non-rephasing spectra²⁶. For each waiting time, a Fourier transform over the coherence time axis generates the excitation axis (ω).

4.4 Results & Discussion

Trimeric LHCII is comprised of three monomers, each with fourteen chlorophyll and four carotenoids, held in a close-packed arrangement by a surrounding protein

matrix. The structural model from x-ray crystallography is shown in Fig. 4.1. The fourteen chlorophyll are found in two spectral and structural variants (8 Chla and 6 Chlb). In Figure 4.2a-d, the absolute value, non-rephasing 2D spectra under the coherence-specific polarization sequence are shown. The spectra can be considered as containing three regions: 1) Chla ($<14,900 \text{ cm}^{-1}$); 2) intermediate, with high energy Chla and low energy Chlb ($14,900 \text{ cm}^{-1} < 15,200 \text{ cm}^{-1}$); and 3) Chlb ($>15,200 \text{ cm}^{-1}$). The spectra are characterized by three clear diagonal peaks, all of which are visible in the $T=0$ fs spectrum: two peaks in the Chla region and one peak in the Chlb region. The signals due to coherence can be separated into on-diagonal and off-diagonal contributions, which appear in non-rephasing and rephasing spectra respectively²⁷. The coordinates of the off-diagonal peaks, which appear in the rephasing spectra, connect the two excitons that give rise to the superposition state. Within the non-rephasing spectra, those shown in Fig. 4.2, the diagonal features directly correspond to each exciton involved in quantum coherence and so provide a direct measure, weighted by the orientational factor and dipole strength of these transitions, of the amount of excitonic coherence in which each states is involved. Additionally, the anti-diagonal elongation of non-rephasing features facilitates identification of absorption and emission energies.

Within the spectra shown in Fig. 4.2, all Liouville pathways (all momentum and energy conserving molecular processes) that do not arise from coherence during the waiting time are suppressed^{13,28} due to the pulse polarizations, $(\pi/4, -\pi/4, \pi/2, 0)$. Each peak within a 2D spectrum is scaled by an orientational prefactor based on the angle between the incident pulses and the angles between the transition dipole moments of the states involved in the molecular process that produces the peak for an isotropic sample. The orientational prefactor has the following mathematical form²⁸⁻³⁰,

$$\begin{aligned} \langle i_{\alpha} j_{\beta} k_{\gamma} l_{\delta} \rangle = & \frac{1}{30} [\langle \cos \theta_{\alpha\beta} \cos \theta_{\gamma\delta} \rangle (4 \cos \theta_{ij} \cos \theta_{kl} - \cos \theta_{ik} \cos \theta_{jl} - \cos \theta_{il} \cos \theta_{jk}) \\ & + \langle \cos \theta_{\alpha\gamma} \cos \theta_{\beta\delta} \rangle (4 \cos \theta_{ik} \cos \theta_{jl} - \cos \theta_{ij} \cos \theta_{kl} - \cos \theta_{il} \cos \theta_{jk}) \\ & + \langle \cos \theta_{\alpha\beta} \cos \theta_{\gamma\delta} \rangle (4 \cos \theta_{il} \cos \theta_{jk} - \cos \theta_{ij} \cos \theta_{kl} - \cos \theta_{ik} \cos \theta_{jl})] \end{aligned} \quad (1)$$

where $i, j, k,$ and l are the laser polarizations in the lab frame and $\alpha, \beta, \gamma,$ and δ are the excited state transition dipole moments in the molecular frame. In the experiment presented here, the angles of the laser pulses were chosen so that this prefactor is non-zero only for Liouville pathways where the system is in a coherence during the waiting time. That is, signals from molecular processes corresponding to linear absorption, coupling, population transfer, and excited state absorption are suppressed.

The diagonal features that appear throughout the spectrum indicate the existence of coherence in all resonant regions. These results are consistent with the long-lived oscillatory behavior observed in all-parallel 2D experiments on LHCII⁹. Due to the removal of the background of signals from linear absorption, however, here the relative intensities of features in different spectral regions can be more easily observed. Especially at $T>0$, the mid-energy Chl-a region shows a particularly strong coherence signature, with more intensity in the peak than would be expected from theoretical predictions for this spectral region.²⁰ Changes in relative amplitude of the peaks indicate differences between the lifetimes of coherences in different spectral regions. Fluctuations induced by the surrounding protein environment are responsible for destruction of the phase coherence that maintains quantum mechanical wavepackets. Because of

differences in the protein environments surrounding each pigment, the timescale over which phase coherence is destroyed changes with the site-basis composition of the excitonic states involved in each beating signal. Experimental and theoretical results show that an individual alpha helix, large enough to surround multiple pigments, could correlate the multiple transition energies of multiple pigments and thus maintain coherence for longer than initially expected⁶. In a model where the excitonic states in the mid-energy Chl-a region are related to specific chromophores, the long lifetime of coherence in this region could serve as a guide for the model of the protein environment around the pigments.

The coherence-specific 2D spectra show the total amount of excitonic coherence in the entire LHCII complex. Therefore, in order to examine the total evolution of excitonic coherence, the coherence-specific spectra are integrated and the integrated intensity is plotted versus waiting time in Figure 4.3. The overall lifetime of coherences produced by non-negligible coupling in LHCII was found through fitting this curve. The results of fitting the data to a three-lifetime exponential are presented in Table 4.1. The short time and overall signal decay timescales (the shortest and longest lifetime components) were determined through a similar analysis of all-parallel data on LHCII taken on the same apparatus,¹⁹ because these values should be consistent for both sets of data. The all-parallel data was fit to a bi-exponential decay where the two timescales are from the combination of short time decays (the physical origin of which is discussed below) and the overall signal decay. The intermediate decay time was found using the coherence data, and this lifetime indicates an overall decoherence time of 700-900 fs (the range is due to the limited resolution from the large timestep of the data). Recent theoretical work has shown that the timescales of coherent motion in individual PPCs far outlasts that in the ensemble, which is the measured value. The observation of ensemble averaged behavior does, however, offer insight into the physical phenomena behind photosynthetic light-harvesting.

A broadband femtosecond pulse initially excites coherent superpositions between many different combinations of the excitons in LHCII, as recently demonstrated experimentally using 2D spectroscopy⁹. A Fourier transform of oscillatory time domain data produced peaks at the energy differences between the excitonic states, or the beat frequency at which a superposition would oscillate. Because the Fourier transform of even a short-lived oscillation produces a frequency domain peak, the number of peaks displayed the large number of coherences at short times. These coherences can be considered in two separate categories. In the first category, which contains most of these excitonic superpositions, these coherences arise as a function of excitation by a femtosecond pulse. The resultant oscillations decay rapidly because of the vanishingly small couplings between many of the pigments, compared to the strength of the interaction with the surrounding protein environment. In the second category, however, the electronic coupling (between the site basis chromophores which give rise to the excitonic states involved in the coherence) is on the same order or larger than the coupling to the surrounding protein environment. These coherences will persist through the timescale of energy transfer, pointing to the existence of wavelike motion of the excitation through the pigments. Simulations illustrating the range of lifetimes of excitonic coherences within LHCII are shown in Fig. 4.4. Figure 4.4 shows the population of excitonic coherences for a given pair of chromophores as a function of

waiting time. These dynamics were modeled using the method developed by Ishizaki and Fleming³¹. Figure 4a shows the simulated decay of coherence between two excitons produced by the strongest coupling with LHCII, $J=105 \text{ cm}^{-1}$.³² The coherence exhibits a lifetime of 700 fs. Figure 4b, however, shows a simulation of the coherence decay between two excitons where the site-basis contributions to these states (Chl-a 604 and Chl-b 605) have a vanishingly small coupling ($J_{604,605}=5.4 \text{ cm}^{-1}$). The short time decay was fit in the all-parallel spectra, because this effect, although due to excitonic coherence, appears at short times under both sequences and would be expected to have a large contribution at short times due to the size of the system. That is, the large amplitude of this component results from the large number of excitonic superpositions. After the first two interactions, looking at an isolated monomer, there are 182 (14×13) potential combinations of excitonic states that produce coherences during the waiting time, or $\rho(t=0)=|e_i\rangle\langle e_j|$, $i \neq j$, where ρ is the density matrix and $|e_i\rangle$ is an exciton. There are, however, only 14 possible populations, $\rho(t=0)=|e_i\rangle\langle e_i|$. From the order of magnitude difference in the number of combinations, these molecular processes combine to contribute a large amount of amplitude to the 2D spectra, which then exhibits rapid decay. Clearly, if the complete LHCII trimer is considered (containing 42 chlorophylls), there are 1,722 possible combinations, and so this effect increases drastically. Thus, the short-time decay due to rapid decay of coherences between chromophores with vanishingly small couplings is a product of large complexes with many chromophores. Additionally, the short-time component contains contributions from pulse overlap effects and the destruction of the ability of the system to rephase (produce a photon echo signal), induced by the loss of memory in the local environment. The finite timescale of this process arises from non-Markovian dynamics in the surrounding protein environment³³. Finally, an interesting potential extension of this technique could be that, with perfectly set polarizations, under this sequence off-diagonal features in the non-rephasing spectra would directly show coherence transfer. Coherence transfer is when phase coherence between two excited states then evolves into phase coherence between one of the original states and a third exciton, so essentially phase coherence is maintained through an energy transfer process. Although we do not have the precision in our polarization to be able to completely suppress all other off-diagonal features, some off-diagonal amplitude could be a signature of coherence transfer. The right shoulder of the low energy Chl-a diagonal peak broadens within 100 femtoseconds and then decays by 500 femtoseconds in agreement with dynamical and energetic expectations for coherence transfer. Coherence transfer is more likely when the energy gap remains similar through the transfer process and occurs within 100-200 femtoseconds.³³ While experiments using other polarization and pulse sequences have been shown to access the signal from coherence transfer, improving the precision of the linear polarization of the beams to the point where this technique could provide a more definitive measure of coherence transfer would provide a second means to access this elusive process.

4.5 Conclusion

We present the first demonstration of the application of the coherence-specific polarization sequence in the electronic regime. This experimental method has the potential to isolate the signal from quantum coherence from a background of other

molecular processes accessible in ultrafast experiments. A significant result of this method is the quantitative determination of the lifetime of the components of quantum coherence in LHCI produced by non-negligible couplings to be 700-900 fs in the ensemble. Application of this technique allows for elucidation of the dynamical evolution of individual excitonic superpositions. From spectra taken under all-parallel polarization sequences, the timescale of the energy transfer steps in which those excitons are involved was previously available. The additional information the coherence-specific-polarization sequence allows for identification of the second of the two important timescales, the timescale of coherences in which those excitons are involved. The overlap of these two timescales offers insight into the contribution of phase coherence to individual energy transfer steps. Relating both coherence and energy transfer to individual excitons within the molecular structure may also correlate details of the local environment to the mechanisms behind individual electronic energy transfer processes. An understanding of the role of coherence in energy transfer may point to how the large number of variables present in photosynthetic complexes combines to produce remarkably efficient energy transfer.

4.6 References

- (1) Blankenship, R. E., *Molecular mechanisms of photosynthesis*. Blackwell Science: Oxford ; Malden, MA, 2002; p 321 p.
- (2) Dekker, J. P.; Boekema, E. J., Supramolecular organization of thylakoid membrane proteins in green plants. *Biochimica Et Biophysica Acta-Bioenergetics* **2005**, *1706* (1-2), 12-39.
- (3) Engel, G. S.; Calhoun, T. R.; Read, E. L.; Ahn, T. K.; Mancal, T.; Cheng, Y. C.; Blankenship, R. E.; Fleming, G. R., Evidence for wavelike energy transfer through quantum coherence in photosynthetic systems. *Nature* **2007**, *446* (7137), 782-786.
- (4) Ishizaki, A.; Fleming, G. R., Theoretical examination of quantum coherence in a photosynthetic system at physiological temperature. *Proceedings of the National Academy of Sciences of the United States of America* **2009**, *106* (41), 17255-17260.
- (5) Cheng, Y. C.; Fleming, G. R., Coherence quantum beats in two-dimensional electronic spectroscopy. *Journal of Physical Chemistry A* **2008**, *112* (18), 4254-4260.
- (6) Lee, H.; Cheng, Y. C.; Fleming, G. R., Coherence dynamics in photosynthesis: Protein protection of excitonic coherence. *Science* **2007**, *316* (5830), 1462-1465.
- (7) Collini, E.; Wong, C. Y.; Wilk, K. E.; Curmi, P. M. G.; Brumer, P.; Scholes, G. D., Coherently wired light-harvesting in photosynthetic marine algae at ambient temperature. *Nature* **2010**, *463* (7281), 644-649.
- (8) Panitchayangkoon, G.; Hayes, D.; Fransted, K. A.; Caram, J. R.; Harel, E.; Wen, J. Z.; Blankenship, R. E.; Engel, G. S., Long-lived quantum coherence in photosynthetic complexes at physiological temperature. *Proceedings of the National Academy of Sciences of the United States of America* **2010**, *107* (29), 12766-12770.
- (9) Calhoun, T. R.; Ginsberg, N. S.; Schlau-Cohen, G. S.; Cheng, Y. C.; Ballottari, M.; Bassi, R.; Fleming, G. R., Quantum Coherence Enabled Determination of

the Energy Landscape in Light-Harvesting Complex II. *Journal of Physical Chemistry B* **2009**, *113* (51), 16291-16295.

(10) Mohseni, M.; Rebentrost, P.; Lloyd, S.; Aspuru-Guzik, A., Environment-assisted quantum walks in photosynthetic energy transfer. *Journal of Chemical Physics* **2008**, *129* (17), 174106.

(11) Plenio, M. B.; Virmani, S., Many-body physics and the capacity of quantum channels with memory. *New Journal of Physics* **2008**, *10*, 113019.

(12) Mukamel, S., *Principles of nonlinear optical spectroscopy*. Oxford University Press: New York, 1995; p xviii, 543 p.

(13) Zanni, M. T.; Ge, N. H.; Kim, Y. S.; Hochstrasser, R. M., Two-dimensional IR spectroscopy can be designed to eliminate the diagonal peaks and expose only the crosspeaks needed for structure determination. *Proceedings in the National Academy of Sciences of the United States of America* **2001**, *98* (20), 11265-11270.

(14) Jonas, D. M., Two-dimensional femtosecond spectroscopy. *Annual Review of Physical Chemistry* **2003**, *54*, 425-463.

(15) Ginsberg, N. S.; Cheng, Y. C.; Fleming, G. R., Two-Dimensional Electronic Spectroscopy of Molecular Aggregates. *Accounts of Chemical Research* **2009**, *42* (9), 1352-1363.

(16) Read, E. L.; Engel, G. S.; Calhoun, T. R.; Mancal, T.; Ahn, T. K.; Blankenship, R. E.; Fleming, G. R., Cross-peak-specific two-dimensional electronic spectroscopy. *Proceedings of the National Academy of Sciences of the United States of America* **2007**, *104* (36), 14203-14208.

(17) Schlau-Cohen, G. S.; Calhoun, T. R.; Ginsberg, N. S.; Ballottari, M.; Bassi, R.; Fleming, G. R., Spectroscopic elucidation of uncoupled transition energies in the major photosynthetic light-harvesting complex, LHCII. *Proceedings of the National Academy of Sciences of the United States of America* **2010**, *107* (30), 13276-13281.

(18) van Grondelle, R.; Novoderezhkin, V. I., Energy transfer in photosynthesis: experimental insights and quantitative models. *Physical Chemistry Chemical Physics* **2006**, *8* (7), 793-807.

(19) Schlau-Cohen, G. S.; Calhoun, T. R.; Ginsberg, N. S.; Read, E. L.; Ballottari, M.; Bassi, R.; van Grondelle, R.; Fleming, G. R., Pathways of Energy Flow in LHCII from Two-Dimensional Electronic Spectroscopy. *Journal of Physical Chemistry B* **2009**, *113* (46), 15352-15363.

(20) Calhoun, T. R., Ginsberg, N.S., Schlau-Cohen, G.S., Cheng, Y.-C., Ballottari, M., Bassi, R., Fleming, G.R., Quantum Coherence Enabled Determination of the Energy Landscape in LHCII. *Journal of Physical Chemistry B* **in press**.

(21) Caffarri, S.; Croce, R.; Breton, J.; Bassi, R., The major antenna complex of photosystem II has a xanthophyll binding site not involved in light harvesting. *Journal of Biological Chemistry* **2001**, *276* (38), 35924-35933.

(22) Brixner, T.; Stiopkin, I. V.; Fleming, G. R., Tunable two-dimensional femtosecond spectroscopy. *Optics Letters* **2004**, *29* (8), 884-6.

(23) Brixner, T.; Mançal, T.; Stiopkin, I. V.; Fleming, G. R., Phase-stabilized two-dimensional electronic spectroscopy. *Journal of Chemical Physics* **2004**, *121* (9), 4221-4236.

- (24) Joo, T.; Jia, Y. W.; Fleming, G. R., Ti-Sapphire Regenerative Amplifier for Ultrashort High-Power Multikilohertz Pulses without an External Stretcher. *Optics Letters* **1995**, *20* (4), 389-391.
- (25) Cowan, M. L.; Ogilvie, J. P.; Miller, R. J. D., Two-dimensional spectroscopy using diffractive optics based phased-locked photon echoes. *Chemical Physics Letters* **2004**, *386* (1-3), 184-189.
- (26) Ernst, R. R., Bodenhausen, Geoffrey, Wokaun, Alexander, *Principles of Nuclear Magnetic Resonance in One and Two Dimensions*. Oxford Science Publications: Oxford, 1987.
- (27) Read, E. L.; Schlau-Cohen, G. S.; Engel, G. S.; Wen, J. Z.; Blankenship, R. E.; Fleming, G. R., Visualization of excitonic structure in the Fenna-Matthews-Olson photosynthetic complex by polarization-dependent two-dimensional electronic spectroscopy. *Biophysical Journal* **2008**, *95* (2), 847-856.
- (28) Hochstrasser, R. M., Two-dimensional IR-spectroscopy: polarization anisotropy effects. *Chemical Physics* **2001**, *266* (2-3), 273-284.
- (29) Barron, L. D., *Molecular light scattering and optical activity*. 2nd ed.; Cambridge University Press: Cambridge, UK ; New York, 2004; p xxii, 443 p.
- (30) Dreyer, J.; Moran, A. M.; Mukamel, S., Tensor components in three pulse vibrational echoes of a rigid dipeptide. *Bulletin of the Korean Chemical Society* **2003**, *24* (8), 1091-1096.
- (31) Ishizaki, A.; Fleming, G. R., Unified treatment of quantum coherent and incoherent hopping dynamics in electronic energy transfer: Reduced hierarchy equation approach. *Journal of Chemical Physics* **2009**, *130* (23), 234111.
- (32) Frahmcke, J. S.; Walla, P. J., Coulombic couplings between pigments in the major light-harvesting complex LHC II calculated by the transition density cube method. *Chemical Physics Letters* **2006**, *430* (4-6), 397-403.
- (33) Ishizaki, A.; Calhoun, T. R.; Schlau-Cohen, G. S.; Fleming, G. R., Quantum coherence and its interplay with protein environments in photosynthetic electronic energy transfer. *Physical Chemistry Chemical Physics* **2010**, *12* (27), 7319-7337.

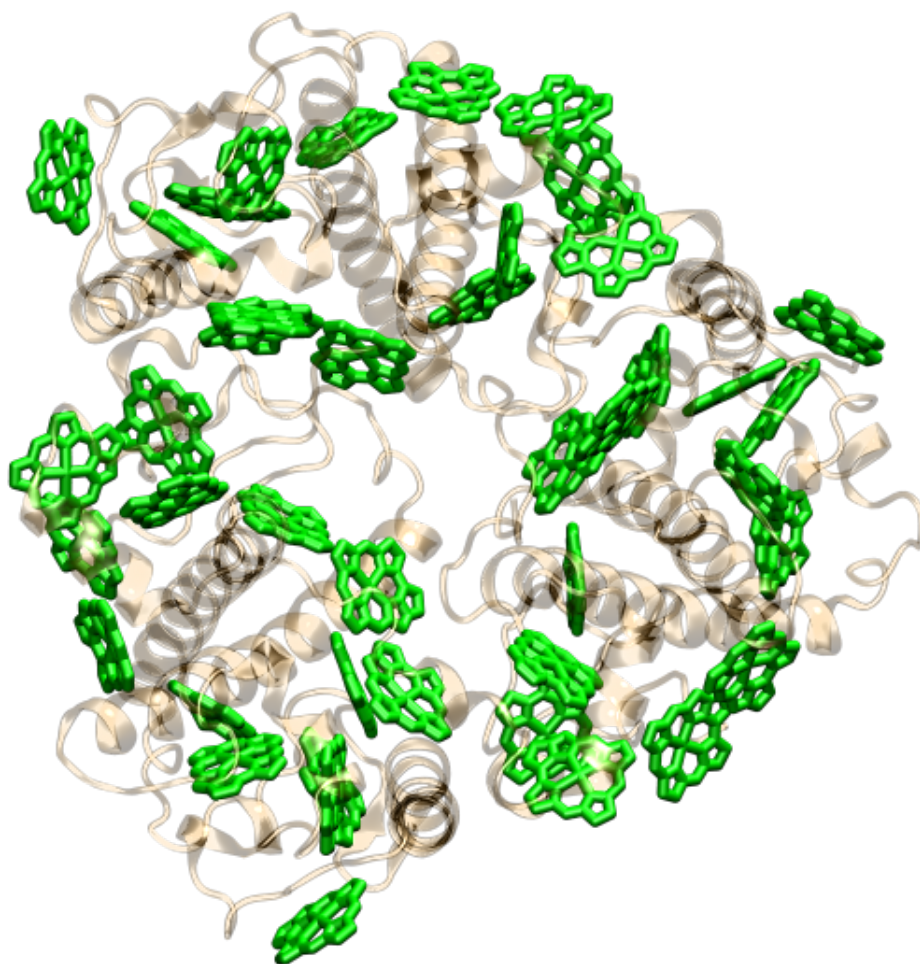


Figure 4.1. The structural model of LHCII from x-ray crystallography, showing the 42 chlorophylls held within a protein scaffold.

Coherence Specific Spectra ($\pi/4, -\pi/4, \pi/2, 0$)

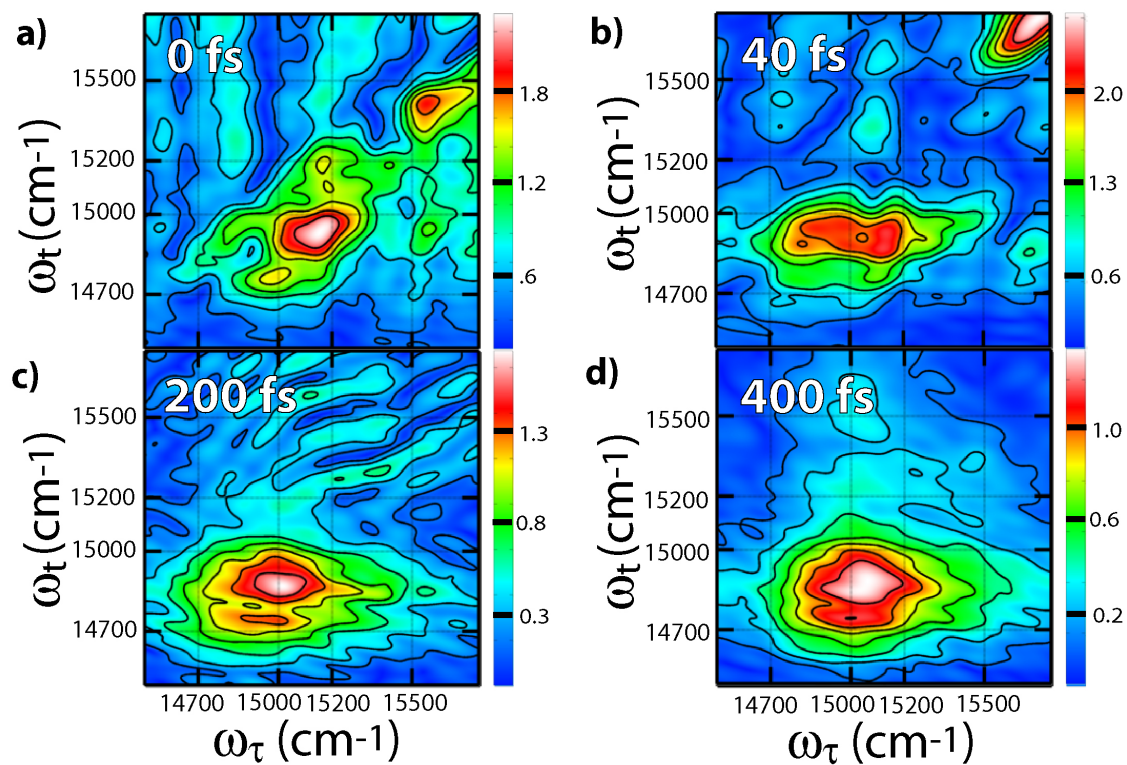


Figure 4.2. Absolute value non-rephasing spectra under the coherence-specific polarization at 77 K for $T=0, 40, 200,$ and 400 fs. Amplitude along the diagonal across the spectra indicates coherence in all spectral regions.

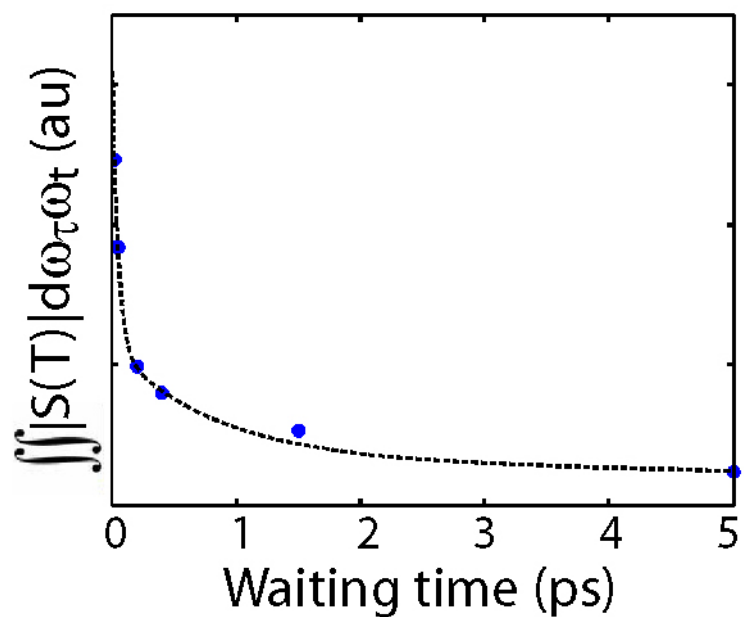


Figure 4.3. Integrated coherence-specific, absolute value relaxation spectra plotted versus waiting time. Fitting of this curve allows for determination of the lifetime of quantum coherence in LHCII.

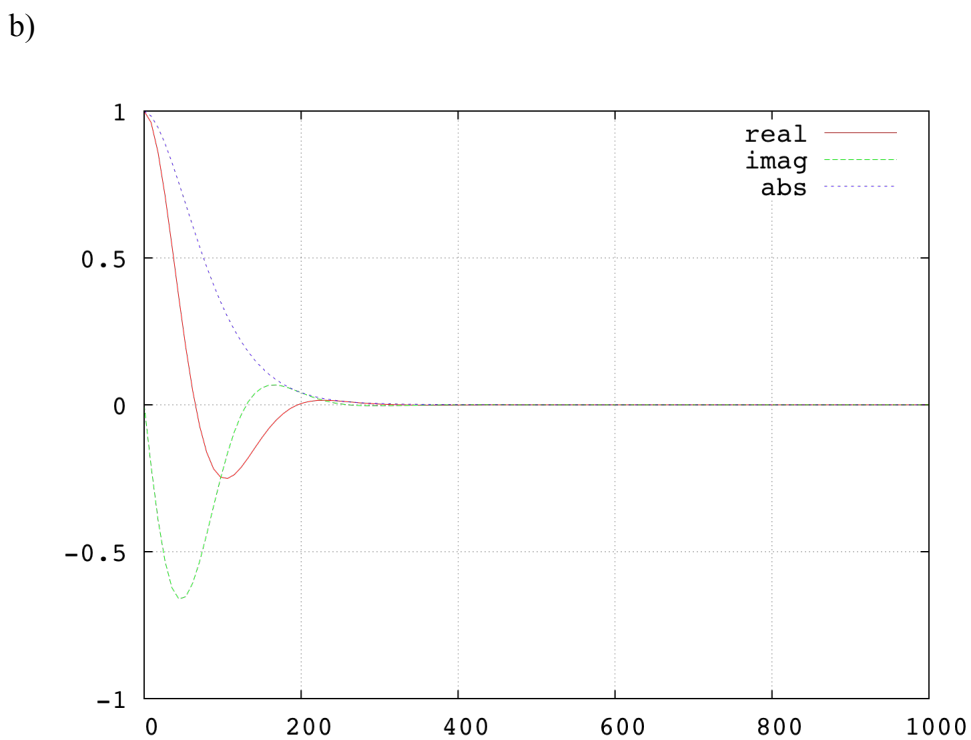
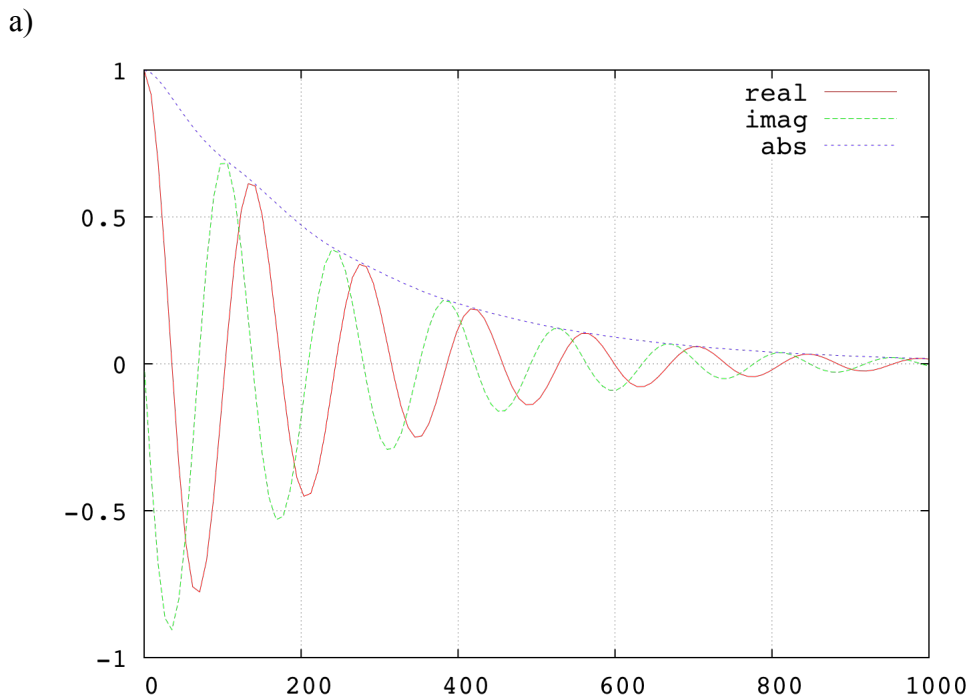


Figure 4.4. Simulation of the decay curves for coherences between pairs of excitons produced by: a) the strongest coupling in LHCII (localized on 611-612) and b) negligibly small couplings (localized on 604-605).

Time Constant (fs)	Amplitude (%)
46.5	64
809	24
1374	11

Table 4.1. The results of fitting the decay of the coherence-specific integrated spectral decay.

Chapter 5

Investigating Energy Transfer in the Bacterial Reaction Center with 2D Electronic Spectroscopy

5.1 Introduction

In photosynthetic light harvesting, photoenergy is converted to chemical energy with near unity quantum efficiency¹. After absorption (primarily in the antenna regions of the photosynthetic apparatus), the excitation energy is transferred to a central location, the reaction center. In the reaction center, an initial charge separation event occurs, which then drives a chain of electron transfer reactions. The molecular structure of the reaction center is highly conserved across species, in contrast to the antenna systems, which exhibit a large amount of architectural and size diversity. The bacterial reaction center is an ideal model system for studying the functionality of reaction centers, because it has been well-characterized by numerous spectroscopic and biochemical experiments¹. Additionally, it serves as a good model for studying couplings and dynamics within photosynthetic pigment-protein complexes more generally due to the relatively small number of pigments and the large body of information about its dynamics. The bacterial reaction center consists of two branches of chromophores, called A and B, which have a pseudo- C_{2V} symmetric arrangement (Fig. 1.1). Each branch contains two bacteriochlorophylls, a bacteriopheophytin and a quinone, with a carotenoid found next to the B branch¹. Despite the structural similarity between the two branches and the fact that energy transfers along both of these branches, electron transfer occurs only along one. The linear absorption spectrum, shown in Fig. 5.1, exhibits a series of well-separated peaks. Most of these peaks contain two states, one from each of the two branches.

Two-dimensional (2D) electronic spectroscopy provides significant insight into the functionality of and interactions within complex biological systems². 2D spectroscopy generates frequency maps of electronic states, molecular coupling and dynamical processes with femtosecond time resolution³. This technique has spectral resolution across both the excitation and emission axes, and can reveal features that are buried in other (linear and non-linear) techniques. In particular, the anti-diagonal elongation in the non-rephasing component of the 2D spectra provides a means to separate closely spaced electronic transitions⁴.

In this chapter, I describe a series of 2D experiments on the bacterial reaction center from *Rhodobacter sphaeroides*. In order to investigate the energy levels and dynamics within the B band, one-color 2D experiments were performed centered at around 800 nm (the Q_y region of the accessory bacteriochlorophyll). Secondly, an apparatus for two-color 2D spectroscopy has been constructed to study the interaction and energy transfer pathways between the carotenoid and the B band. I present the spectra of these experiments and a preliminary analysis of the results.

The Q_y transition for the bacteriochlorophyll exhibits a single peak in linear and most non-linear spectra. As shown in Fig. 5.1, there is a broad feature centered at 800 nm, which contains the Q_y (S_0 - S_1) transition of the two accessory BChl. There is biochemical and spectroscopic support for the existence of more than one overlapping state

encompassed by the peak. For example, three-pulse photon echo peak shift (3PEPS) experiments observed two separate bath correlation timescales within the B band, with 60 fs and 90 fs determined under 790 nm and 810 nm excitation, respectively⁵. Additionally, transient absorption experiments have observed spectroscopic results that suggest that, after excitation of the B band, energy transfer along the A branch is slightly faster.^{6,7} In this work, we use the excitation and emission spectral resolution provided by 2D spectroscopy, as well as the anti-diagonal elongation seen in non-rephasing 2D spectra, to more directly elucidate the excited state energies and relaxation dynamics within the B band.

5.2 Experimental methods

Previously described methods were followed in preparing and isolating the reaction centers of *Rhodobacter sphaeroides*, strain GIC⁸. In order to oxidize the primary electron donor P, the sample was dissolved in 100 mM $K_3Fe(CN)_6$ in Tris/LDAO buffer (pH=8.0). The samples were diluted 30:70 (v/v) with glycerol and cooled to 77 K. The OD at 800 nm was 0.2-0.3 per 200 μ m.

A home-built Ti:sapphire regenerative amplifier, seeded by a home-built Ti:sapphire oscillator, produces a 3.4 kHz pulse train of 45 fs pulses centered at 805 nm with 27 nm of bandwidth as measured by SHG-FROG⁹. The regenerative amplifier output is used directly for the one-color experiments, and also pumps a home-built non-collinear optical parametric amplifier (NOPA) for the two-color experiments. The NOPA produces a pulse encompassing 480 nm – 520 nm, compressed to a duration of 27 fs using a prism pair, as measured by TG-FROG on fused silica. In the one-color experiments at 800 nm, the energy on the sample from each of beams 1, 2, and 3 was 4 nJ per pulse and beam 4 was attenuated by four orders of magnitude. The beams were focused to a 70 μ m beam waist. In the one-color experiments at 500 nm, the energy from of beams 1, 2 and 3 was 15 nJ per pulse and beam 4 was attenuated by four orders of magnitude, focused to a 120 μ m beam waist. During the two-color experiment, the energy on the sample from each of beams 1 and 2 was 36 nJ per pulse, from beam 3 was 6 nJ per pulse, and beam 4 was attenuated by four orders of magnitude. Beams 1 and 2 were focused to a 120 μ m beam waist and beams 3 and 4 to a 70 μ m beam waist. For the polarization experiments, true zero order waveplates (CVI) were inserted into beams 1 and 2 and set with a precision of $\pm 2^\circ$. All measurements were performed at 77 K.

The details of the experimental apparatus, data acquisition and analysis have been described in detail elsewhere.⁹ For the one-color experiments, a single laser beam (either from the regenerative amplifier for the experiments at 800 nm or from the NOPA for the experiments at 500 nm) is split into four beams with a beamsplitter and a diffractive optic. For the two-color experiments, the NOPA output and the regenerative amplifier output are coupled into the apparatus, where both beams are split to generate four beams with the NOPA output used for beams 1 and 2 and the regenerative amplifier output for beams 3 and 4. The use of the diffractive optic allows for phase stability between pulse pairs. Four ultrafast beams are incident on the sample in a so-called box geometry. The interaction of three of the beams with the sample generates the signal, emitted in the phase-matched direction, $\mathbf{k}_s = -\mathbf{k}_1 + \mathbf{k}_2 + \mathbf{k}_3$, collinear with the fourth beam, a local oscillator pulse. The local oscillator is attenuated to ensure it does not interact strongly with the

sample. Using spectral interferometry, the signal is heterodyne-detected in the frequency domain¹⁰.

The measured electric field is a function of the three time delays between the pulses^{3,11}. The time delay between the first two pulses is known as the coherence time, τ , and is controlled to interferometric precision with movable glass wedges, which were scanned from -390 to 390 fs in 1.3 fs steps for the one-color experiments at 800 nm and from -320 to 320 fs in 0.8 fs steps for the one-color experiments at 500 nm and the two-color experiments. Negative coherence times generate the non-rephasing signal and positive times generate the rephasing signal. Between the second and third pulses, the system evolves dynamically during a so-called “waiting time,” T . The third time delay, between pulse 3 and the signal emission is the rephasing time, t . The frequency-frequency 2D spectrum at fixed T is produced by spectrally resolving the signal along ω_t and then Fourier-transforming along the coherence time axis, τ . In this frequency domain representation, the spectrum directly correlates excitation and emission energies. The ensemble of PPCs evolves in a coherence during both the coherence time and the rephasing time. If the system progresses in conjugate frequencies during these two time periods, this allows for the reversal of dephasing and the generation of a photon echo signal. To produce a non-rephasing signal, the ensemble of PPCs evolves with a phase factor of the same sign during the coherence time and the rephasing time, thus generating a free induction decay signal. The rephasing and non-rephasing signals are separated experimentally by the time ordering of pulses one and two. The signal generated over the entire scan, or the sum of the photon echo and free induction decay contributions, produces a relaxation spectrum. Phasing was performed using the projection-slice theorem by separately measuring the spectrally-resolved pump-probe (SRPP) signal for each waiting time³.

5.3 Results & Discussion

5.3.1 Relaxation within the B band

2D real, non-rephasing spectra of the Q_y region are shown in Fig. 5.2. In the linear absorption spectrum shown in Fig. 5.1, the two B band transitions appear as one feature centered close to 800 nm ($12,500 \text{ cm}^{-1}$). As can be seen in the $T=40$ fs spectrum, the 2D non-rephasing spectra exhibit two separate positive, diagonal peaks, corresponding to the two states in the B band that are labeled D1 ($12,325 \text{ cm}^{-1}$) and D2 ($12,450 \text{ cm}^{-1}$). These values are slightly red-shifted from the linear absorption peak due to the partial overlap with the negative, excited state absorption feature at $\sim 12,550 \text{ cm}^{-1}$. In the early time spectra (<100 fs), energy transfer between these two states can be observed in the appearance of a cross-peak connecting these two transitions (the below-diagonal peak is labeled as CP in the $T=70$ fs spectrum). The direct observation of two distinct transitions, as well as the energy transfer between them, was not previously resolvable in other techniques. Based on previous assignments, D1 most likely corresponds to the B_B transition and D2 most likely corresponds to the B_A transition⁵.

Energy has completely transferred out of the B band by the $T=300$ fs spectrum (not shown), in accordance with previous transient absorption measurements⁶. However, as can be seen in the $T=120$ fs spectrum in the lower right of Fig. 5.2, energy transfers out

of the D1 state at a slightly faster rate than out of D2. As is also visible in the spectra of Fig. 5.2, the maximum intensity of CP occurs at about $T=70$ fs.

Further evidence for and ability to quantify the energy transfer appear in the polarization dependence of CP¹². Within a 2D spectrum, each peak is scaled by an orientational prefactor based on the angles between the transition dipole moments in the molecular frame and the angles between the laser pulse polarizations in the lab frame. This has been described extensively in several references¹²⁻¹⁵. Except in the case of energy transfer between a donor and acceptor with parallel transition dipole moments, cross-peaks will scale differently with changes to the polarization of the incident beams than diagonal peaks corresponding to linear absorption will. Spectra were recorded under the all-parallel (0,0,0,0) and cross-peak-specific ($\pi/3,-\pi/3,0,0$) polarization sequences, which are sequences that maximize intensities for energy transfer steps between parallel transitions and between perpendicular transitions, respectively.

Horizontal slices at the emission energy of D1 ($12,325\text{ cm}^{-1}$) are shown in Fig. 5.3 for both the parallel and cross-peak-specific polarization sequences. CP contains both energy transfer population and the dispersive tails of the diagonal peaks. In the all-parallel slices, there are similar relative amplitudes of the CP and D1, and compression and spectral fluctuations produce the small intensity fluctuations as a function of waiting time. Under the cross-peak-specific polarization, however, the suppression of the diagonal peaks allows the dispersive tails to be suppressed as well. This allows relative enhancement of energy transfer peaks, and the energy transfer step appears much more clearly. Specifically, there is a clear increase in relative intensity as energy transfers from the D1 to D2, or as the cross-peak grows in. This is shown in Fig. 5.3b. The CP increases in relative intensity between 40-150 fs. This provides clear evidence of energy transfer occurring at about 100 fs. If there were no energy transfer between these two states, the difference in polarization sequence would not change the relative intensities of the peaks. These spectra provide, for the first time, direct evidence that energy transfers between the two states within the B band.

5.3.2 Energy transfer from neurosporene to the B band

One and two-color 2D spectra showing excitation into the S_2 state of the neurosporene and emission from the Q_y state of the accessory BChl are shown in Fig. 5.4. The corresponding linear absorption spectra are plotted around the 2D results. The 2D spectra illustrate the timescales of overall pathways of energy transfer from the carotenoid to the B band. One-color 2D spectra centered on the S_2 state of the neurosporene are shown in Fig. 5.4, top. These spectra are characterized by a single diagonal feature at the S_2 energy ($20,500\text{ cm}^{-1}$). At early times (not shown), the peak has a much higher intensity, which decays drastically within the first 200 fs. This corresponds primarily to the relaxation from S_2 to S_1 , and is consistent with transient absorption results for carotenoids¹⁶. In the two-color 2D spectra, the peak at ($\omega_r=20,500\text{ cm}^{-1}$; $\omega_i=12,500\text{ cm}^{-1}$) shows energy transfer from the neurosporene to the B band. The intensity of the cross-peak first appears at around 600 fs, reaches a maximum at around 750 fs, and disappears by 1200 fs. There are additional features that appear in the two-color 2D spectra. These peaks are most likely a function of the high pulse energies required to generate a detectable, non-degenerate signal. The cross-sections are much

lower than in the case of fully-degenerate experiments, and thus require higher power. According to our preliminary analysis, the peaks appearing around $19,500\text{ cm}^{-1}$ are most likely due to absorption after triplet formation. Previous experiments have found the T_1 - T_n transition to be centered at around 510 nm ($19,608\text{ cm}^{-1}$) on both the neurosporene and the BChl^{8, 17}. After triplet formation, excitation of the T_1 - T_n transition leads to emission from a previously observed long-lived feature in the B band. This state has been observed in experiments such as flash photolysis, which showed that after excitation there is a change in absorption in the B band that remains for a second timescale¹⁸. This peak, therefore, lasts longer than the repetition rate of the laser, and so appears as a constant feature in all the spectra. Excitation of the T_1 - T_n transition also leads to emission from a state at $12,125\text{ cm}^{-1}$ at a timescale of $\sim 750\text{ fs}$. This emission energy corresponds to the energy of the P_+ state in previous models⁷.

There are four states on the neurosporene and on the accessory BChl that potentially contribute to the energy transfer dynamics observed.^{16, 19} These are illustrated in Fig. 5.5. After excitation into the S_2 state, energy can transfer to the BChl by two pathways: 1) relaxing to S_1 and then transferring to Q_y or 2) transferring to Q_x and relaxing to Q_y . In order to understand the energy transfer pathways and timescales observed, a kinetic model was constructed, where each of the energy transfer steps was modeled as a first order rate equation. The populations that are the result of the current working model of rates are presented in Fig. 5.6. The resultant differential equations were solved analytically. For this calculation, the following values were found to best reproduce the peaks seen in the one- and two-color spectra: $\tau_{S_2-S_1}=200\text{ fs}$, $\tau_{S_2-Q_x}=500\text{ fs}$, $\tau_{S_1-Q_y}=550\text{ fs}$, $\tau_{Q_x-Q_y}=200\text{ fs}$. These results suggest that energy transfers in parallel along these two pathways, instead of a single pathway dominating. A larger component does, however, transfer via S_1 , as can be seen in the relative timescales of relaxation out of S_2 . Further analysis will provide more quantitative information about these relaxation pathways and future modeling will identify the microscopic structural features which give rise to the Coulombic couplings and transition energies that produce the observed dynamics.

5.4 Conclusions

In this chapter, a series of 2D spectra on the bacterial reaction center and a preliminary analysis of the results were presented. These investigations provided insight into previously unobserved pathways of energy transfer. From the one-color experiments on the B band, absorption of the two distinct, previously inseparable states within the B band was observed. Energy transferring between these two states was also seen, in particular from the comparison of the all-parallel and polarized results. These observations have the potential to inform on the differences between the electronic structure of the two branches. They can provide a benchmark for microscopic modeling to understand how small differences in structure between the two branches may lead to small differences in pigment-pigment or pigment-protein couplings, which then produces two excited states with distinct energies and dynamics.

Secondly, two-color 2D spectra were used to directly observe the pathways of energy transfer between the carotenoid and the BChl. The extension of 2D spectroscopy to include non-degenerate pulse sequences provides a means to investigate interaction

and energy transfer between widely separate transitions. Here, it allows more directly observation of energy transferring from the neurosporene to the BChl. Because the bacterial reaction center has been so well-characterized and has relatively few pigments, this provides an ideal starting point for the implementation of this technique. It also provides a useful model system for looking at carotenoid-chlorophyll interaction.

Overall, these experiments both highlight new implementations of 2D spectroscopy and provide new information about the bacterial reaction center. With the information from these experiments, the details of the interaction between the chromophores and the protein environment can be investigated theoretically to understand how small changes in structure may give rise to different electronic structures and excited state dynamics. Secondly, the direct information about the timescale of energy transfer from the carotenoid to the chlorophyll can inform on the strength of interaction, which, in combination with modeling, can provide new insight into the mechanism of coupling between the two chromophores. Together, these experiments illustrate the wealth of information provided by the addition of spectral resolution along both excitation and emission axes, and the potential to access even more dynamical behaviors with the extension into non-degenerate pulse sequences.

5.5 References

- (1) Blankenship, R. E., *Molecular mechanisms of photosynthesis*. Blackwell Science: Oxford, 2002; p 321 p.
- (2) Ginsberg, N. S.; Cheng, Y. C.; Fleming, G. R., Two-Dimensional Electronic Spectroscopy of Molecular Aggregates. *Accounts of Chemical Research* **2009**, *42* (9), 1352-1363.
- (3) Jonas, D. M., Two-dimensional femtosecond spectroscopy. *Annual Review of Physical Chemistry* **2003**, *54*, 425-463.
- (4) Read, E. L.; Schlau-Cohen, G. S.; Engel, G. S.; Wen, J. Z.; Blankenship, R. E.; Fleming, G. R., Visualization of excitonic structure in the Fenna-Matthews-Olson photosynthetic complex by polarization-dependent two-dimensional electronic spectroscopy. *Biophysical Journal* **2008**, *95* (2), 847-856.
- (5) Groot, M. L.; Yu, J.-Y.; Agarwal, R.; Norris, J. R.; Fleming, G. R., Three-Pulse Photon Echo Measurements on the Accessory Pigments in the Reaction Center of *Rhodobacter sphaeroides*. *Journal of Physical Chemistry B* **1998**, *102* (30), 5923-5931.
- (6) Arnett, D. C.; Moser, C. C.; Dutton, P. L.; Scherer, N. F., The first events in photosynthesis: Electronic coupling and energy transfer dynamics in the photosynthetic reaction center from *Rhodobacter sphaeroides*. *Journal of Physical Chemistry B* **1999**, *103* (11), 2014-2032.
- (7) Jonas, D. M.; Lang, M. J.; Nagasawa, Y.; Joo, T.; Fleming, G. R., Pump-probe polarization anisotropy study of femtosecond energy transfer within the photosynthetic reaction center of *Rhodobacter sphaeroides* R26. *Journal of Physical Chemistry* **1996**, *100* (30), 12660-12673.
- (8) Cogdell, R. J.; Monger, T. G.; Parson, W. W., Carotenoid triplet states in reaction centers from *Rhodospirillum rubrum* and *Rhodospirillum rubrum*. *Biochimica et Biophysica Acta (BBA)-Bioenergetics* **1975**, *408* (3), 189-199.

- (9) Brixner, T.; Mancal, T.; Stiopkin, I. V.; Fleming, G. R., Phase-stabilized two-dimensional electronic spectroscopy. *Journal of Chemical Physics* **2004**, *121* (9), 4221-4236.
- (10) Lepetit, L.; Joffre, M., Two-dimensional nonlinear optics using Fourier-transform spectral interferometry. *Optics Letters* **1996**, *21* (8), 564-566.
- (11) Ernst, R. R.; Bodenhausen, G.; Wokaun, A., *Principles of nuclear magnetic resonance in one and two dimensions*. Repr. ... 1988 (with corrections). ed.; Clarendon Press ; Oxford University Press: Oxford [England] New York, 1988; p xxiv, 610 p.
- (12) Hochstrasser, R. M., Two-dimensional IR-spectroscopy: polarization anisotropy effects. *Chemical Physics* **2001**, *266* (2-3), 273-284.
- (13) Barron, L. D., *Molecular light scattering and optical activity*. 2nd ed.; Cambridge University Press: Cambridge, UK ; New York, 2004; p xxii, 443 p.
- (14) Dreyer, J.; Moran, A. M.; Mukamel, S., Tensor components in three pulse vibrational echoes of a rigid dipeptide. *Bulletin of the Korean Chemical Society* **2003**, *24* (8), 1091-1096.
- (15) Schlau-Cohen, G. S.; Calhoun, T. R.; Ginsberg, N. S.; Ballottari, M.; Bassi, R.; Fleming, G. R., Spectroscopic elucidation of uncoupled transition energies in the major photosynthetic light-harvesting complex, LHCII. *Proceedings of the National Academy of Sciences of the United States of America* **2010**, *107* (30), 13276-13281.
- (16) Lin, S.; Katilius, E.; Taguchi, A. K. W.; Woodbury, N. W., Excitation Energy Transfer from Carotenoid to Bacteriochlorophyll in the Photosynthetic Purple Bacterial Reaction Center of *Rhodobacter sphaeroides*. *The Journal of Physical Chemistry B* **2003**, *107* (50), 14103-14108.
- (17) Monger, T. G.; Cogdell, R. J.; Parson, W. W., Triplet states of bacteriochlorophyll and carotenoids in chromatophores of photosynthetic bacteria. *Biochimica et Biophysica Acta (BBA)-Bioenergetics* **1976**, *449* (1), 136-153.
- (18) van Mourik, F.; Reus, M.; Holzwarth, A. R., Long-lived charge-separated states in bacterial reaction centers isolated from *Rhodobacter sphaeroides*. *Biochimica et Biophysica Acta (BBA)-Bioenergetics* **2001**, *1504* (2-3), 311-318.
- (19) Lin, S.; Katilius, E.; Ilagan, R. P.; Gibson, G. N.; Frank, H. A.; Woodbury, N. W., Mechanism of carotenoid singlet excited state energy transfer in modified bacterial reaction centers. *Journal of Physical Chemistry B* **2006**, *110* (31), 15556-15563.

Oxidized bacterial reaction center at 77 K

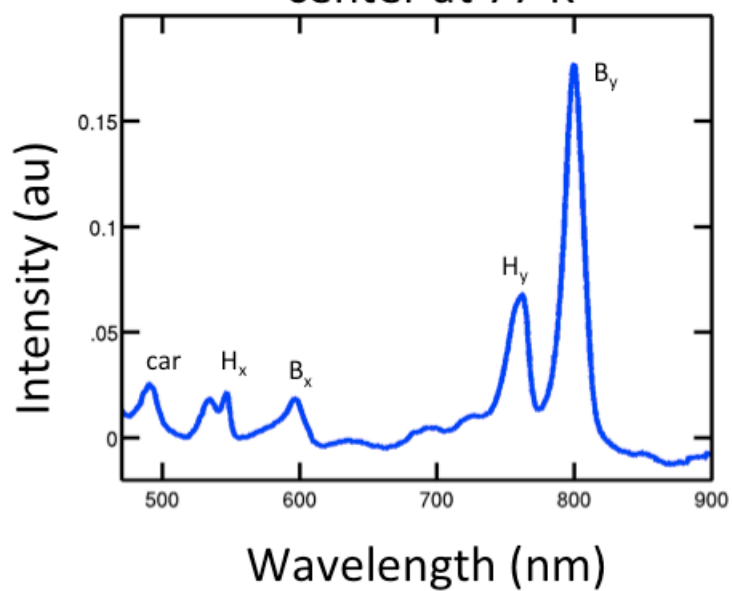


Figure 5.1. Linear absorption spectrum of the oxidized bacterial reaction center from GIC-strain *Rhodobacter sphaeroides* at 77 K.

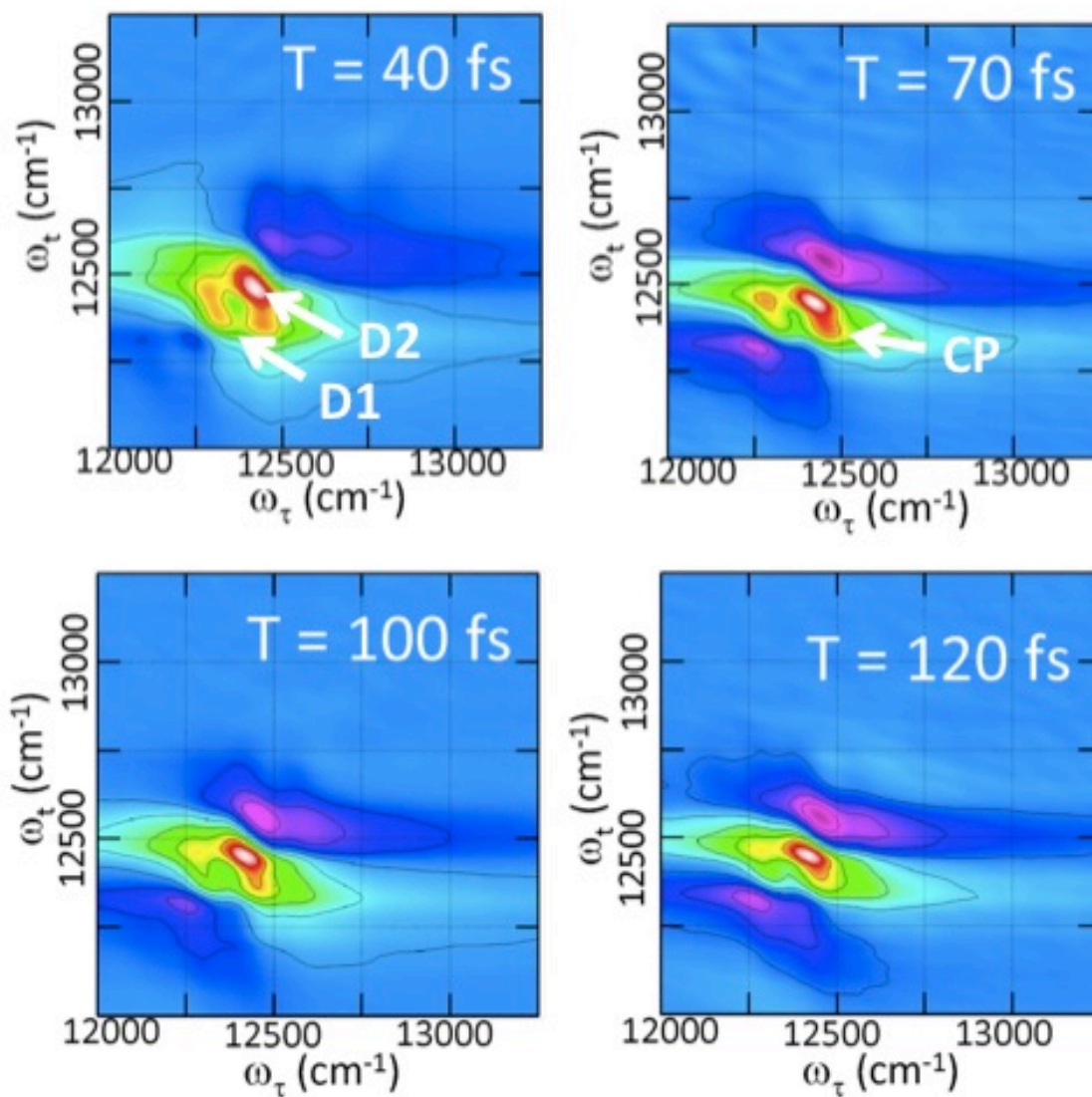


Figure 5.2. Real, non-rephasing 2D spectra of the B band at selected waiting times. These spectra exhibit two separated states along the diagonal, labeled D1 and D2 in the $T=40$ fs spectrum. Energy transfer between these two states appears in the increase in intensity of the cross-peak labeled CP in the $T=70$ fs spectrum.

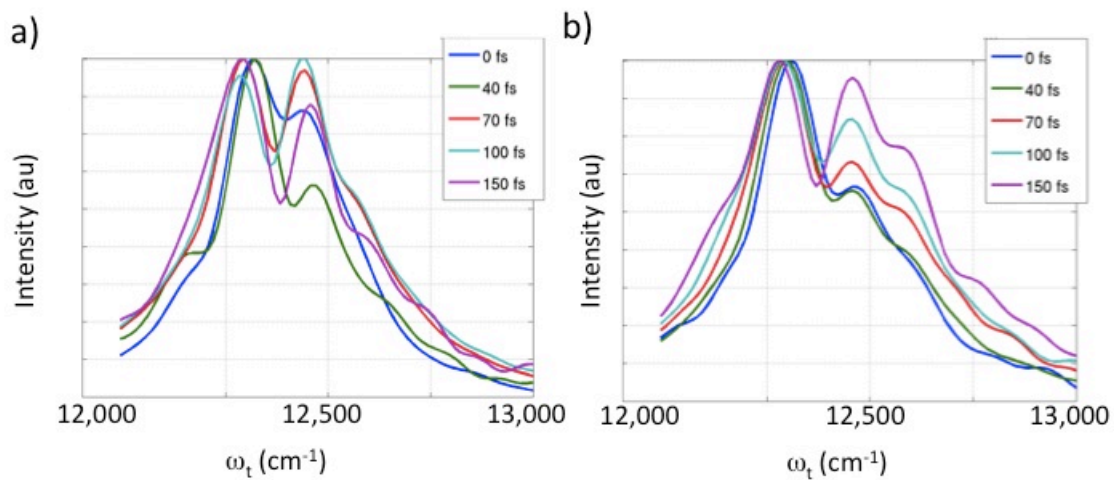


Figure 5.3. Horizontal slices from the 2D spectra at $\omega_i=12,325\text{ cm}^{-1}$ for a) all-parallel and b) cross-peak-specific polarization sequences. The difference in scaling with polarization, as appears in the clear grow-in of the cross-peak ($\omega_t=12,450\text{ cm}^{-1}$) under the cross-peak-specific sequence, indicates the existence of an energy transfer pathway.

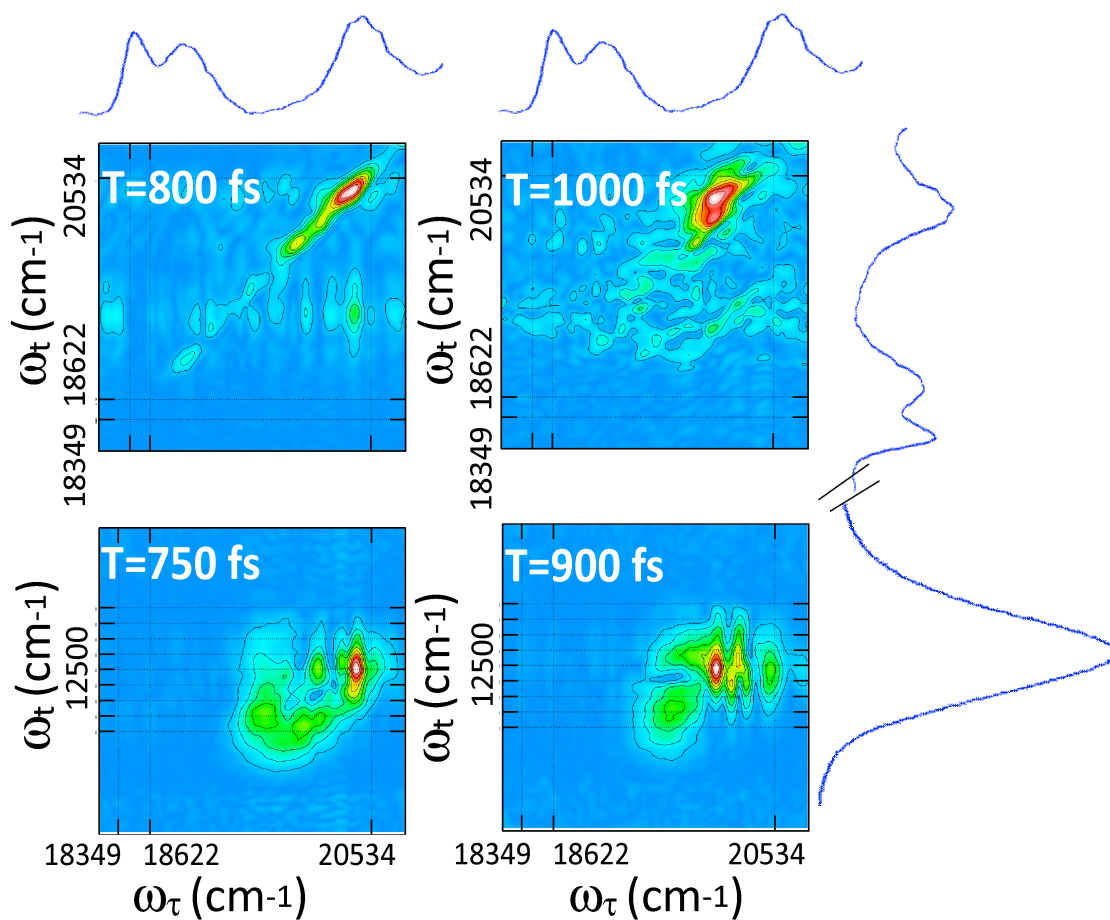


Figure 5.4. One- and two-color 2D spectra of the bacterial reaction center, with the linear absorption spectra of the corresponding spectral regions plotted above and to the right for selected waiting times. The one-color spectra show the decay of the ground state bleach as the energy transfers from the neurosporene to the BChl. The two-color spectra show energy transfer, as the peak indicating excitation into the S_2 state of the carotenoid and emission out of the B band reaches a maximum intensity at around 750 fs.

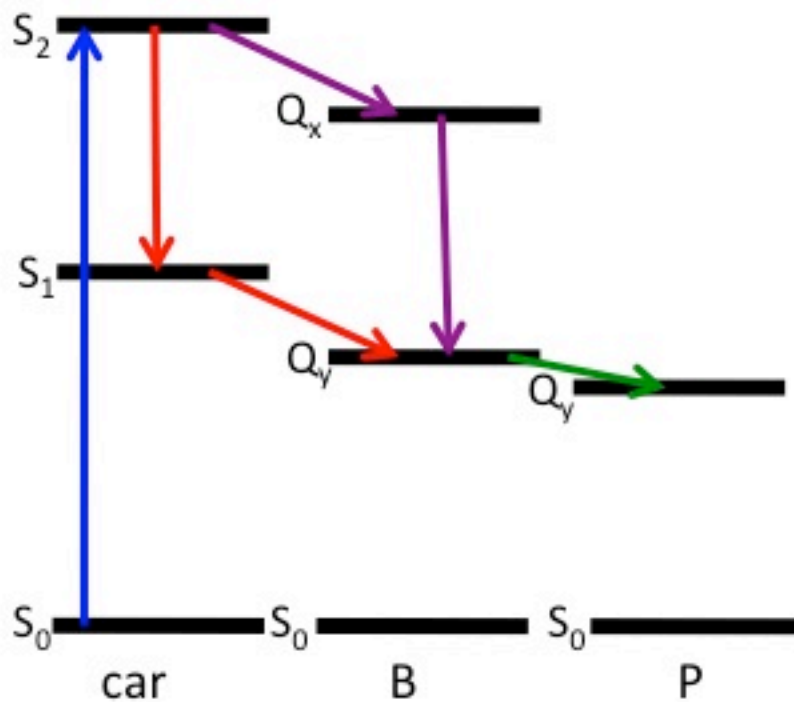


Figure 5.5. Model of the states involved in energy transferring from the carotenoid to the B band, and then transferring out of the B band. As shown, energy can transfer in two parallel pathways.

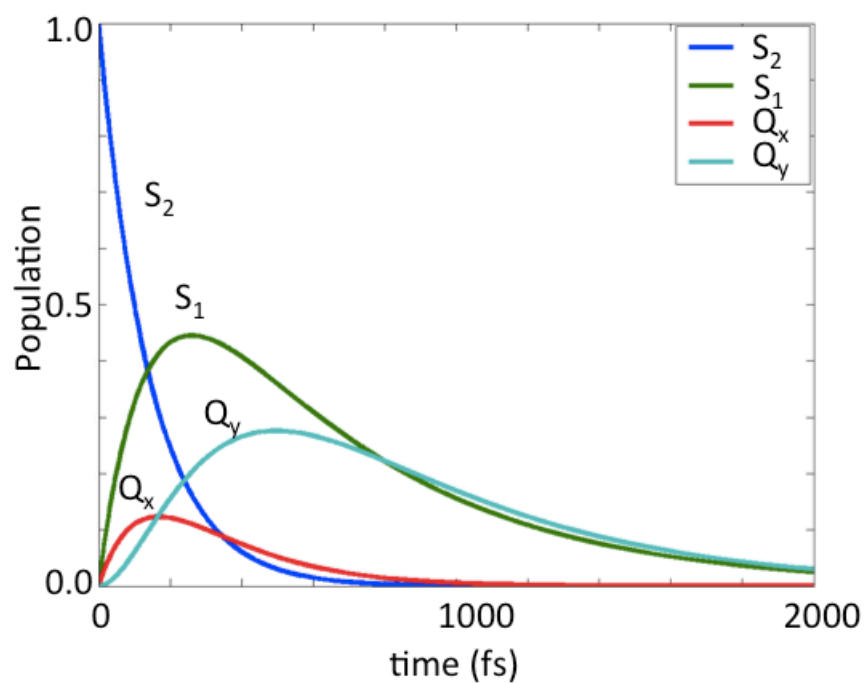


Figure 5.6. Calculated populations of the four states of the carotenoid and accessory Chl after excitation into the S_2 state of the carotenoid. These values were calculated based on first order kinetics between each state, in accordance with the state diagrams shown in Fig. 5.5.

Chapter 6

Conclusion

6.1 Afterword

In this thesis, several distinctive characteristics of photosynthetic light harvesting, and the means by which 2D spectroscopy can investigate these properties, have been discussed. These design principles may be useful in the construction of devices. Just as the design of modern electronics relies heavily on sophisticated modeling and simulation tools, the design of artificial light-harvesting devices would be greatly aided by simulation tools that allow rapid exploration of the influence of specific design parameters on predicted total energy output, device lifetime, and other desired properties. While extensive theoretical effort has gone into simulating the microscopic photophysics of light-harvesting complexes^{1,2}, some examples of which have been discussed in previous chapters, there remains a need for larger scale methods to consider the entire photosynthetic unit. These models can better integrate these microscopic behaviors into a functional system. To date, there have been only a few efforts to make these larger-scale models³⁻⁵. These models could, however, provide a guide for incorporating the microscopic behaviors described here into devices.

Currently, many different approaches to reproduce photosynthetic functionality are under development, including genetic manipulation of biological systems to optimize light-harvesting^{5,6}, incorporation of biological components into synthetic devices, synthetic devices that mimic photosynthetic dynamics,^{7,8} and mixed biological/inorganic systems^{9,10}. In designing these devices, the help of an analytical model could, for example, indicate the optimal packing density of absorbing molecules. The concentration could be tuned to overcome the paucity of solar photons and introduce strong interactions between pigments, which would then drive unidirectional, ultrafast energy transfer via both coherent and incoherent dynamics, as has been observed in photosynthetic systems. This approach could also be used to optimize the level of delocalization based on function (e.g., energy wire vs. antenna), as the level of delocalization affects the angular specificity of energy transfer off of a chromophore, as described in Chapter 2. Secondly, an analytical model could evaluate the benefits of including a secondary light-harvester. The information about interaction and energy transfer pathways from Chapter 5 could be used to calculate whether or not the additional spectral coverage would balance the construction cost of including a second chromophore.

Beyond the features of photosynthetic light-harvesting discussed here, photosynthesis exhibits additional desirable characteristics which make this direction of research particularly appealing. Photosynthetic proteins have the ability to turn on pathways that quench excess energy, and thus prevent the formation of Chl triplet states that in turn produce singlet oxygen. This photosynthetic functionality has already been reproduced in devices, such as with a pH-dependent quenching pathway in a porphyrin hexad system.⁷ Additionally, photosynthetic systems have the ability to self-repair, or replace components after oxidative damage¹¹. Recently, researchers have successfully copied this functionality by introducing repair mechanisms into photosynthetic reaction

centers attached to nanotube substrates.¹⁰ Finally, following the photosynthetic model would mean the construction of all the molecular machinery out of readily available, earth abundant materials¹¹. As we learn more about photosynthetic function, these lessons will aid in efforts to adapt what bacteria, algae and plants accomplish – conversion of sunlight into usable energy in a robust, renewable manner – to meet our long-term energy needs.

6.2 References

- (1) van Grondelle, R.; Novoderezhkin, V. I., Energy transfer in photosynthesis: experimental insights and quantitative models. *Physical Chemistry Chemical Physics* **2006**, *8* (7), 793-807.
- (2) Ishizaki, A.; Calhoun, T. R.; Schlau-Cohen, G. S.; Fleming, G. R., Quantum coherence and its interplay with protein environments in photosynthetic electronic energy transfer. *Physical Chemistry Chemical Physics* **2010**, *12* (27), 7319-7337.
- (3) Yang, M.; Fleming, G. R., Construction of kinetic domains in energy trapping processes and application to a photosynthetic light harvesting complex. *The Journal of chemical physics* **2003**, *119*, 5614.
- (4) Zhu, X. G.; Long, S. P.; Ort, D. R., What is the maximum efficiency with which photosynthesis can convert solar energy into biomass? *Current opinion in biotechnology* **2008**, *19* (2), 153-159.
- (5) Melis, A., Solar energy conversion efficiencies in photosynthesis: Minimizing the chlorophyll antennae to maximize efficiency. *Plant science* **2009**, *177* (4), 272-280.
- (6) Noy, D.; Moser, C. C.; Dutton, P. L., Design and engineering of photosynthetic light-harvesting and electron transfer using length, time, and energy scales. *Biochimica et Biophysica Acta (BBA)-Bioenergetics* **2006**, *1757* (2), 90-105.
- (7) Terazono, Y.; Kodis, G.; Liddell, P. A.; Garg, V.; Moore, T. A.; Moore, A. L.; Gust, D., Multiantenna Artificial Photosynthetic Reaction Center Complex. *Journal of Physical Chemistry B* **2009**, *113* (20), 7147-7155.
- (8) Hardin, B. E.; Hoke, E. T.; Armstrong, P. B.; Yum, J. H.; Comte, P.; Torres, T.; Frechet, J. M. J.; Nazeeruddin, M. K.; Gratzel, M.; McGehee, M. D., Increased light harvesting in dye-sensitized solar cells with energy relay dyes. *Nature Photonics* **2009**, *3* (7), 406-411.
- (9) Das, R.; Kiley, P. J.; Segal, M.; Norville, J.; Yu, A. A.; Wang, L. Y.; Trammell, S. A.; Reddick, L. E.; Kumar, R.; Stellacci, F.; Lebedev, N.; Schnur, J.; Bruce, B. D.; Zhang, S. G.; Baldo, M., Integration of photosynthetic protein molecular complexes in solid-state electronic devices. *Nano Letters* **2004**, *4* (6), 1079-1083.
- (10) Faulkner, C. J.; Lees, S.; Ciesielski, P. N.; Cliffl, D. E.; Jennings, G. K., Rapid assembly of photosystem I monolayers on gold electrodes. *Langmuir* **2008**, *24* (16), 8409-8412.
- (11) Blankenship, R. E., *Molecular mechanisms of photosynthesis*. Blackwell Science: Oxford, 2002; p 321 p.

Appendix A

Theoretical Methods for Simulation of 2D Spectra of LHCII

This chapter is reproduced with permission from
G. S. Schlau-Cohen, T. R. Calhoun, N. S. Ginsberg, E. L. Read, M. Ballottari,
R. Bassi, R. van Grondelle, G. R. Fleming
“Pathways of energy flow in LHCII from two-dimensional electronic spectroscopy”
Journal of Physical Chemistry B (2009), **113**, 15352-15363
© 2009 American Chemical Society

All citations in this appendix refer to those in Chapter 2

The full Hamiltonian used in the simulations is presented in Table A.1. The off-diagonal elements were generated as described in the main text. The diagonal elements were produced through sum of squares fitting to the linear absorption spectrum. The values were bounded by limitations imposed by site-directed mutagenesis (ref 11 of the main text) and starting conditions were varied across this range (a width averaging ~ 200 cm^{-1}). Each set of starting conditions was repeated five times and was run for 1000 iterations. The non-linear spectra were calculated with the results of fits that converged. The final set of site energies chosen, the values shown here, was evaluated by comparison to the linear and non-linear spectra. This set of site energies shows the Chl-a main peak, a clear shoulder and a distinct Chl-b peak in the linear absorption spectrum and reproduces the double peak structure visible in the Chl-a band of the 2D spectra (with clear separation between the two peaks). While these values do not necessarily represent a unique solution, they are the only set that matches the spectroscopic results as described. Values published previously do not produce two well-separated peaks. Because linear spectroscopies and non-linear techniques used for previous fitting are subject to homogeneous and inhomogeneous broadening in one dimension, the peaks overlap in congested spectra, resulting in additional difficulty in resolving excitonic energies.

Chl	601	602	603	604	605	606	607	608	609	610	611	612	613	614
601	15764	47.1	-6.1	-2.7	0.5	-2.0	-2.6	3.3	4.4	-4.5	24.5	2.3	-8.4	2.9
602	-47.1	15103	17.4	5.5	-0.2	4.9	6.2	-5.8	-21.9	-5.4	0.7	10.1	-1.9	0.1
603	-6.1	17.4	15262	-0.5	-0.2	-2.1	8.2	4.2	71.6	8.4	-0.7	-0.6	2.4	-5.7
604	-2.7	5.5	-0.5	15390	5.4	80.8	26.0	-5.7	-1.5	-0.2	-3.3	3.7	2.2	-2.8
605	0.5	-0.2	-0.2	5.4	15544	11.5	-5.2	-3.7	-0.1	0.8	1.1	-2.2	-1.2	0.0
606	-2.0	4.9	-2.1	80.8	11.5	15686	23.7	-6.7	-11.8	-0.6	-2.0	2.1	1.2	-1.8
607	-2.6	6.2	8.2	26.0	-5.2	23.7	15557	-3.5	-1.7	-0.4	-2.1	2.2	2.7	-2.4
608	3.3	-5.8	4.2	-5.7	-3.7	-6.7	-3.5	15678	26.1	57.0	4.8	-1.3	-2.2	1.4
609	4.4	-21.9	71.6	-1.5	-0.1	-11.8	-1.7	26.1	15616	1.1	3.3	-0.2	-2.5	2.0
610	-4.5	-5.4	8.4	-0.2	0.8	-0.6	-0.4	57.0	1.1	15038	-26.4	12.4	6.0	-1.2
611	24.5	0.7	-0.7	-3.3	1.1	-2.0	-2.1	4.8	3.3	-26.4	15180	105.0	-0.8	0.6
612	2.3	10.1	-0.6	3.7	-2.2	2.1	2.2	-1.3	-0.2	12.4	105.0	15082	-1.0	-0.2
613	-8.4	-1.9	2.4	2.2	-1.2	1.2	2.7	-2.2	-2.5	6.0	-0.8	-1.0	15160	-28.0
614	2.9	0.1	-5.7	-2.8	0.0	-1.8	-2.4	1.4	2.0	-1.2	0.6	-0.2	-28.0	15309

Table A.1. LHCII monomer Hamiltonian used in the simulations presented in the main text. Site energies are given in bold.

Appendix B

This chapter is reproduced with permission from
 G. S. Schlau-Cohen, T. R. Calhoun, N. S. Ginsberg, E. L. Read, M. Ballottari,
 R. Bassi, R. van Grondelle, G. R. Fleming
Proceeding of the National Academy of Science (2010), **107**, 13276-13281
 © 2010 National Academy of Science

All citations in this appendix refer to those in Chapter 3

B.1. Angle between etdms for model dimer system

We present an analytical form for the angle between the excitonic transition dipole moments (etdm) of a dimer as a function of the site basis Hamiltonian and the site-basis transition dipole moments (stdm). Roman numerals enumerate the individual chromophores and Arabic numbers enumerate the excitons. The site basis Hamiltonian (H_{site}) is diagonalized by the orthogonal transformation matrix, U , to produce the Hamiltonian in the exciton basis ($H_{exciton}$)³²,

$$H_{exciton} = U^{-1} H_{site} U$$

where the site basis Hamiltonian is,

$$H_{site} = \begin{pmatrix} \varepsilon_I & J \\ J & \varepsilon_I + \Delta\varepsilon \end{pmatrix}$$

where ε_I is the energy of the uncoupled transition on chlorophyll I (with $\Delta\varepsilon$ the energy difference between the chlorophyll I and II), and J is the Coulombic coupling between the chromophores. The eigenvalues of this matrix give the energies of the excitonic transitions,

$$E_{\pm} = \varepsilon_I + \frac{\Delta\varepsilon}{2} \pm \sqrt{\left(\frac{\Delta\varepsilon}{2}\right)^2 + J^2}$$

The transformation matrix that diagonalizes the site-basis Hamiltonian for this dimer has the following form,

$$U = \begin{pmatrix} \frac{1}{\sqrt{2\left(\left(\frac{\Delta\varepsilon}{2J}\right)^2 + 1 + \left(\frac{\Delta\varepsilon}{2J}\right)\sqrt{\left(\frac{\Delta\varepsilon}{2J}\right)^2 + 1}\right)}} & \frac{1}{\sqrt{2\left(\left(\frac{\Delta\varepsilon}{2J}\right)^2 + 1 - \left(\frac{\Delta\varepsilon}{2J}\right)\sqrt{\left(\frac{\Delta\varepsilon}{2J}\right)^2 + 1}\right)}} \\ \left(\frac{\Delta\varepsilon}{2J}\right) + \sqrt{\left(\frac{\Delta\varepsilon}{2J}\right)^2 + 1} & \left(\frac{\Delta\varepsilon}{2J}\right) - \sqrt{\left(\frac{\Delta\varepsilon}{2J}\right)^2 + 1} \\ \frac{1}{\sqrt{2\left(\left(\frac{\Delta\varepsilon}{2J}\right)^2 + 1 + \left(\frac{\Delta\varepsilon}{2J}\right)\sqrt{\left(\frac{\Delta\varepsilon}{2J}\right)^2 + 1}\right)}} & \frac{1}{\sqrt{2\left(\left(\frac{\Delta\varepsilon}{2J}\right)^2 + 1 - \left(\frac{\Delta\varepsilon}{2J}\right)\sqrt{\left(\frac{\Delta\varepsilon}{2J}\right)^2 + 1}\right)}} \end{pmatrix}$$

The transformation matrix depends only ratio of $\Delta\varepsilon$ and J , and so is entirely independent of the total magnitude of $\Delta\varepsilon$, J and ε . The etdms (\mathbf{d}_n) are linear combinations of the stdms (\mathbf{d}_m) given by,

$$\mathbf{d}_n \equiv \langle 0 | \hat{\mu} | \psi_n \rangle = \sum_m U_{n,m}^{-1} \mathbf{d}_m$$

where n corresponds to exciton 1 or 2, m corresponds to chlorophylls I or II, and $|\psi_n\rangle$ is the excitonic wavefunction. The angle between etdms can be found using the normalized etdms,

$$\theta_{1,2} = \cos^{-1}(\hat{\mathbf{d}}_1 \cdot \hat{\mathbf{d}}_2)$$

The analytical form of the angle between etdms is the following,

$$\theta_{1,2} = \cos^{-1} \left(\frac{\left(\frac{\Delta\varepsilon}{2J} \right) \cos \theta_{I,II}}{\sqrt{\left(\frac{\Delta\varepsilon}{2J} \right)^2 + 1 - \cos^2 \theta_{I,II}}} \right)$$

where $\theta_{I,II}$ is the angle between the stdms of the two chromophores,

$$\mathbf{d}_I \cdot \mathbf{d}_{II} = \cos \theta_{I,II}$$

The equation for an example system is plotted in Fig. 3.4b.

B.2 Additional Figures

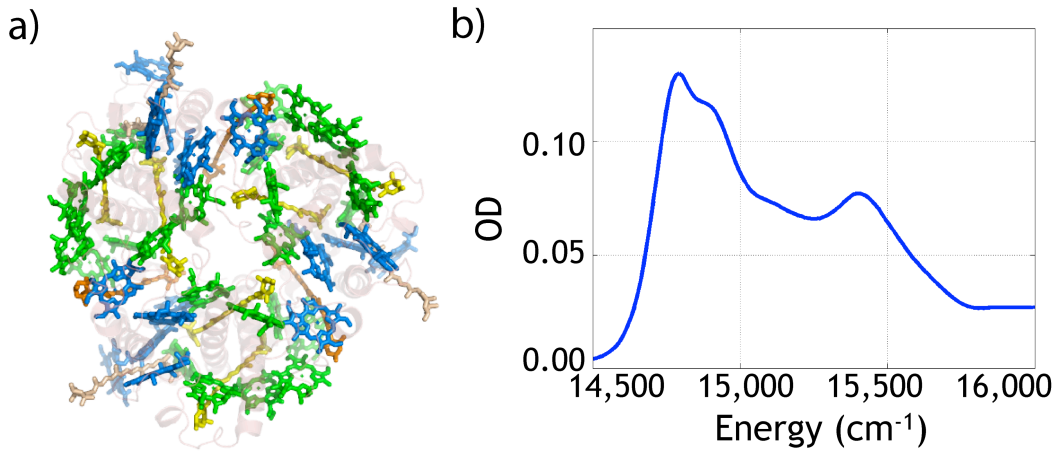


Figure B.1. a) LHCII structural model from x-ray crystallography containing pigments (8 Chla in green, 6 Chlb in blue, and 4 carotenoids in yellow, orange, and off-white per monomer)²¹ held within the protein helices; b) linear absorption spectrum of the Q_y region (S₀-S₁ transition) of LHCII at 77 K.

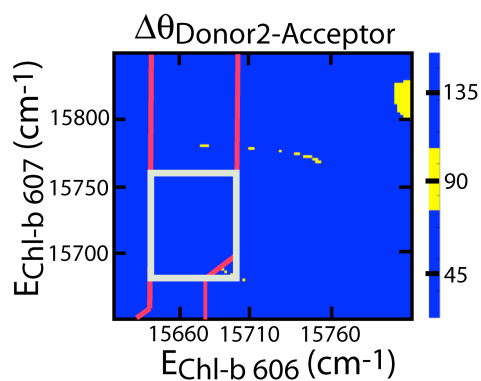


Figure B.2. The plot in this figure shows the angle between etdms as a function of site basis transition energies of two chromophores which are coupled to each other. The angle between donor 2 (localized mostly on Chl**b** 607) and the acceptor (localized on a third chromophore, Chl**b** 605) as a function of the site-basis transition energies of the two Chl**b** molecules which give rise to the donor excitons. The bounds from site-directed mutagenesis of Chl**b** 606 are shown in pink. The off-white box indicates the range of the site-basis transition energies for Chl**b**s 606 and 607 that matches experimental results